5-2012

High Frequency Characterization of Carbon Nanotube Networks for Device Applications

Emmanuel Decrossas
University of Arkansas, Fayetteville

HIGH FREQUENCY CHARACTERIZATION OF CARBON NANOTUBE NETWORKS FOR DEVICE APPLICATIONS

HIGH FREQUENCY CHARACTERIZATION OF CARBON NANOTUBE NETWORKS FOR DEVICE APPLICATIONS

A dissertation submitted in partial fulfillment
of the requirements for the degree of
Doctor of Philosophy in Engineering

By

Emmanuel Decrossas
Université Pierre et Marie Curie – Paris 6
Bachelor of Engineering Science, 2004
Université Pierre et Marie Curie – Paris 6
Master of Science in Electrical Engineering, 2006

May 2012
University of Arkansas

ABSTRACT

This work includes the microwave characterization of carbon nanotubes (CNTs) to design new CNTs-based high frequency components. A novel developed method to extract the electrical properties over a broad microwave frequency band from 10 MHz to 50 GHz of carbon nanotubes (CNTs) in a powder form is performed. The measured scattering parameters (S-parameters) with a performance network analyzer are compared to the simulated one obtained from an in-house computed mode matching technique (MMT). An optimized first order gradient method iteratively changes the unknown complex permittivity parameters to map the simulated S-parameters with the measured one until convergence criteria are satisfied. The mode matching technique accurately describes waveguide discontinuities as both propagating and evanescent modes are considered allowing an error less than 5% on the extracted permittivity over a broad frequency range. The very large values obtained at low frequencies of carbon nanotubes permittivity are explained theoretically and experimentally based on the percolation theory. The powder composed of semiconducting and conducting CNTs illuminated by an electromagnetic field is seen as series of nano-resistance-capacitance which significantly increase the real and imaginary parts of the complex effective permittivity until the percolation threshold is reached. Based on experimental results different CNTs-based composites material are engineered to design novel microwave components for possible electromagnetic compatibility (EMC) applications.

As the extraordinary properties of the carbon nanotubes exist along their axis, the second part of this work is oriented on the alignment and the deposition of carbon nanotubes using a dielectrophoresis (DEP) technique. Micro/nano-electrodes are fabricated using a lift-off process consisting of photo-lithography and electron-beam lithography techniques where the carbon

nanotubes suspended in an aqueous solution are attracted in the gap between the electrodes by applying an AC bias voltage. After burning the conducting carbon nanotubes an observed photocurrent with aligned semiconducting CNTs is used to develop high frequency photo-device prototypes.

This dissertation is approved for recommendation
to the Graduate Council.

Dissertation Director:

_____
Dr. Samir M. El-Ghazaly

Dissertation Committee:

_____
Dr. Victor Fouad Hanna

_____
Dr. Hameed A. Naseem

_____
Dr. Shui-Qing (Fisher) Yu

_____
Dr. Juan C. Balda

DISSERTATION DUPLICATION RELEASE

I hereby authorize the University of Arkansas Libraries to duplicate this dissertation when needed for research and/or scholarship.

Agreed _____

Emmanuel Decrossas

Refused _____

Emmanuel Decrossas

ACKNOWLEDGEMENTS

I would like to express my sincere gratitude to my supervisor Dr. Samir M. El-Ghazaly for his insight and guidance through this journey. I'm deeply in debt of Dr. Victor Fouad Hanna who encouraged me to pursue my graduate studies and motivated me with his precious advices. It has been a pleasure to work under their supervision and let me enough freedom to work and think outside the box to achieve my goals. I would like to also thank my other committee members Dr. Hameed Naseem, Dr. Juan Balda and Dr. Shui-Qing (Fisher) Yu for their time, supports and precious comments along all those years.

Many thanks to Dr. Mahmoud EL Sabbagh who closely follows my achievements and encourages me when nothing seemed to work as expected. His collaboration results in many publications and numerous achievements. At last but not least I would like to thank all professors and staff at the University of Arkansas for their support throughout the years to create such a nice environment for graduate students and makes me feel at home.

I'm grateful to Denis Roger who manufactured the measurement setup describes in this work and his advices through our long conversations to machine such devices. I also thank the University of Arkansas' High Density Electronics Center staff members for their help with thin film fabrication processing and the gain knowledge about working in clean room environment.

Finally, I would like to show my gratitude to Drs. Madan Dubey and Barbara Nichols who gratefully approved my published manuscripts and conference papers. Research was sponsored by the Army Research Laboratory who sponsored this research and was accomplished under Cooperative Agreement Number W911NF-10-2-0072. The views and conclusions contained in this are those of the authors and should not be interpreted as representing the official policies, either expressed or implied, of the Army Research Laboratory or the U.S. Government. The U.S.

TABLE OF CONTENTS

I. INTRODUCTION

A. HISTORY OF THE DISCOVERY

The discovery of carbon nanotubes is frequently attributed to Iijima in 1991 [1]. However, in 1952, an image of 50 nanometer diameter tubes of carbon is published by two Russian researchers, L.V. Radushkevich and V.M. Lukyanovich [2]. The manuscript written in Russian during the cold war period (1946-1991) is largely unnoticed by the Western countries. Some researchers assert that carbon nanotubes existed even before but have not been observed. In fact, the observation of carbon nanotubes realized by Iijima coincides with the development of the transmission electron microscope (TEM) images. For instance, Oberlain et al. published images of nanometer size carbon fiber in 1976 using high resolution electron microscopy [3]. Three years later, Abrahamson presented nanometer diameter carbon fibers obtained by arc discharge in the 14^{th} biennial conference on carbon [4]. Then in 1981, Kolesnik et al. suggested forming carbon multilayer tubular crystals by rolling graphene layer and mentioned different possible crystal arrangements now known as armchair and chiral carbon nanotubes [5]. Six years later, Tennent patented a method to produce nanometer size carbon fibrils with high aspect ratio [6].

B. FROM GRAPHENE TO CARBON NANOTUBES

The element carbon in a solid phase exists through different allotropes depending on how the covalent bonding between carbon atoms is realized. The way carbon atoms are organized in a crystal changes its material properties (e.g. diamond and coal own both the same carbon element but different atomic structure). For instance graphite which can be found in pencil lead is composed of multi-layers of graphene. Geim and Novoselov received the Nobel Prize in physics 2010 after the discovery and characterization of graphene consisting of a single mono-atomic layer of carbon atoms by peeling off coal samples using scotch tape [7].

Graphene can be rolled in spherical shape such as buckyballs or cylindrical form called carbon nanotubes [8] defining the different allotropes of carbon as shown in Fig. 1.1. The physical properties of carbon nanotubes [9]-[10] have demonstrated unique electronic structure depending on their dimensions and chiralities, which have been considered as a major discovery in semiconductor devices. Usually, CNTs are classified in two categories: Single-wall CNTs (SWCNTs) composed of a single graphitic cylinder where the diameter varies from 0.7 to 2 nm and Multi-wall CNTs (MWCNTs) composed of several concentric graphitic layers with a diameter varying from 10 to 200 nm.

In 1993, Iijima is the first one to predict the conducting or semiconducting nature of the carbon nanotubes based on the diameter of the tube and its chiral angle [12]. In addition, due to strong covalent carbon-carbon bonding CNTs present very high tensile strength, thermal and electrical conductivity.

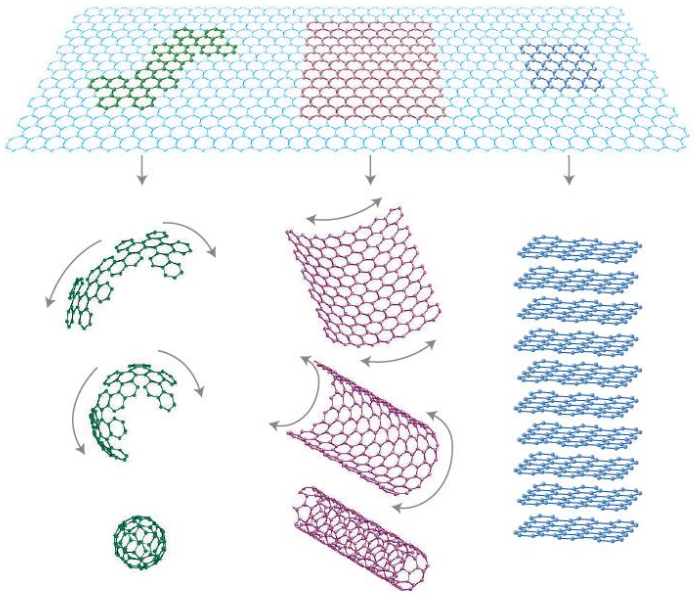

Fig. 1.1: Different graphitic formed from graphene (at the top) to (from left to right): buckyball, carbon nanotube and graphite [11].

The Band structure calculation methods have been extensively studied for quantum wells, quantum dots and semiconductors properties. Usually, the most common theoretical models include the Kane theory or **k.p** method, the envelop function approximation and the tight-binding method which is the technique chosen in the section [13]. To simplify the energy band calculation, we may consider the strong interaction of a localized electron tightly bound to the positive ion instead of looking at weak periodic potential slightly perturbed. Since, the band structure calculation is based on the atomic structure of the material, the study of graphene band structure is first studied and then the same method is applied for carbon nanotubes.

To understand the physical properties of carbon nanotubes, a linear combination of atomic orbitals (LCAO) method is provided, also called tight-binding method based on Bloch's theory. CNTs can be seen as a rolled graphene sheet [11], [14]-[16]. The graphene sheet is a mono-atomic layer of carbons organized in honeycomb structure as shown on Fig. 1.1.

It is possible to describe the real space of a two dimensional graphene sheet by translating a unit cell through the following vectors $\vec{T} = n\vec{a}_1 + m\vec{a}_2$ where $\vec{a}_1$ and $\vec{a}_2$ as depicted in Fig. 1.2 and *n*, *m* integers.

$$\vec{a}_1 = a_0\left(\frac{\sqrt{3}}{2}\hat{\mathrm{x}} + \frac{1}{2}\hat{\mathrm{y}}\right) \tag{1.1}$$

$$\vec{a}_2 = a_0\left(\frac{\sqrt{3}}{2}\hat{x} - \frac{1}{2}\hat{y}\right) \tag{1.2}$$

where $a_0 = \sqrt{3}a_{cc}$ is the length of the basis vector and $a_{cc} = 1.42\,\text{Å}$ is the closest neighbor Carbon-Carbon bonding distance.

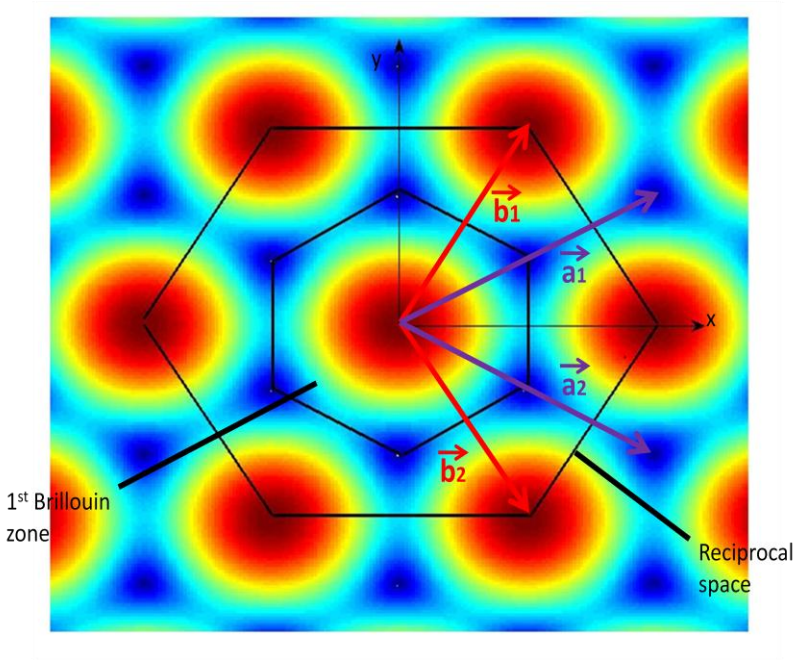

Fig. 1.2: First Brillouin zone of the reciprocal lattice

The dispersion relation $E(\vec{k})$ is derived by solving the eigenvalues of the Hamiltonian matrix for a crystal as shown in [16].

$$H(\vec{k}) = \pm\gamma_0 \begin{bmatrix} 0 & 1 + e^{j\vec{k}\,.\,\vec{a}_1} + e^{j\vec{k}\,.\,\vec{a}_2} + e^{j\vec{k}\,.\,\vec{a}_3} \\ 1 + e^{-j\vec{k}\,.\,\vec{a}_1} + e^{-j\vec{k}\,.\,\vec{a}_2} + e^{-j\vec{k}\,.\,\vec{a}_3} & 0 \end{bmatrix} \quad (1.3)$$

where the overlap energy γ_0 ≈-2.9 eV is the Carbon-Carbon (C-C) bonding energy and $\vec{a}_3 = \vec{a}_1 - \vec{a}_2$.

$$E(\vec{k}) = \pm|\gamma_0| \sqrt{3 + 2\,cos(\vec{k}\,.\,\vec{a}_1) + 2\,cos(\vec{k}\,.\,\vec{a}_2) + 2\,cos(\vec{k}\,.\,\vec{a}_3)} \quad (1.4)$$

It should be noted that the positive values describe the conduction band while the negative values are used for the valence band. Thus, expression (1.4) indicates that the band structures are symmetric in case of graphene. The Fermi points or K points can be seen at the corner of the Brillouin zone represented in blue in Fig. 1.2 that describes the energy valleys in the conduction band. It may be easier to see the Fermi point on a three dimension image as shown in Fig. 1.3.

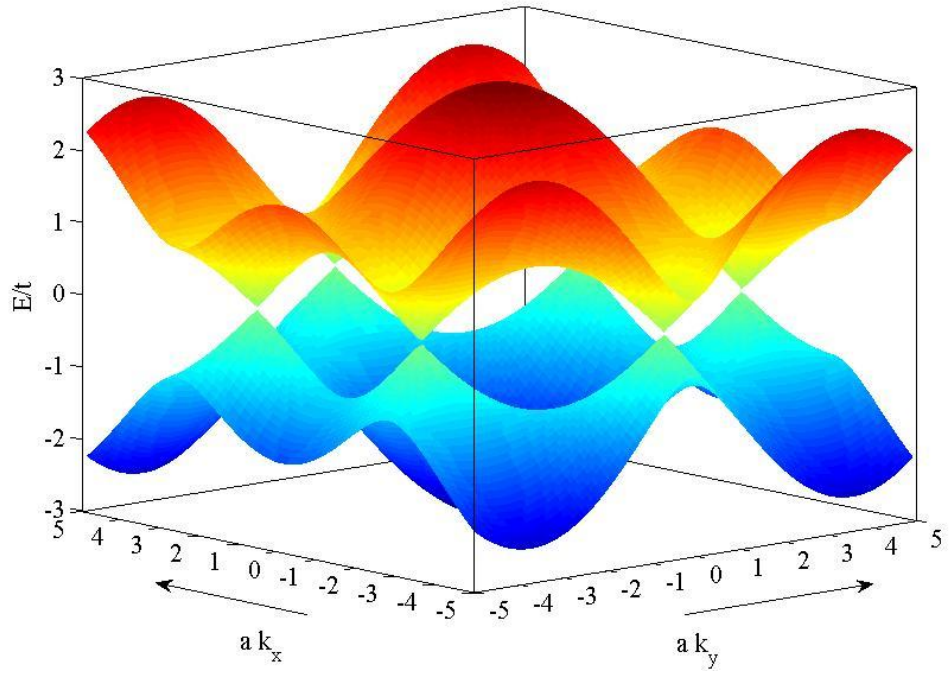

Fig. 1.3: Three dimensional plot of the band structure for graphene

From Fig. 1.2 it can be see that the relation between the basis vector of the real and the reciprocal space can be expressed as [16]:

$$\vec{a}_i \,.\, \vec{b}_j = 2\pi\delta_{ij} \tag{1.5}$$

Hence,

$$\vec{b}_1 = b_0\left(\frac{1}{2}\hat{x} + \frac{\sqrt{3}}{2}\hat{y}\right)$$
$$\vec{b}_2 = b_0\left(\frac{1}{2}\hat{x} - \frac{\sqrt{3}}{2}\hat{y}\right) \tag{1.6}$$

where $b_0 = \frac{4\pi}{\sqrt{3}a_0}$ is the length of the basis vector in the reciprocal space

By using the basis vector in the reciprocal space it is possible to compute the position of the Fermi point and shows that at this K points the Energy is 0. By using expressions (1.5) and (1.6) and substituting in (1.4) we obtained:

$$E(\vec{k}) = \pm|\gamma_0| \sqrt{3 + 2\cos\left(\pm\frac{2}{3}\pi\right) + 2\cos\left(\mp\frac{2}{3}\pi\right) + 2\cos\left(\pm\frac{4}{3}\pi\right)} = 0 \qquad (1.7)$$

This expression can be simplified using Taylor expansion of the cosine function and shows that E-k curve is isotropic around the Fermi point and indicate a linear dispersion..

$$E(\vec{k}) = \frac{3a_{cc}|\gamma_0|}{2}|\vec{k} - \vec{k}_F| \qquad (1.8)$$

where $\vec{k}_F = \left(u \pm \frac{1}{3}\right)\vec{b}_1 + \left(v \mp \frac{1}{3}\right)\vec{b}_2$ and *u* and *v* are integers.

Similarly, the carbon nanotubes physical properties can be obtained by translating a unit cell through $\vec{c} = n\vec{a}_1 + m\vec{a}_2$ where $\vec{a}_1$ and $\vec{a}_2$ are the bases vectors of the graphene sheet and n, m are integers shown in Fig. 1.2. Depending on their chirality different electric properties appeared (semiconducting or conducting). There are three types of carbon nanotubes as shown on Fig. 1.4; armchair when n=m; zigzag when m=0; chiral otherwise.

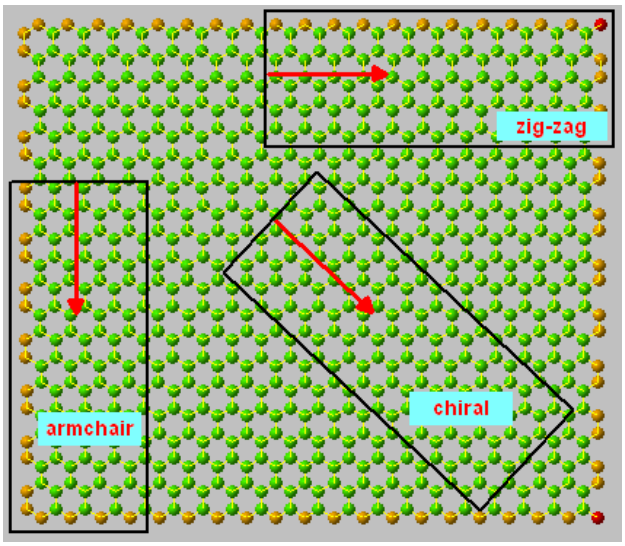

Fig. 1.4: picture illustrating the different way to roll the graphene sheet to obtained different carbon nanotubes based on their chirality, retrieved from http://academic.pgcc.edu/~ssinex/nanotubes/.

The rolled graphene sheet introduces a periodic cylindrical boundary condition allowing us to write another constraint [16]:

$$\vec{k}.\vec{c} = 2\pi q \tag{1.9}$$

where $\vec{k}$ is an allowed vector and q the quantum number.

As previously seen for a graphene sheet, we can choose a specific Fermi point as

$$\vec{k}_F = \left(u \pm \frac{1}{3}\right)\vec{b}_1 + \left(v \mp \frac{1}{3}\right)\vec{b}_2 \tag{1.10}$$

where u=0 and v=0 and compute its components along the circumference direction

$$\vec{k}_F \,.\, \vec{c} = \; 2\pi \; \frac{n-m}{3} \tag{1.11}$$

Then by changing the origin of reciprocal space as the chosen Fermi point, we can describe in the new coordinate system as [16]:

$$\overrightarrow{k'} = \vec{k} - \vec{k}_F \; = \; k'_c \, \hat{c} + k'_t \, \hat{t} \tag{1.12}$$

where k'_c is the component along the circumference direction which can be quantized by using the periodic boundary condition as:

$$k'_{c,q} = \left(\vec{k} - \vec{k}_F\right) . \hat{c} = \frac{\vec{k} \,.\, \vec{c} - \overrightarrow{k_F} \,.\, \vec{c}}{|\vec{c}|} = \frac{1}{3d}[3q - (n-m)] \tag{1.13}$$

where d is the diameter of the CNT.

From (1.8) of the E-k relation found for graphene, we can write

$$E(\vec{k}) = \frac{3a_{cc}|\gamma_0|}{2}\left|\vec{k} - \vec{k}_F\right| = \pm\frac{3a_{cc}|\gamma_0|}{2}\sqrt{{k'_{c,q}}^2 + {k'_t}^2} \tag{1.14}$$

It should be noted that the lowest sub-band of the CNT is controlled by $\left|k'_{c,q}\right|$ whether (n-m) is multiple of 3.

- If (n-m) is a multiple of 3, a linear relation for metallic carbon nanotubes is expressed and plotted in Fig. 1.5.

$$E(\vec{k}) = \pm \frac{3a_{cc}|\gamma_0|}{2} k'_t \tag{1.15}$$

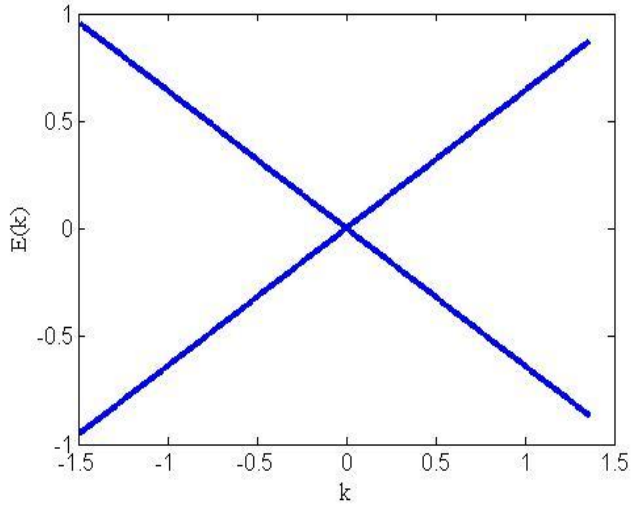

Fig. 1.5: linear E-k relation for conducting carbon nanotubes obtained from (1.15).

Consequently, the one dimension density of states of the lowest sub-band of the metallic CNT is constant which is coherent with the general expression described for quantum wire in [13]-[16].

$$D(E) = 2\ x\ 2\ x \frac{1}{L} \delta[E - E'(\Delta k_t)] = \frac{8}{3\pi a_{cc}|\gamma_0|} \tag{1.16}$$

- If (*n*-*m*) is not a multiple of 3, semi-conducting CNT are obtained and the lowest sub-band in this case is:

$$k'_{c,q} = \frac{2}{3d} \tag{1.17}$$

where *d* is the diameter of the carbon nanotube.

By substituting (1.17) in (1.14), the linear E-k relation can be computed as

$$E(\vec{k}) = \pm \frac{3a_{cc}|\gamma_0|}{2} \sqrt{\left(\frac{2}{3d}\right)^2 + {k'_t}^2} \tag{1.18}$$

It is interesting to mention that the band gap of semiconducting carbon nanotubes mainly depends on the diameter *d* in nm as:

$$E_G = \frac{2a_{cc}|\gamma_0|}{d} \approx \frac{0.8eV}{d} \tag{1.19}$$

In addition, the 1D density of state (DOS) for semiconducting CNT can be derived as [13] and shown in Fig. 1.6, assuming a (13, 0) semiconducting carbon nanotube.

$$D(E) = 2x2x\frac{1}{L}\sum_{\Delta k_t}\delta\left[E - E^{'(\Delta k_t)}\right] = D_0\frac{|E|}{\sqrt{E^2 - (E_G/2)^2}}\Theta(|E| - E_G/2) \tag{1.20}$$

where $D_0 = \frac{8}{3\pi a_{cc}|\gamma_0|}$ is constant metallic band DOS and Θ the step function defined as

$$\Theta = \begin{cases} 1 \; when \; |E| - \frac{E_G}{2} > 0 \\ 0 \; otherwise \end{cases}.$$

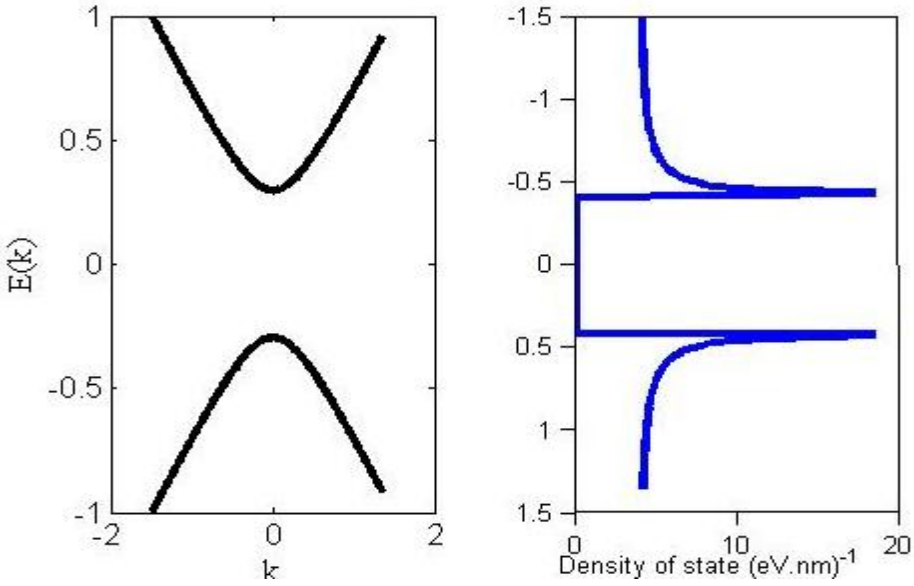

Fig. 1.6: Energy band gap and DOS of (13,0) semiconducting carbon nanotubes.

C. GROWTH OF CARBON NANOTUBES

The earliest research was focus on the synthesis of CNTs including several growth techniques such as arc discharge (1991) and laser ablation (1992) of graphite pieces and later chemical vapor deposition (CVD) (1993) and plasma enhanced CVD has significantly improved the quantity as well as the quality of the CNTs [17]. In the last decade many companies have concentrated their efforts to develop and control those growth techniques to insure very high purity and uniform CNTs in length and diameter at a reasonable cost [17].Carbon nanotube networks are usually present in a dry powder form which consists of 1:2 ratio where 1/3 of metallic CNTs is randomly mixed with 2/3 of semiconducting nanotubes [18].

In 2006, manufacturers have focused their interest on producing very high purity carbon nanotubes suspended in an aqueous solution to facilitate their deposition/implementation into electronic components. Although the cost is still high, it is now possible to buy high purity (single or multi-walled) CNTs highly uniform, owing the same electrical properties (conducting or semiconducting). The process to select the desired tube in a solution involves density gradient ultracentrifugation (DGU) and chemical reactions [19]-[20]. The key for future implementation of carbon based devices is to be able to select the carbon nanotubes based on its electrical nature.

D. MATERIAL CHARACTERIZATION AT MICROWAVE FREQUENCIES

Before developing novel high frequency carbon based electronic devices, it is necessary to characterize carbon nanotubes, i.e. finding the electrical parameters that help to understand the behavior of the nanotubes under an electromagnetic field.

The applied electric field $\vec{E}$ in a dielectric medium induces the polarization of the particles/atoms of the material which causes electric dipole moments that enhances the total displacement flux $\vec{D}$ as:

$$\vec{D} = \varepsilon_0 \vec{E} + \vec{P_e} \tag{1.21}$$

where $\vec{P_e}$ is the electric polarization vector created by the rearrangement of the charged particles in the dielectric medium and $\varepsilon_0 = 8.854 \times 10^{-12}$ is the permittivity of free space. The contribution of the electric polarization vector can be written as:

$$\vec{P_e} = \varepsilon_0 \chi_e \vec{E} \tag{1.22}$$

where the complex number χ_e is the electric susceptibility of the dielectric material which indicates the degree of polarization of a material submitted to an electric field.

By substituting the electric polarization expression into the definition of the electric flux, we obtain,

$$\vec{D} = \varepsilon_0 (1 + \chi_e)\vec{E} = \varepsilon \vec{E} \tag{1.23}$$

where the complex permittivity or the electric property of the material is described by

$$\varepsilon = \varepsilon' - j\,\varepsilon'' = \varepsilon_0 (1 + \chi_e) \tag{1.24}$$

So the electrical characterization of a material under test (MUT) at microwave frequencies consists of extracting the quantitative value of the complex permittivity. The real part of the complex permittivity is also known as dielectric constant at low frequency (below 1 MHz), while the imaginary part of the permittivity is related to the dielectric losses or conductivity of the medium. Several high frequency techniques exist to obtain the complex permittivity of material under test [21]. The extraction techniques are usually classified into two categories: resonant methods and non resonant approaches. Although resonant techniques are usually more accurate, the extraction method is limited to a narrow frequency band. The material property characterization is an important area in the microwave community and several review papers in this field have been published [21]-[25].

The non-resonant methods include two different kind of measurement using the reflection methods or the transmission/reflection methods. The measurements consist of radiating electromagnetic waves into the material under test (MUT) and study the reflected and transmitted power at the material interface known as scattering parameters (S-parameters). From those reflection and transmission coefficients, the electrical properties of MUT can be extracted.

E. STATE OF THE ART

Material characterization is a necessary step to understand the material behavior exposed to an external electromagnetic field. Materials in a powder form are challenging as common extraction techniques usually involves solid media and are limited in frequency. Therefore, in 2003, Watts *et al.* characterized from 8 to 12 GHz (X band) various carbon nanotubes incorporated into polystyrene films [26] placed in rectangular waveguide. Then, Potschke *et al.* extracted the dielectric constant and AC conductivity of polycarbonate-multiwalled CNTs from DC to a few MHz [27]. The work highlights the importance of samples preparation and a discussion is provided to explain the experimental results based on the percolation theory which is also confirmed by Sandler *et al.* and Kim *et al.* demonstrating an ultra-low electrical percolation threshold in carbon-nanotube-epoxy composites [28]-[29]. For instance, Grimes *et al.* characterized carbon nanotubes embedded in a thick-film poly-ethyl methacrylate polymer from 500 MHz to 5.5 GHz using stripline cavity measurement setup [30].

Experimental results show an enhancement of the real part of the relative permittivity by a factor of ~35 and an increase by a factor of 1200 for the imaginary part attributed to the embedded single-walled carbon nanotubes effect. Later, the same group showed the effect of purification of the electrical conductivity and complex permittivity of multiwall carbon nanotubes [31].

A net decrease of the complex permittivity and conductivity for purified carbon nanotube samples is observed (2.22 x 10^{-4} S/m) compared to the conductivity of unpurified samples (7.78 x 10^{-4} S/m) which is attributed to the removed residual metallic catalyst such as Nickel and Yttrium used in the growth process. Those experiments highlight the fact that the characterization of carbon nanotubes can be highly influenced by the presence of metallic impurities and therefore, the electrical properties depend on the growth and the carbon nanotubes sample preparation. Similarly, Wu and Kong have extracted the complex permittivity of composites material consisting of multi-walled carbon nanotubes dispersed in epoxy considering different mass concentration from 10 MHz to 20 GHz [32]. Although large values for both the real and imaginary complex permittivity part are presented, the values decrease rapidly with frequency in the MHz range. According to the authors based on experiments and theoretical simulations, the dielectric mechanisms occurring inside the composite material can be explained through its intrinsic property such as the dielectric relaxation/resonance and electron motion. Moreover, in 2007, Liu *et al.* studied the microwave absorption of single-walled carbon nanotubes/soluble cross-linked polyurethane composites using a transmission/reflection coaxial line method from 2 GHz to 18 GHz [33]. The method consists to introduce the composite slab between two coaxial cables and studied the reflection and transmission coefficients. The results reported in the paper present again relatively high values of the complex permittivity which continuously increases with the concentration of single-walled present in the dielectric medium [33]. The same year, Liu *et al.* reported the frequency and concentration dependence of complex permittivity of single, multi-walled carbon nanotubes and carbon black powder blended in a epoxy medium using a coaxial air-line and impedance methods from 0.1 to 10 GHz [34]. The CNT-based possible high frequency applications are presented by Bednarz *et al.* who observed

from 40 MHz to 40 GHz new absorbing and shielding composites properties where CNTs are dispersed in a polymer dielectric material [35]. The high-aspect-ratio of the nanotubes enhances shielding efficiency which can be achieved with a lower carbon nanotubes concentration compared to the common carbon powder used. In 2007, Xu *et al.* computed microwave shielding of transparent and conducting single-walled carbon nanotubes films using open coaxial technique also known as Corbino technique from 10 MHz to 30 GHz based on the real and imaginary part of the complex permittivity [36]. Although all those results are more or less consistent showing very large values of the complex permittivity at microwave frequencies some discrepancies seem to occur due the composite/thin film preparation. Our goal instead is to characterize carbon nanotubes in a powder form as provided by the furnisher from 10 MHz to 50 GHz which is the frequency band available of our network analyzer. By reducing the preparation sample effects and characterizing only carbon nanotubes networks, we expect to enhance the accuracy of the extracted data which can be implemented in commercial software to improve simulation models for radio frequency (RF) /microwave applications.

F. DISSERTATION CONTRIBUTION AND SIGNIFICANCE

Extensive work has been previously performed to characterize carbon nanotubes embedded in a host medium. However, those types of characterization are limited in frequency band and the results are highly dependent of samples preparation which explains the discrepancies that appears in the literature. In this work, instead the complex permittivity extraction is achieved over a wide frequency band from 10 MHz to 50 GHz and no sample preparation is involved. The characterization technique easily implemented is none destructive; it means that carbon nanotubes can be reused without alteration. The extraction technique has been validated with different materials and then applied to CNT networks.

The beauty of the technique is that it can be used for material characterization in a solid, liquid or powder form and composites material as well. The electrical property extractions of carbon nanotubes in a pulverized form are realized and different mixture of CNT-based are evaluated for electromagnetic compatibility (EMC) applications and electromagnetic interference (EMI) shielding. Mathematical model and explanation are provided based on experimental results to improve simulations software and offer a better understanding of the material behavior submitted to an external electrical field.

This dissertation is organized as shown in Fig. 1.7: Chapter 2 explains the measurement setup used in this work to extract the complex permittivity through theoretical and experimental studies. The validation of the technique is realized by comparing the results with common commercial simulation software and is then experimentally applied to known lossless and lossy materials. Chapter 3 presents the experimental results for unaltered carbon nanotubes networks in a dry power form. Chapter 4 describes the experimental results of different CNTs based composites material and provides a physical explanation of the high values obtained for carbon nanotubes networks. Chapter 5 describes a technique to fully exploit the electrical properties of the carbon nanotubes by considering their alignment using a dielectrophoresis method. Finally, Chapter 6 concludes this work and a discussion about our future work direction is provided.

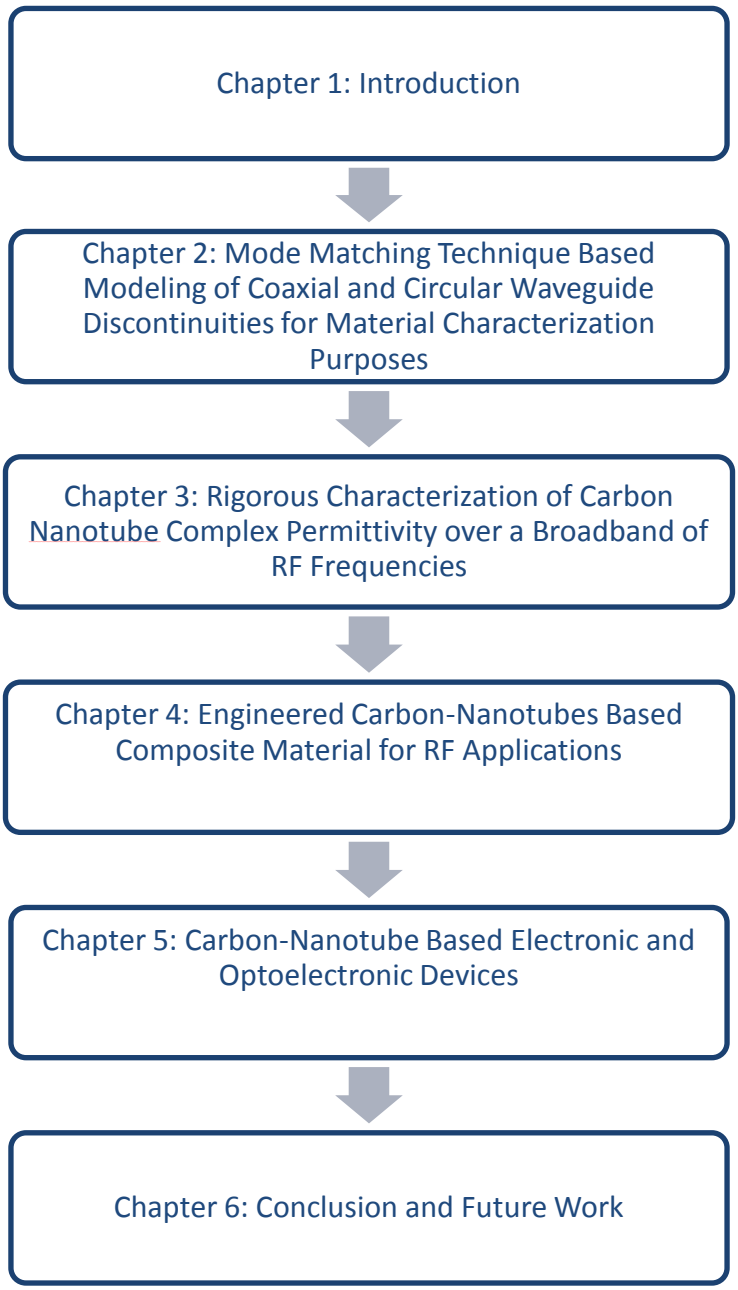

Fig. 1.7: Flow chart of dissertation organization.

II. MODE MATCHING TECHNIQUE BASED MODELING OF COAXIAL AND CIRCULAR WAVEGUIDE DISCONTINUITIES FOR MATERIAL CHARACTERIZATION PURPOSES[1]

A. INTRODUCTION

The design of new radio frequency (RF)/microwave components involves a series of simulations to be able to predict the behavior of the circuits or waveguide. Thus, modeling waveguide discontinuities or transitions can be achieved using meshed configuration such as Finite element methods (FEMs) or Finite Difference Time Domain (FDTD) techniques. However, those techniques commercially available in most simulation software require expensive computing time and resources. In addition, model solvers predict the results, i.e. compute the scattering parameters when the physical properties of the material are known. In our case, the problem is an inverse problem because the material properties are unknown, yet the S-parameters can be measured. Consequently, instead of using a meshed configuration to model waveguides discontinuities, the full-wave mode matching technique (MMT) is preferred. Each discontinuity is cascaded through transmission line intermediate blocks to fully characterize a microwave structure composed of coaxial and circular waveguides. The technique involves the computation of the electromagnetic field components on each side of the discontinuity and uses the orthogonality properties of the wave functions. So, to solve the inverse problem, i.e. finding the complex permittivity of a medium measuring the S-parameters, an iterative technique is implemented. Thus, the unknown complex permittivity is the tuned parameter that varies until the measured S-parameters matched the simulated ones obtained from MMT.

---

[1] © Cambridge University Press (2011). Reprinted, with permission, from E. Decrossas, M.A. EL Sabbagh, V. Fouad Hanna and S.M. El-Ghazaly, "Mode Matching Technique Based Modeling of Coaxial and Circular Waveguide Discontinuities for Materials Characterization Purposes" *Int. Journal Microw. Wireless Technologies*, vol. 3, no.6, pp. 679-690, Sept. 2011.

The extraction method has been successfully validated in case of lossless material such as air and lossy material like water at room temperature over a wide frequency band [37]-[38]. Agilent developed an open-ended coaxial probe measurement [39]. However, the measurements are highly sensitive to surface roughness as the measurements are limited to the skin depth of the material under test (MUT). In our case the MUT filled a circular waveguide shorted at the end, so electromagnetic waves propagate inside the material and then are reflected at the end. In addition, for powder characterization it is easier to control the packing density of the powder inside the confined volume defined by the circular waveguide dimensions. Whinnery *et al.* provide formulae to model coaxial discontinuities based on the computation of the admittance of the fundamental mode added to the contribution from higher order modes [40]. From this work, an extraction technique is developed where the measured admittance is compared to the simulated one then iterative technique is implemented to change the permittivity components [41]. However, the technique is limited in frequency to 18 GHz due to size of the connector. In this work instead the scattering parameters are used instead of the admittance measurement and different formulae are derived by describing each discontinuity with its generalized scattering matrix (GSM) [42]-[46]. The discontinuity model is highly accurate as excited propagating and evanescent higher modes are considered. The reflection coefficient is computed by cascading the self-inner and mutual inner product matrices. By considering perfect inner and outer conductor and neglecting the surface roughness of the surface to define the coaxial and circular waveguide, it is possible simplified the model without losing resolution. The extraction process is validated through a series of simulations and compared to data obtained from the finite element methods using HFSS software [47] as well as microwave measurements.

B. DESCRIPTION OF THE TEST SETUP

The fabricated test structure consists of cylindrical waveguide shorted at the end connected to the network analyzer via a 1.85 mm (female (F)) to 2.4 mm (male (M)) precision adapter as shown in Fig. 2.1 and Fig. 2.2. The structure is then modeled as a series of regions: 1) The 1.85 mm female part of the adapter is modeled as a 50-Ω coaxial waveguide filled with air. 2) The 2.4 mm male part of the connector is simulated as coaxial waveguide filled with unknown material under test. 3) The circular waveguide ended by a short circuit filled with MUT. Each discontinuity encountered by electromagnetic waves is described by its generalized scattering matrix building blocks as shown in Fig. 2.2 (b). The coaxial first discontinuity is represented by the GSM $\mathbf{S}^{\mathbf{coax-coax}}$. Then the length L_1 of the coaxial with characteristic impedance $\boldsymbol{Z}_{\mathbf{coax2}}$ filled with MUT is modeled as a phase delay matrix. The second discontinuity between the coaxial and circular waveguide is represented by the GSM $\mathbf{S}^{\mathbf{coax-circ}}$. Finally the waves propagate along the circular waveguide with a characteristic impedance $\boldsymbol{Z}_{\mathbf{circ}}$ and length L_2 and are reflected back. The beauty of the structure is that the calibration plane or reference plane coincide with the first discontinuity at the surface of the material under test to remove any phase ambiguity [48].

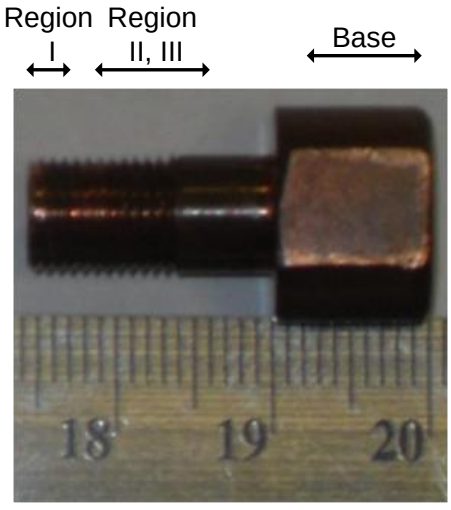

Fig. 2.1: Picture of the fabricated testing structures. Regions I, II, and III are the same as those shown in the schematic of Fig. 2.2.

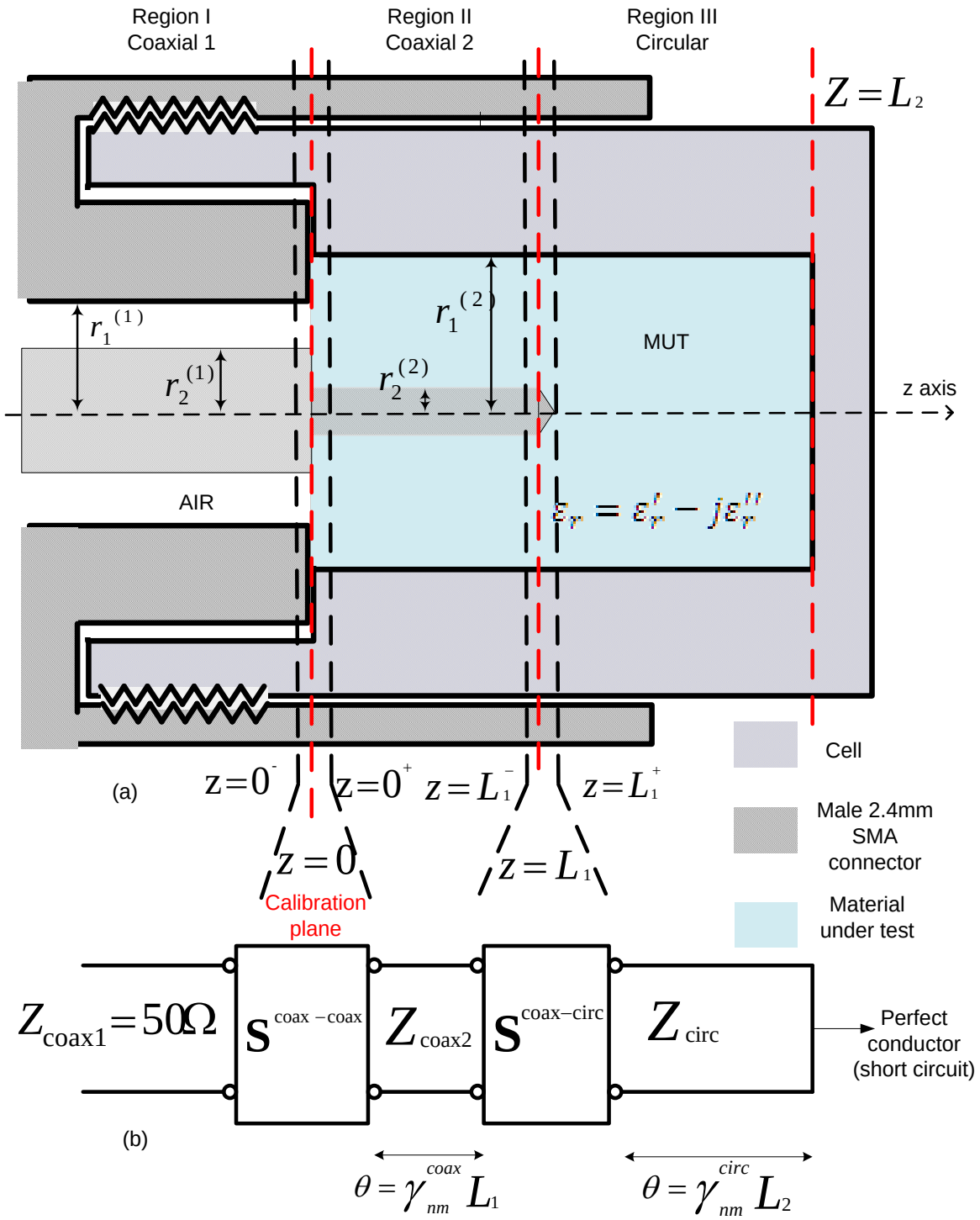

Fig. 2.2: (a) Schematic of the test structure. Dimensions of design parameters are: $r_1^{(1)}$= 1.2 mm,$r_2^{(1)}$ = 0.52 mm, $r_1^{(2)}$= 1.26 mm, $r_2^{(2)}$= 0.254 mm, L_1 = 1.1 mm, L_2 = 5 mm. (b) Microwave circuit model of test structure based on Generalized scattering matrices building blocks.

C. FULL-WAVE MODELING OF TEST STRUCTURE

1. Eigenmodes

The fundamental mode of coaxial waveguide is transverse electromagnetic (TEM), yet it also supports transverse magnetic(TM) and transverse electric (TE) higher order modes. Circular waveguides supports only TM and TE modes. Field components inside circular waveguides and TEM mode in coaxial waveguides are given in [49]. The only difference between the TM and TE modes field components in coaxial compared to circular waveguides is the contribution of Bessel functions of second kind, also called Neumann functions to describe the field close to the inner conductor in a coaxial transmission lines. Appendix A describes the expressions of electric and magnetic field components in a coaxial waveguide used in this work. It should be noted that the superscript numbers in parenthesis refers to the region shown in Fig. 2.2 and bold style is used for matrix or vectors notation.

2. Generalized Scattering Matrices

Let's consider a general waveguide discontinuity as shown in Fig. 2.3 where the input cross section S_1 is smaller than the output cross section S_2 and a wave propagates from region 1 to region 2 along *z* axis.

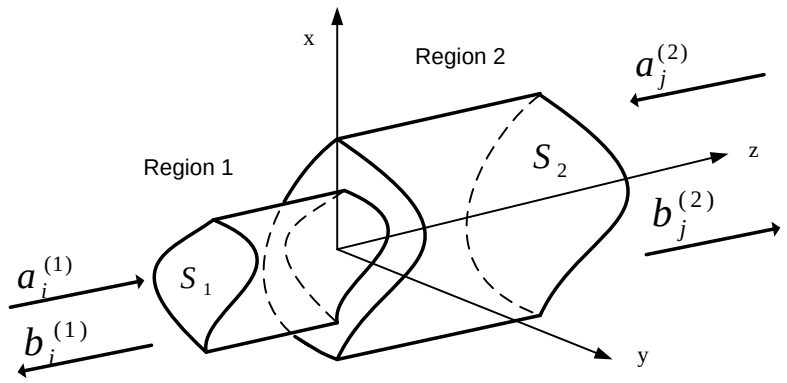

Fig. 2.3: Cross section of a general discontinuity: S_1 is the input smaller cross section of region 1 and S_2 represents the output larger cross section of region 2.

Each side of the discontinuity is described by the summation of the incident and reflected field coefficient $\left(a_i^{(l)}, b_i^{(l)}\right)$ of i^{th} mode in l^{th} region where $\in \{1,2\}$. Then, by matching the total electric and magnetic fields contribution considering the adequate boundary conditions a set of formulae is solved by using the orthogonality properties of the electric and magnetic fields:

- Continuity of tangential electric field at $z = 0$

$$\sum_{j=1}^{\mathrm{J}}\left(a_j^{(2)} + b_j^{(2)}\right)\vec{e}_j^{(2)}(r,\phi) = \begin{cases} \sum_{i=1}^{\mathrm{I}}\left(a_i^{(1)} + b_i^{(1)}\right)\vec{e}_i^{(1)}(r,\phi) \text{ on } S_1 \\ 0 \qquad\qquad\qquad\qquad \text{on } S_2 - S_1 \end{cases} \tag{2.1}$$

- Continuity of tangential magnetic field at $z = 0$

$$\sum_{j=1}^{\mathrm{J}}\left(-a_j^{(2)} + b_j^{(2)}\right)\vec{h}_j^{(2)}(r,\phi) = \sum_{i=1}^{\mathrm{I}}\left(a_i^{(1)} - b_i^{(1)}\right)\vec{h}_i^{(1)}(r,\phi) \text{ on } S_1 \tag{2.2}$$

where $\left(\vec{e}_i^{(k)}, \vec{h}_i^{(k)}\right)$ are the tangential electric and magnetic fields of the i^{th} mode in k^{th} region with $k \in \{1,2\}$ and $\left(a_i^{(k)}, b_i^{(k)}\right)$ represents the corresponding field coefficients of incident and reflected waves. It should be noted that in theory a discontinuity excites infinite number of modes, yet in practice the number is truncated to *I* modes in region 1 and *J* modes in region 2 as shown in (2.1) and (2.2).

The continuity of tangential electric field (2.1) is tested on both sides by the magnetic field intensity of the larger cross section, region 2. Similarly, the continuity tangential magnetic expression (2.2) is tested on both sides by the electric field intensity of the smaller cross section of region 1. In [43], it has been demonstrated that testing both sides of the continuity tangential expressions with either the magnetic or electric intensity is equivalent. By rearranging the cross product expressions in a matrix forms, we obtained:

$$\boldsymbol{\lambda}^{(2)}\left(\boldsymbol{a}^{(2)}+\boldsymbol{b}^{(2)}\right)=\mathbf{M}\left(\boldsymbol{a}^{(1)}+\boldsymbol{b}^{(1)}\right) \tag{2.3}$$

$$\mathbf{M^t}\left(-\boldsymbol{a}^{(2)}+\boldsymbol{b}^{(2)}\right)=\boldsymbol{\lambda}^{(1)}\left(\boldsymbol{a}^{(1)}-\boldsymbol{b}^{(1)}\right) \tag{2.4}$$

where vectors $\boldsymbol{a}^{(1)}$and $\boldsymbol{b}^{(1)} \in \mathbb{C}^{I\times 1}$, $\boldsymbol{a}^{(2)}$and $\boldsymbol{b}^{(2)} \in \mathbb{C}^{J\times 1}$ represent the incident and reflected field coefficients in regions 1 and 2 respectively as shown in Fig. 2.3. The matrix $\boldsymbol{\lambda}^{(2)} \in \mathbb{C}^{J\times J}$ represents the matrix of self inner products for region 2 and its elements are given as

$$\int_{S_2} \vec{e}_j^{(2)}(r,\phi)\times\vec{h}_j^{(2)}(r,\phi).r\,dr\,d\phi\,\hat{a}_z=\lambda_{jj}^{(2)} \tag{2.5}$$

where $j \in \{1,2,\dots,J\}$ and $\hat{a}_z$ is the unit vector. M $\in \mathbb{C}^{J\times I}$ is the matrix of mutual inner products between region 1 and 2.

$$\int_{S_1} \vec{e}_i^{(1)}(r,\phi)\times\vec{h}_j^{(2)}(r,\phi).r\,dr\,d\phi\,\hat{a}_z=M_{ji} \tag{2.6}$$

The matrix $\mathbf{M^t} \in \mathbb{C}^{I\times J}$, the superscript "t" denotes the matrix transpose. The diagonal matrix $\boldsymbol{\lambda}^{(1)} \in \mathbb{C}^{I\times I}$ is the self inner product of region 1 and its elements are given as

$$\int_{S_1} \vec{e}_i^{(1)}(r,\phi)\times\vec{h}_i^{(1)}(r,\phi).r\,dr\,d\phi\,\hat{a}_z=\lambda_{ii}^{(1)} \tag{2.7}$$

where $i \in \{1,2,\dots,I\}$.

The generalized scattering matrix modeling the discontinuity between regions 1 and 2 in Fig. 2.3 is obtained by rearranging (2.3) and (2.4):

$$\begin{bmatrix}\boldsymbol{b}^{(1)}\\ \boldsymbol{b}^{(2)}\end{bmatrix}=\begin{bmatrix}\mathbf{S_{11}} & \mathbf{S_{12}}\\ \mathbf{S_{21}} & \mathbf{S_{22}}\end{bmatrix}\begin{bmatrix}\boldsymbol{a}^{(1)}\\ \boldsymbol{a}^{(2)}\end{bmatrix} \tag{2.8}$$

where

$$\begin{aligned}\mathbf{S_{11}} &= (\mathbf{U}+\mathbf{R\,T})^{-1}(\mathbf{U}-\mathbf{R\,T}) && \in \mathbb{C}^{I\times I}\\ \mathbf{S_{12}} &= (\mathbf{U}+\mathbf{R\,T})^{-1}\ \mathbf{2\,R} && \in \mathbb{C}^{\mathrm{I}\times J}\\ \mathbf{S_{21}} &= (\mathbf{U}+\mathbf{T\,R})^{-1}\,\mathbf{2\,T} && \in \mathbb{C}^{J\times \mathrm{I}}\\ \mathbf{S_{22}} &= (\mathbf{U}+\mathbf{T\,R})^{-1}(\mathbf{T\,R}-\mathbf{U}) && \in \mathbb{C}^{J\times J}\end{aligned} \tag{2.9}$$

$\mathbf{R} \in \mathbb{C}^{I\times J}$, $\mathbf{T} \in \mathbb{C}^{J\times I}$ are defined as $\mathbf{R} = \boldsymbol{\lambda}^{(1)^{-1}}\mathbf{M}^{\mathbf{t}}$ and $\mathbf{T} = \boldsymbol{\lambda}^{(2)^{-1}}\mathbf{M}$. **U** is the identity matrix.

It is noted that this is a general formulation describing a discontinuity between any two waveguides with different cross sections where the only assumptions is that the input cross section is smaller than the output cross section independently of the waveguide (coaxial, circular, rectangular).

The electric and magnetic field components and eigenmodes are determined by the boundary conditions or in other words, the shape of the waveguide. In the structure presented in Fig. 2.3, the generalized scattering matrices are computed for coaxial to coaxial discontinuity and coaxial to circular.

3. Coaxial to Coaxial Discontinuity

As shown in Fig. 2.2(a), the first discontinuity encounter by an incident waves is a coaxial to coaxial transition where region 1 is modeled as a coaxial 50-Ω filled with air while region 2 corresponding to the probe of the 2.4mm male part protruding in a circular waveguide filled with the MUT can also be modeled as a coaxial waveguide with a different cross section. Based on the field components given in the appendix A, the self and mutual inner products are derived. Bessel functions are used to describe the waves propagating in a circular or coaxial waveguides [50].

Self-Inner Product

Self-inner products for a coaxial waveguide are given below:

$$\lambda^{(\mathrm{i})\mathrm{TEM}-\mathrm{TEM}} = 2\pi\frac{k^{(i)}}{\omega\mu}\ln\left(\frac{r_1^{(i)}}{r_2^{(i)}}\right) \tag{2.10}$$

$$\lambda_{nmnm'}^{(\mathrm{i})\mathrm{TM}-\mathrm{TM}}$$

$$= \begin{cases} \mathrm{E}\,\varepsilon^{(i)} \begin{Bmatrix} \mathrm{I}_1 \\ \mathrm{I}_2 \end{Bmatrix} \left\{ {r_1^{(i)}}^2 \left[Z_{n+1}^2 \left(k_{\mathrm{c}_{nm}}^{(\mathrm{i})\mathrm{TM}} r_1^{(i)} \right) \right] - {r_2^{(i)}}^2 \left[Z_{n+1}^2 \left(k_{\mathrm{c}_{nm}}^{(\mathrm{i})\mathrm{TM}} r_2^{(i)} \right) \right] \right\} & , m = m' \,\&\, n = n' \\ 0 & , m \neq m' \text{or } n \neq n' \end{cases} \tag{2.11}$$

$$\lambda_{nmnm'}^{(\mathrm{i})\mathrm{TE}-\mathrm{TE}}$$

$$= \begin{cases} \mathrm{E}\,\mu^{(i)} \begin{Bmatrix} \mathrm{I}_1 \\ \mathrm{I}_2 \end{Bmatrix} \left[{r_1^{(i)}}^2 \mathrm{F}\, Z_n^2 \left(k_{\mathrm{c}_{nm}}^{(\mathrm{i})\mathrm{TE}} r_1^{(i)} \right) - {r_2^{(i)}}^2 \mathrm{G}\, Z_n^2 \left(k_{\mathrm{c}_{nm}}^{(\mathrm{i})\mathrm{TE}} r_2^{(i)} \right) \right] & , m = m' \text{and } n = n' \\ 0 & , m \neq m' \text{or } n \neq n' \end{cases} \tag{2.12}$$

where $\mathrm{E} = \frac{1}{2} \frac{\gamma_{nm}^{(\mathrm{i})\mathrm{TM}}}{k_{\mathrm{c}_{nm}}^{2\,(\mathrm{i})\mathrm{TE}}} j\omega$ $\quad \mathrm{F} = \left(1 - \frac{n^2}{k_{\mathrm{c}_{nm}}^{2\,(\mathrm{i})\mathrm{TE}} {r_1^{(i)}}^2} \right)$ $\quad \mathrm{G} = \left(1 - \frac{n^2}{k_{\mathrm{c}_{nm}}^{2\,(\mathrm{i})\mathrm{TE}} {r_2^{(i)}}^2} \right)$

$$i = 1, 2 \text{ to describe region 1 or 2}$$

$$\mathrm{I}_1 = \begin{cases} 2\pi & , n = n' = 0 \\ \pi & , n = n' \neq 0 \text{ for PEW} \\ 0 & , n \neq n' \end{cases}$$

$$\mathrm{I}_2 = \begin{cases} 0 & , n = n' = 0 \\ \pi & , n = n' \neq 0 \text{ for PMW} \\ 0 & , n \neq n' \end{cases}$$

$\varepsilon^{(i)}$and $\mu^{(i)}$ are the permittivity and permeability, respectively, in region (i) where $i \in \{1,2\}$. It should be noted that there is no coupling between hybrid modes due to the assumption of perfect conducting boundary conditions and the orthogonality properties of the Bessel, sine and cosine functions. The outer and inner radii of the coaxial in region (i) are respectively denoted as $r_1^{(i)}$ and $r_2^{(i)}$, as shown in Fig. 2.2 (a). The cutoff constants are expressed as $k_{\mathrm{c}_{nm}}^{(\mathrm{i})\mathrm{TM}}$ for TM_{nm} modes, $k_{\mathrm{c}_{nm}}^{(\mathrm{i})\mathrm{TE}}$ for TE_{nm} modes, and $k^{(i)}$ for the fundamental TEM mode as derived in appendix A. Similarly, the propagation constant for the TM_{nm} and TE_{nm} are expressed as $\gamma_{nm}^{(\mathrm{i})\mathrm{TM}}$and $\gamma_{nm}^{(\mathrm{i})\mathrm{TE}}$. The cylindrical shape of the coaxial waveguide helps to introduce two different symmetric plans as represented the perfect electric wall (PEW) and perfect magnetic wall (PMW) conducting to different expressions of the self inner product expressions.

Mutual Inner Product

The coaxial waveguide support 3 modes of propagation TEM, TM_{nm} and TE_{nm}, all possible combinations are considered. However, due to the orthogonality properties of the sine, cosine and Bessel functions only four possible combinations are allowed. Analytical analysis performed shows that an incident TEM fundamental mode in region 1 can only couple with TEM and TM_{0m} modes in region 2.

$$\mathrm{M}^{\mathrm{TEM(1)-TEM(2)}} = 2\pi \frac{k}{\omega\mu} \ln\left(\frac{r_1^{(1)}}{r_2^{(1)}}\right) \tag{2.13}$$

$$\mathrm{M}_{nm}^{\mathrm{TEM(1)-TM(2)}} = \begin{cases} -\dfrac{\mathrm{j}\omega\varepsilon^{(2)}}{k_{\mathrm{c}\,0m}^{2\,\mathrm{TM(2)}}} \begin{Bmatrix} \mathrm{J}_1 \\ \mathrm{J}_2 \end{Bmatrix} \left[\mathrm{Z}_0\left(k_{\mathrm{c}_{0m}}^{\mathrm{TM(2)}} r_1^{(1)}\right) - \mathrm{Z}_0\left(k_{\mathrm{c}_{0m}}^{\mathrm{TM(2)}} r_2^{(1)}\right)\right] & , n = 0, \forall m \\ 0 & , n \neq 0, \forall m \end{cases} \tag{2.14}$$

Finally, the mutual inner products of higher order modes are expressed as follows:

$$\mathrm{M}_{nm,n'm'}^{\mathrm{TM(1)-TM(2)}} = \begin{cases} -\mathrm{j}\omega\varepsilon^{(2)} \dfrac{\gamma_{nm}^{\mathrm{TM(1)}}}{k_{\mathrm{c}_{nm}}^{\mathrm{TM(1)}}} \begin{Bmatrix} \mathrm{I}_1 \\ \mathrm{I}_2 \end{Bmatrix} \mathrm{H}\, \mathrm{Z}_{\mathrm{n}}\left(k_{\mathrm{c}_{nm'}}^{\mathrm{TM(2)}} r_2^{(1)}\right) Z_{n+1}\left(k_{\mathrm{c}_{nm}}^{\mathrm{TM(1)}} r_2^{(1)}\right), n = n', \forall m, m' \\ 0 \qquad\qquad , n \neq n', \forall m, m' \end{cases} \tag{2.15}$$

$$\mathrm{M}_{nm,n'm'}^{\mathrm{TE(1)-TE(2)}} = \begin{cases} -j\omega\mu^{(1)} \dfrac{\gamma_{nm'}^{\mathrm{TE(2)}}}{k_{\mathrm{c}_{nm'}}^{\mathrm{TE(2)}}} \begin{Bmatrix} \mathrm{I}_1 \\ \mathrm{I}_2 \end{Bmatrix} \mathrm{H}\, \mathrm{Z'}_{\mathrm{n}}\left(k_{\mathrm{c}_{nm'}}^{\mathrm{TE(2)}} r_2^{(1)}\right) Z_n\left(k_{\mathrm{c}_{nm}}^{\mathrm{TE(1)}} r_2^{(1)}\right), n = n' \ \forall m, m' \\ 0 \qquad\qquad , n \neq n \ \forall m, m' \end{cases} \tag{2.16}$$

where

$$\mathrm{J}_1 = \begin{cases} 0 & , n \neq 0 \\ 2\pi & , n = 0 \end{cases} \text{ for PEW}$$

$$\mathrm{J}_2 = \begin{cases} 0 & , n \neq 0 \\ 0 & , n = 0 \end{cases} \text{ for PMW}$$

and

$$\mathrm{H} = \frac{r_2^{(1)}}{k_{\mathrm{c}}^{2\,\mathrm{TM/TE}(1)}_{nm} - k_{\mathrm{c}}^{2\,\mathrm{TM/TE}(2)}_{nm'}}$$

Concerning the TM and TE higher-order modes only coupling with same order *n* can be possible due to the orthogonality properties of the sine and cosine functions, independently of the order *m*. Similarly, the derivation of the self and mutual inner product refereeing to the coaxial to circular discontinuity as shown in Fig. 2.2(a) is performed in the following section.

4. Coaxial to Circular Discontinuity

The following section summarized the self and mutual inner product modeling a coaxial to circular discontinuity as shown in Fig. 2.2(a) between regions 2 and 3. As mentioned the only difference between the field components in coaxial and circular waveguide is the presence of the second kind of the Bessel function [50] to describe the field close to the inner conductor of coaxial transmission line and the TEM mode is not supported in a circular waveguide. The rigorous derivation of the mutual inner product of coaxial-circular discontinuity is given in appendix B.

Self Inner Product

Self inner products for a circular waveguide are given below:

$$\lambda_{nm,nm'}^{(3)\mathrm{TM-TM}} = \begin{cases} j\omega\varepsilon^{(3)} \dfrac{\gamma_{nm}^{\mathrm{TM}}}{k_{\mathrm{c}}^{2\,\mathrm{TM}}_{nm}} \begin{Bmatrix} \mathrm{I}_1 \\ \mathrm{I}_2 \end{Bmatrix} \dfrac{r_1^{(2)^2}}{2} J_{n+1}^2\left(k_{\mathrm{c}}^{\mathrm{TM}}_{nm} r_1^{(2)}\right) & , n = n' \text{ and } m = m' \\ 0 & , n \neq n \text{ or } m \neq m' \end{cases} \tag{2.17}$$

$$\lambda_{nm,n'm'}^{(3)\mathrm{TE-TE}}$$

$$= \begin{cases} j\omega\mu^{(3)} \dfrac{\gamma_{nm}^{\mathrm{TE}}}{k_{\mathrm{c}}^{2\,\mathrm{TE}}_{nm}} \begin{Bmatrix} \mathrm{I}_1 \\ \mathrm{I}_2 \end{Bmatrix} \dfrac{r_1^{(2)^2}}{2} \left(1 - \dfrac{n^2}{k_{\mathrm{c}}^{2\,\mathrm{TE}}_{nm} r_1^{(2)^2}}\right) J_n^2\left(k_{\mathrm{c}}^{\mathrm{TE}}_{nm} r_1^{(2)}\right), n = n' \,\&\, m = m' \\ 0 \qquad\qquad , n \neq n \text{ or } m \neq m' \end{cases} \tag{2.18}$$

Mutual Inner Product

$$\mathrm{M}_{nm}^{\mathrm{TEM(2)-TM(3)}} = \begin{cases} \dfrac{\mathrm{j}\omega\varepsilon^{(3)}}{k_{\mathrm{c}\,0m}^{2\,\mathrm{TM(3)}}} \begin{Bmatrix} \mathrm{J}_1 \\ \mathrm{J}_2 \end{Bmatrix} \mathrm{J}_0\left(k_{\mathrm{c}0m}^{\mathrm{TM(3)}} r_2^{(2)}\right) & , n = 0, \forall m \\ 0 & , n \neq 0, \forall m \end{cases} \tag{2.19}$$

$$\mathrm{M}_{nm,n'm'}^{\mathrm{TM(2)-TM(3)}}$$

$$= \begin{cases} -\mathrm{j}\omega\varepsilon^{(3)} \dfrac{\gamma_{nm}^{\mathrm{TM(2)}}}{k_{\mathrm{c}_{nm}}^{\mathrm{TM(2)}}} \begin{Bmatrix} \mathrm{I}_1 \\ \mathrm{I}_2 \end{Bmatrix} \mathrm{K}\, \mathrm{J}_n\left(k_{\mathrm{c}_{nm'}}^{\mathrm{TM(3)}} r_2^{(2)}\right) Z_{n+1}\left(k_{\mathrm{c}_{nm}}^{\mathrm{TM(2)}} r_2^{(2)}\right), n = n', \forall m, m' \\ 0 \qquad\qquad , n \neq n', \forall m, m' \end{cases} \tag{2.20}$$

$$\mathrm{M}_{nm,n'm'}^{\mathrm{TE(2)-TE(3)}}$$

$$= \begin{cases} -j\omega\mu^{(1)} \dfrac{\gamma_{nm'}^{\mathrm{TE(3)}}}{k_{\mathrm{c}_{nm'}}^{\mathrm{TE(3)}}} \begin{Bmatrix} \mathrm{I}_1 \\ \mathrm{I}_2 \end{Bmatrix} \mathrm{K}\, \mathrm{J'}_n\left(k_{\mathrm{c}_{nm'}}^{\mathrm{TE(3)}} r_2^{(2)}\right) Z_n\left(k_{\mathrm{c}_{nm}}^{\mathrm{TE(2)}} r_2^{(2)}\right) & , n = n', \forall m, m' \\ 0 & , n \neq n', \forall m, m' \end{cases} \tag{2.21}$$

where

$$\mathrm{K} = \frac{r_2^{(2)}}{k_{\mathrm{c}\,nm}^{2\,\mathrm{TM/TE(2)}} - k_{\mathrm{c}\,nm'}^{2\,\mathrm{TM/TE(3)}}}$$

and $r_1^{(2)}$ and $r_2^{(2)}$ describe respectively the radii of the outer and inner conductors of the coaxial line in region 2 shown in Fig. 2.2 (a). TM and TE higher-order modes only couple with the same order *n* and *m* due to the approximation on the perfect conducting wall and the orthogonality properties of the Bessel, sine and cosine functions. By matching the modes at the interface between the different transitions, we have modeled and computed the corresponding GSMs: $\mathbf{S}^{\mathbf{coax-coax}}$ from coaxial 1 to coaxial 2 and $\mathbf{S}^{\mathbf{coax-circ}}$ from coaxial 2 to circular waveguide as indicating in Fig. 2.2.

So, to complete the full-wave model of the entire structure, GSMs are cascaded and coaxial transmission line of length L_1 and circular transmission line of length L_2 are inserted between the transitions.

5. Cascading Generalized Scattering Matrices

The generalized scattering matrices obtained are cascaded and separated by transmission line to model the phase delay of the waves. The following section presents a general expression to cascade scattering matrices and be easily applied to any waveguide problem or any number of discontinuities.

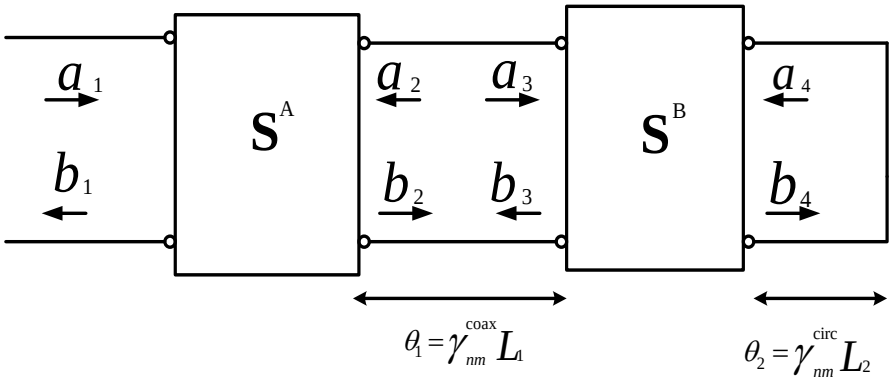

Fig. 2.4: Cascade of two generalized scattering matrices.

As presented in the previous section, vectors $\boldsymbol{a}$ and $\boldsymbol{b}$ represent the amplitude of the respective incident and reflected fields according to their modes.

The block scattering matrices can be expressed as:

$$\mathbf{S^A} = \begin{bmatrix} \mathbf{S_{11}^A} & \mathbf{S_{12}^A} \\ \mathbf{S_{21}^A} & \mathbf{S_{22}^A} \end{bmatrix} \qquad \mathbf{S^B} = \begin{bmatrix} \mathbf{S_{11}^B} & \mathbf{S_{12}^B} \\ \mathbf{S_{21}^B} & \mathbf{S_{22}^B} \end{bmatrix}$$

Reflected field coefficients are related to the incident field coefficients as follows:

$$\begin{aligned} \boldsymbol{b_1} &= \mathbf{S_{11}^A}\boldsymbol{a_1} + \mathbf{S_{12}^A}\boldsymbol{a_2} \\ \boldsymbol{b_2} &= \mathbf{S_{21}^A}\boldsymbol{a_1} + \mathbf{S_{22}^A}\boldsymbol{a_2} \\ \boldsymbol{b_3} &= \mathbf{S_{11}^B}\boldsymbol{a_3} + \mathbf{S_{12}^B}\boldsymbol{a_4} \\ \boldsymbol{b_4} &= \mathbf{S_{21}^B}\boldsymbol{a_3} + \mathbf{S_{22}^B}\boldsymbol{a_4} \end{aligned} \tag{2.22}$$

In the region between the two discontinuities, transmitted and reflected fields are continuous which allows us to write the following equalities:

$$\boldsymbol{a_2 = b_3} \text{ and } \boldsymbol{a_3 = b_2}$$

At the plane of short circuit at the end of the structure:

$$\boldsymbol{a_4 = -b_4}$$

By substituting and rearranging (2.22), we have:

$$\begin{aligned} \boldsymbol{a_2} &= \left(\mathbf{U} - \mathbf{S_{11}^B S_{22}^A}\right)^{-1}\left(\mathbf{S_{11}^B S_{21}^A}\boldsymbol{a_1} + \mathbf{S_{12}^B}\boldsymbol{a_4}\right) \\ \boldsymbol{a_3} &= \left(\mathbf{U} - \mathbf{S_{22}^A S_{11}^B}\right)^{-1}\left(\mathbf{S_{21}^A}\boldsymbol{a_1} + \mathbf{S_{22}^A S_{12}^B}\boldsymbol{a_4}\right) \end{aligned} \tag{2.23}$$

where **U** is the identity matrix. Transmission lines are introduced in between the discontinuities to account for the proper phase shift. The first transmission line between the two discontinuities is described by the diagonal matrix:

$$\mathbf{T_1} = \begin{bmatrix} \mathrm{e}^{-\gamma_{nm}^{i} L_1} & \cdots & 0 \\ \vdots & \ddots & \vdots \\ 0 & \cdots & \mathrm{e}^{-\gamma_{nm}^{J} L_1} \end{bmatrix} \tag{2.24}$$

where γ_{nm}^{i} is the propagation constant corresponding to the i^{th} mode and L_1 is the distance between the two discontinuities as presented in Fig.2.2(b). Similarly, the transmission line between the second discontinuity and the short circuit is described by the following diagonal matrix.

$$\mathbf{T_2} = \begin{bmatrix} \mathrm{e}^{-2\gamma_{nm}^{j} L_2} & \cdots & 0 \\ \vdots & \ddots & \vdots \\ 0 & \cdots & \mathrm{e}^{-2\gamma_{nm}^{J} L_2} \end{bmatrix} \tag{2.25}$$

where L_2 is the length between the short circuit and discontinuity plane between coaxial 2 and circular waveguide.

The sub-matrices of the resultant cascaded matrices are:

$$\begin{aligned} \mathbf{S_{11}^C} &= \mathbf{S_{11}^A} + \mathbf{S_{12}^A T_1}\left(\mathbf{U} - \mathbf{S_{11}^B T_1 S_{22}^A T_1}\right)^{-1}\mathbf{S_{11}^B T_1 S_{21}^A} \\ \mathbf{S_{12}^C} &= \mathbf{S_{12}^A T_1}\left(\mathbf{U} - \mathbf{S_{11}^B T_1 S_{22}^A T_1}\right)^{-1}\mathbf{S_{12}^B} \end{aligned} \tag{2.26}$$

$$\mathbf{S_{21}^{C}} = \mathbf{S_{21}^{B}}\left(\mathbf{U} - \mathbf{T_1}\mathbf{S_{22}^{A}}\mathbf{T_1}\mathbf{S_{11}^{B}}\right)^{-1}\mathbf{T_1}\mathbf{S_{21}^{A}}$$

$$\mathbf{S_{22}^{C}} = \mathbf{S_{22}^{B}} + \mathbf{S_{21}^{B}}\left(\mathbf{U} - \mathbf{T_1}\mathbf{S_{22}^{A}}\mathbf{T_1}\mathbf{S_{11}^{B}}\right)^{-1}\mathbf{T_1}\mathbf{S_{22}^{A}}\mathbf{T_1}\mathbf{S_{12}^{B}}$$

The reflection coefficient of the entire shorted structure is given as:

$$\mathbf{S_{11}^{short}} = \mathbf{S_{11}^{C}} - \mathbf{S_{12}^{C}}\mathbf{T_2}\left(\mathbf{U} - \mathbf{T_2}\mathbf{S_{22}^{C}}\right)^{-1}\mathbf{S_{21}^{C}} \tag{2.27}$$

where $\mathbf{S_{11}^{short}}$ is the general reflection coefficient of the structure. The advantage of the matrix form is that each mode contributions can be easily extracted. It should be noted that the reflection coefficient measured with the network analyzer correspond to the TEM fundamental modes coaxial transmission line. The general S-parameters obtained from the full-wave mode matching technique model can then be directly compared to the one measured with the network analyzer. So, by implementing an iterative method of optimization [51] it is possible to solve the inverse problem which is to extract the unknown complex permittivity of the material under test. The following section explains how the iterative method is performed.

6. Optimized First Order Gradient Method

An optimized first order gradient method is implemented to solve the inverse problem, i.e finding the complex permittivity components measuring the scattering parameters obtained from the performance analyzer. The S-parameters simulated using the mode matching method are compared to measured reflection coefficient. If the convergence criteria are not respected another complex permittivity ($\varepsilon_r = \varepsilon_r' - j\varepsilon_r''$) is computed. The code is implemented in Matlab [52] and complex numbers are converted in vector form where an initial value is determined:

$$\hat{a}_0 = \begin{bmatrix} \varepsilon' \\ \varepsilon'' \end{bmatrix} \tag{2.28}$$

Associated to this vector, an error vector is evaluated by comparing the reflection the simulated and measured reflection coefficient S_{11}.

$$\Delta\vec{S} = \begin{bmatrix} S_{11x}^{(m)} - S_{11x}^{(c)} \\ S_{11y}^{(m)} - S_{11y}^{(c)} \end{bmatrix} \tag{2.29}$$

where *m* and *c* denote the measured and calculated S-parameters in rectangular coordinates. A first order derivative matrix is then derived to evaluate the direction of the minima as:

$$\Delta\vec{S} = \begin{bmatrix} \frac{\partial S_{11x}}{\partial \varepsilon'} & \frac{\partial S_{11x}}{\partial \varepsilon''} \\ \frac{\partial S_{11y}}{\partial \varepsilon'} & \frac{\partial S_{11y}}{\partial \varepsilon''} \end{bmatrix} \begin{bmatrix} \Delta\varepsilon' \\ \Delta\varepsilon'' \end{bmatrix} \tag{2.30}$$

So, by inversing the derivative matrix a new permittivity vector is evaluated where the new search direction is given by:

$$\hat{a}_n = \hat{a}_{n-1} + \begin{bmatrix} \propto_1 \Delta\varepsilon' \\ \propto_2 \Delta\varepsilon'' \end{bmatrix} \tag{2.31}$$

where $\propto$ parameters defined the distance between the actual and next value of the permittivity, $\hat{a}_n$ is the new value which becomes the initial value for next iteration.The convergence criteria are respected when $\|\Delta\vec{S}\|^2 < 10^{-8}$ or $\propto < 10^{-6}$.

7. Numerical Results

This section is dedicated to the determination of the number of modes contributing significantly to describe the coaxial discontinuities. Thus, a convergence study is carried out to truncate the number of modes in each region. This process is important to reduce computing time while achieving accurate model. Hence, the same simulation is realized several times and the number of modes in each section is increased until the scattering parameters converge to one solution.

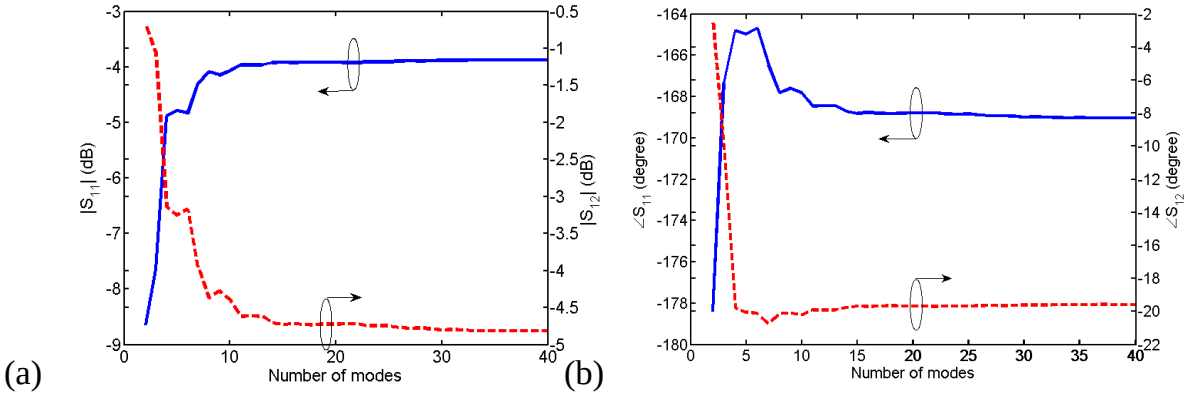

Fig. 2.5: Convergence of the reflection and transmission scattering parameters of a coaxial-coaxial discontinuity versus the number of modes in each side at 40 GHz. (a) Magnitude S_{11} and S_{12} in dB, (b) Phase S_{11} and S_{12} in degree. Dimensions of design parameters as shown in Fig. 2.2(a) are: $r_1^{(1)}$= 1.2 mm, $r_2^{(1)}$ = 0.52 mm, $r_1^{(2)}$= 1.26 mm, $r_2^{(2)}$= 0.254 mm, ε_r = 17 –j1.7.

The algorithms developed in the previous section are carried in an in-house program developed in Matlab [52]. Fig. 2.5 presents the convergence study of the scattering parameters of the transition from coaxial 1 to coaxial 2 as given in Fig. 2.2 assuming that region 2 is filled with fictive material with a permittivity ε_r = 17 –j1.7. In this study the same number of modes in each coaxial region is considered including fundamental TEM and TM_{0m} higher-order modes at a fixed frequency of 40 GHz. In Fig. 2.5 it is shown that 15 modes are sufficient to accurately describe the coaxial-coaxial discontinuity presented in Fig.2.2 (a) as no change occurs in the scattering parameter (magnitude or phase) after increasing the number of modes. The accuracy of the coaxial-coaxial model using the mode matching technique is then compared with a commercial software HFSS [47] using the finite element method as shown in Fig. 2.6 where the scattering parameters both magnitude and phase are presented function of the frequency.

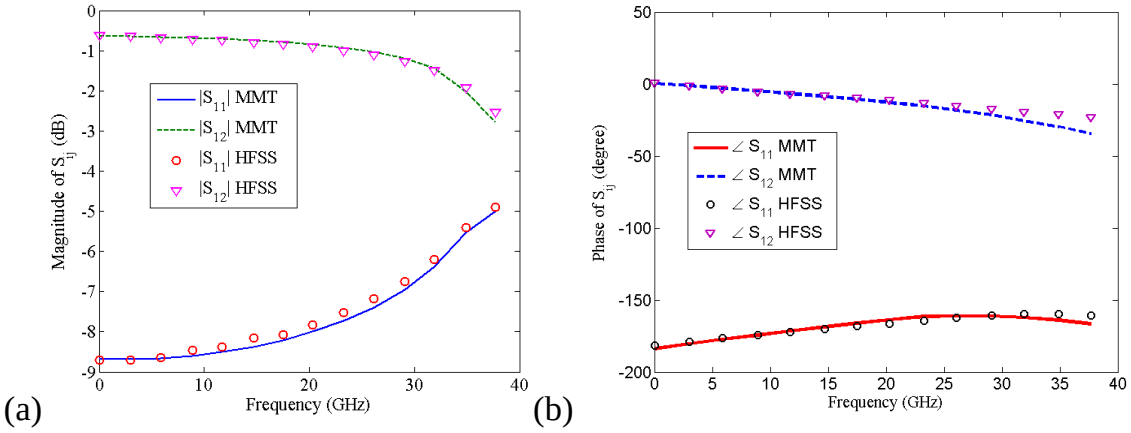

Fig. 2.6: Scattering parameters of the coaxial to coaxial discontinuity, (a) Magnitude S_{ij} in dB, (b) Phase S_{ij} in degree. Dimensions of design parameters shown in Fig. 2.(a) are: $r_1^{(1)}$= 1.2 mm, $r_2^{(1)}r_2^{(1)}$ = 0.52 mm, $r_1^{(2)}$= 1.26 mm, $r_2^{(2)}$= 0.254 mm, ε_r = 17 –j1.7.

Similarly, the second transition between region 2 coaxial and 3 circular waveguide filled with a fictive material of complex permittivity ε_r = 17 –j1.7 is performed through the convergence study at 40 GHz shown in Fig. 2.7. The outer radius of the coaxial waveguide is assumed the same as the circular waveguide as shown in Fig. 2.2 (a). In Fig. 2.7, 15 modes seem sufficient to accurately describe the coaxial-circular discontinuity. It should be noted that the choice of the number of modes to describe each discontinuity is a tradeoff between saving computing time and accurate modeling. For characterization purposes, an iterative method is implemented to solve the inverse problem which is to extract the material properties based on the measured reflection coefficient. In other words, each time a new value of the complex permittivity is determine a new set of scattering parameters is computed. Then, the coaxial-circular waveguide transition model is then compared with HFSS [47] simulation function of frequency to verify the accuracy of the model as shown in Fig. 2.8.

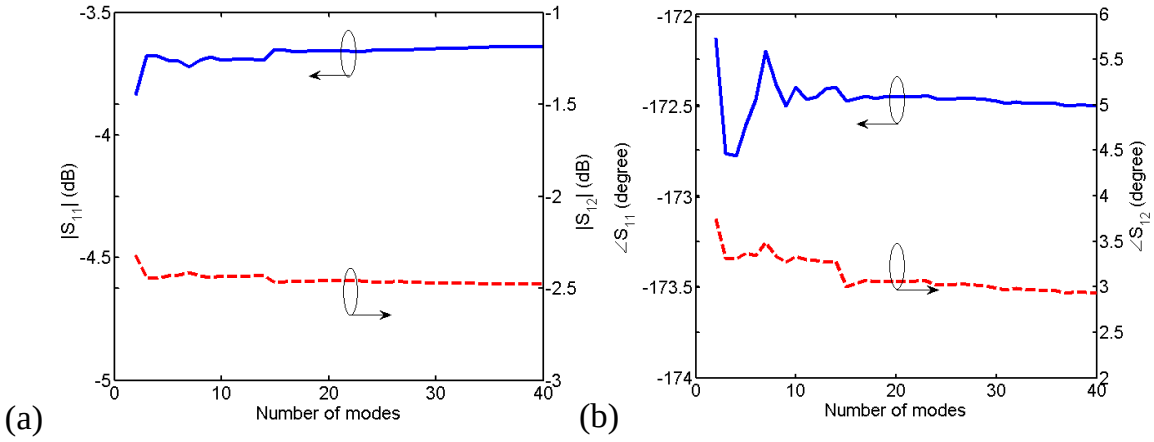

Fig. 2.7: Convergence of the reflection and transmission scattering parameters of a coaxial-circular discontinuity versus the number of modes in each side: (a) Magnitude of S_{11} and S_{12} in dB, (b) Phase of S_{11} and S_{12} in degree. Dimensions of design parameters shown in Fig, 2.2(a) are: $r_1^{(2)}$= 1.26 mm, $r_2^{(2)}$= 0.254 mm, ε_r = 17 –j1.7.

The complete structure presented in Fig. 2.2 (a) is then compared with the model presented in Fig. 2.8 realized with HFSS commercial software [47]. The structure simulated with the finite element methods is optimized using the symmetry planes to save computing time as shown in Fig. 2.8.

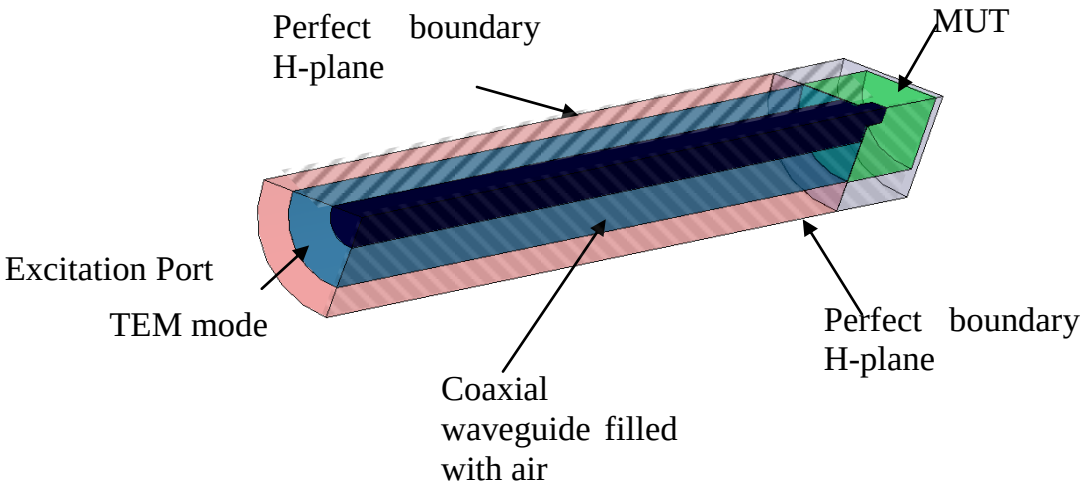

Fig. 2.8: HFSS model for the test structure shown in Fig. 2.2 (a).

So, due to the circular configuration it is possible to simulate only ¼ of the structure to increase the number of iterations to compute the convergence criteria and improve the accuracy of the simulation without enhancing the computing time. Fig. 2.9 shows the comparison of the complex reflection coefficient (magnitude and phase) obtained from HFSS and the mode matching technique models, both simulations are carried out on the same 64-bit operating system windows 7 enterprise PC with Intel® Core™2 Quad CPU Q9550 @2.84 GHz and 4 GB RAM memory.

The structure is filled with the same fictive MUT with a complex relative permittivity of $\varepsilon_r = 17 - j1.7$. HFSS simulation details include a convergence criteria delta S of 0.001, the structure is excited using one TEM port sufficiently far from the discontinuities to avoid misinterpretation of the results due to evanescent modes excited by the waveguides transitions. The model consists of 37201 mesh elements and the HFSS ComEngine memory is 66.7M. The simulation of the structure shown in Fig. 2.8 takes approximately 12 minutes considering a step frequency of 100 MHz from 10 MHz to 40 GHz. The MMT simulation is realized considering 15 modes in each region as describes in Fig. 2.2(a) and from the predicted convergence study presented in Fig. 2.5 and Fig. 2.7. Only 2 minutes are necessary to solve the same problem using the same computer highlighting the efficiency of the mode matching technique over the finite element methods to model such waveguide structure.

To fully validated the extraction technique, the reflection coefficient obtained from HFSS model filled with a complex fictive relative permittivity $\varepsilon_r = 17 - j1.7$ is used to iteratively vary the complex permittivity implemented in the mode matching technique following the flow chart presented in Fig. 2.10. It should be noted that in this case the simulated reflection coefficient obtained with HFSS replaced the measured reflection coefficient with the network analyzer.

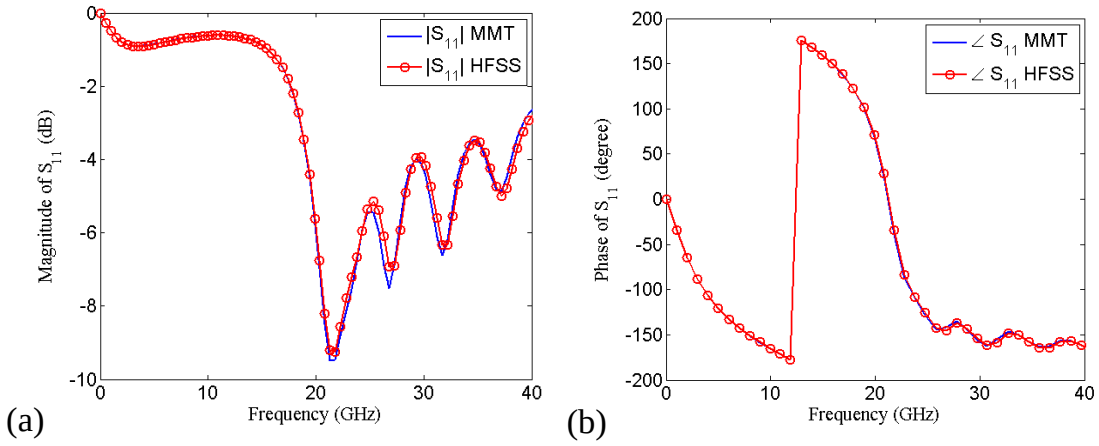

Fig. 2.9: Comparison of the reflection coefficient simulated with the mode matching technique and HFSS of the testing structure shown in Fig. 2.2(a) and Fig. 2.8. (a) Magnitude of S_{11} in dB, (b) Phase of S_{11} in degree. Dimensions of design parameters shown in Fig. 1(a) are: $r_1^{(1)}$= 1.2 mm, $r_2^{(1)}$ = 0.52 mm, $r_1^{(2)}$= 1.26 mm, $r_2^{(2)}$= 0.254 mm, ε_r = 17 –j1.7, L_1 = 1.1 mm, L_2 = 5 mm.

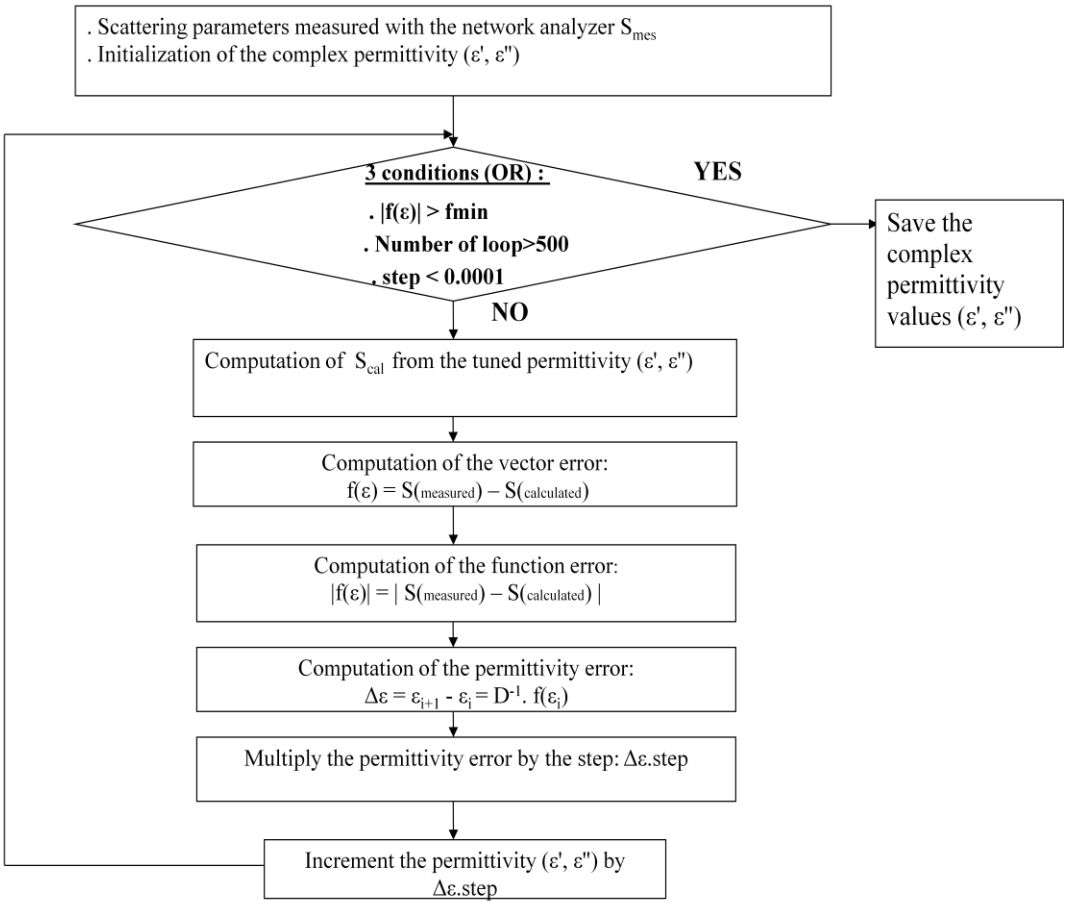

Fig. 2.10: Flow chart of the code implemented in Matlab to extract the electrical properties of the MUT

The complex relative permittivity extracted from the HFSS simulated reflection coefficient are in very good agreement and a standard deviation less than 2% on the real and imaginary part of the fictive material is observed in Fig. 2.11.

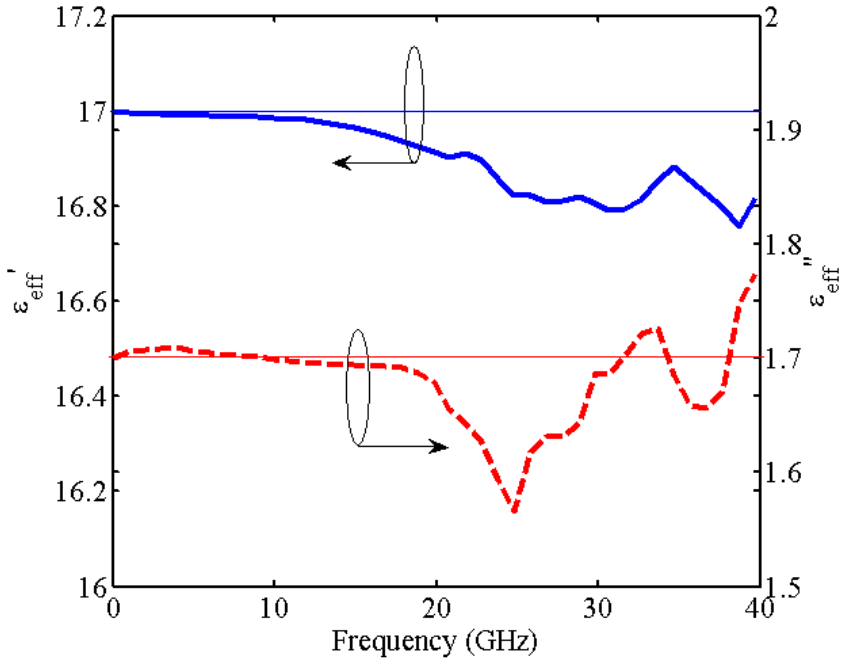

Fig. 2.11: Relative complex permittivity extracted using MMT based on numerical results obtained from HFSS for a fictive material ($\varepsilon_r = 17 - j1.7$). The corresponding reflection coefficients are shown in Fig. 2.9.

8. Experimental Results

Based on the complex reflection coefficient measured with PNA, the couple, real and imaginary part of the complex permittivity is adjusted until the simulated reflection coefficient using the mode matching technique matched the measured S_{11} from the network analyzer. The first set of experiments consists to evaluate the extraction technique with known electrical properties of lossless and lossy material under test.

Thus, the fabricated test cell as shown in Fig. 2.1 is filled with air with a known complex permittivity of $\varepsilon_r = 1 - j0$.

Fig. 2.12 presents the comparison of the measured and simulated with MMT reflection coefficient. Then Fig. 2.13 shows the extracted complex permittivtiy in case of air $\varepsilon_r = 1 - j0$. In case of lossless material it should be noted that the accuracy of the technique is related to the precision of the calibration process of the performance network analyzer. In fact the imaginary part of the permittivity is related to the loss, so in case of the lossless material the magnitude of the reflection coefficient is close to 0 dB and only the phase measurement provides sufficient information to extract the complex permittivity as shown in Fig. 2.12. So, to enhance the calibration of the instrumentation over a broad frequency band two sets of Short-Open-Load-Thru (SOLT) calibration are carried out from 10 MHz to 20 GHz and from 20 GHz to 40 GHz with 201 frequency point in each band. In addition, the intermediate frequency band is fixed to 70 Hz to minimize error due to random noise and the reference plane is directly in contact with the material under test to avoid phase ambiguity.

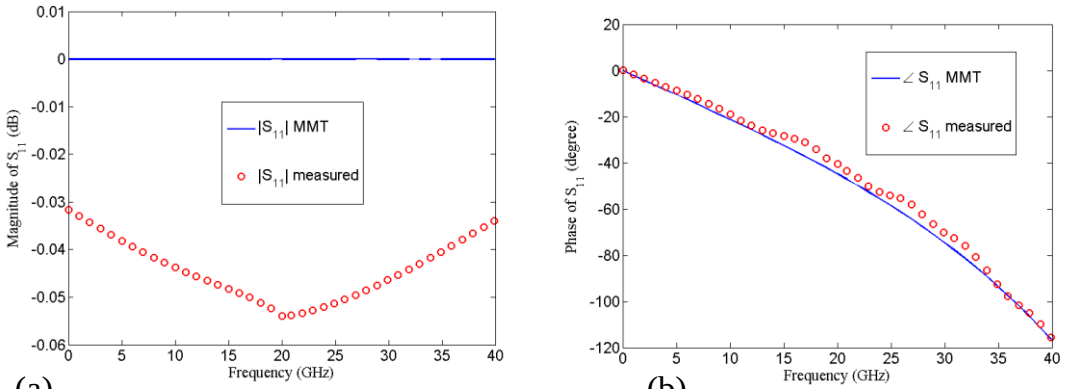

(a) (b)

Fig. 2.12: Comparison of the reflection coefficient obtained from MMT and microwave measurements of the testing structure shown in Fig. 1(a) when the cell is air filled ($\varepsilon_r = 1 - j0$). (a) Magnitude S_{11} in dB, (b) Phase S_{11} in degree. Dimensions of design parameters as shown in Fig. 2.2(a) $r_1^{(1)} = 1.2$ mm, $r_2^{(1)} = 0.52$ mm, $r_1^{(2)} = 1.26$ mm, $r_2^{(2)} = 0.254$ mm, $\varepsilon_r = 17 - j1.7$, $L_1 = 1.1$ mm, $L_2 = 5$ mm.

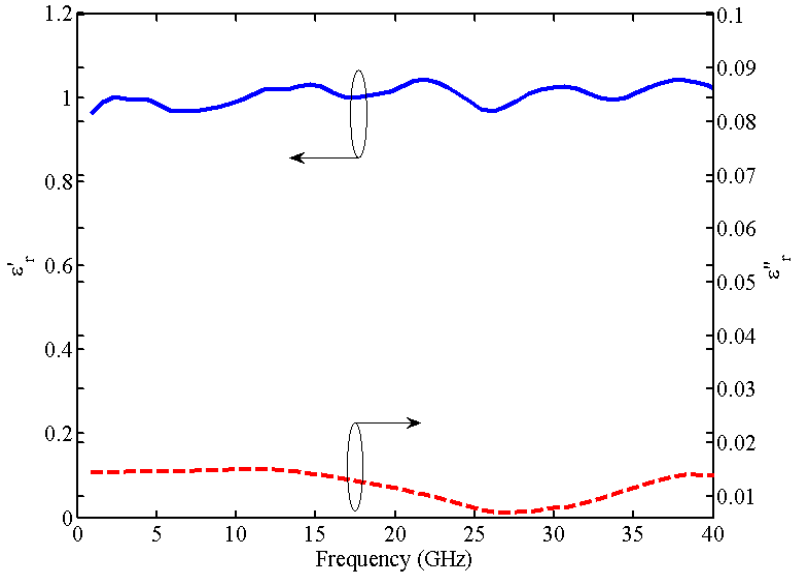

Fig. 2.13: Extraction of the relative complex permittivity of air when the cell is empty (ε_r =1 –j0) computed from the measured reflection coefficient presented Fig. 2.12.

The relative error found in the extracted complex permittivity of air as shown in Fig. 2.13 is mainly due to the approximation of the model where the surface of the fabricated circular waveguide are assumed perfectly conductor and smooth which is not true in practice. Those assumptions can be seen in Fig. 2.12(b) where fluctuations occur in the phase measurements due to the tolerance of the manufactured structure. The second verification of the extraction technique include a lossy medium such as deionized (DI) water at room temperature and compared with published results found in the literature [53] and presented in Fig. 2.14. The comparison of the scattering parameters between the measurement and the following frequency dependence Debye function have been published in [37].

$$\varepsilon(\upsilon) = \varepsilon(\infty) + \frac{\varepsilon(0) - \varepsilon(\infty)}{1 + j\omega\tau}$$

where the parameters given in [53] for the Debye relaxation spectral function for water at 25^{o}C. Static dielectric constant $\varepsilon(0) = 78.36 \pm 0.05$, permittivity at high frequency$\varepsilon(\infty) = 5.2 \pm 0.1$ relaxation time$= 8.27 \pm 0.02$ps , ω is the angular frequency.

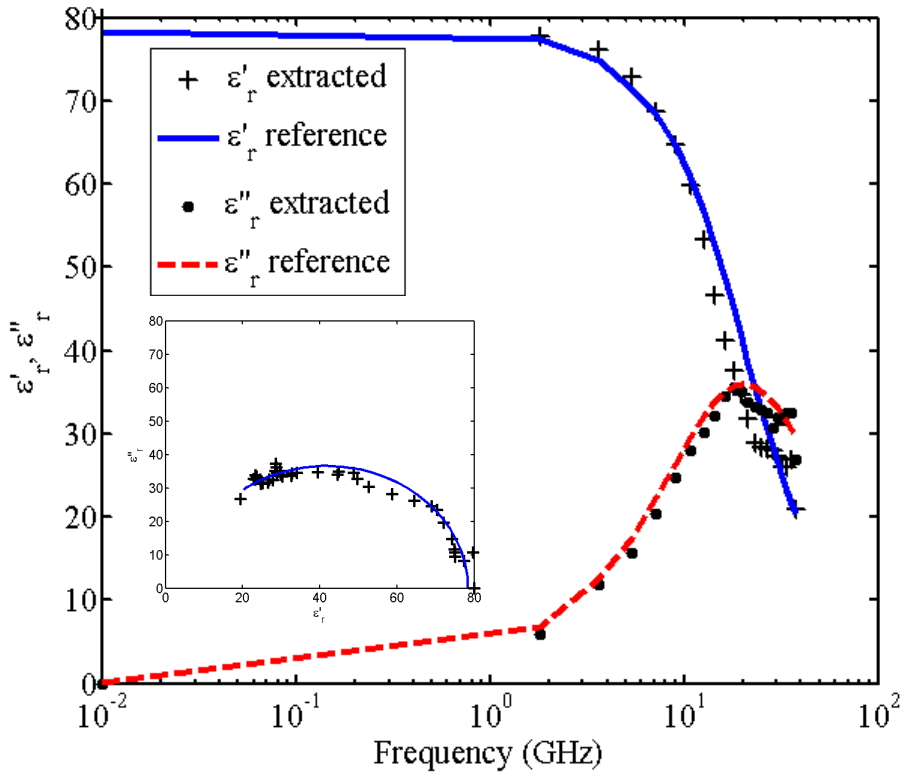

Fig. 2.14: Relative complex permittivity of water extracted by applying the described process in this paper and compared with data found in reference [53] for distilled water at 25°C. The inset presents the Argand diagram of the reference permittivity compared with the extracted measurements (black cross line).

III. RIGOROUS CHARACTERIZATION OF CARBON NANOTUBE COMPLEX PERMITTIVITY OVER A BROADBAND OF RF FREQUENCIES[2]

A. INTRODUCTION

After verifying the validity of our extraction technique the complex permittivity of carbon nanotubes in a dry powder form is then evaluated by inserting the CNT powder in the measurement setup presented in chapter 2. The CNT rigorous characterization over a broad frequency band includes the effect of the packing density and physical explanations of the measured experimental data. The main difference between our proposed technique and published extraction process is that usually others techniques requires to prepare the carbon nanotubes sample in a thin film or embedded in dielectric host medium which affects the measurements explaining the large values difference found in the literature. In our case the dry powder as furnished by the supplier stand alone the hollow circular waveguide as described in chapter 2. In addition, by confining the powder in a known volume it is possible to study the material properties function of the packing density [54]. Several advantages of the implemented extraction methods are highlighted in this work compared to published process in the literature: the material under test can be in pulverized, solid or liquid form; only a small fraction of material

---

[2] ©2012 IEEE. Reprinted, with permission, from E. Decrossas, M.A. EL Sabbagh, V. Fouad Hanna and S.M. El-Ghazaly, "Rigorous characterization of carbon nanotube complex permittivity over a broadband of RF frequencies," in *IEEE Transactions on Electromagnetic Compatibility*, vol. 54, no. 1, pp. 81-87, February 2012.
E. Decrossas, M.A. EL Sabbagh, V. Fouad Hanna and S.M. El-Ghazaly, "Engineered Carbon-nanotube Based Composite Materials for RF Applications," *in IEEE Transactions on Electromagnetic Compatibility*,vol. 54, no. 1, pp. 52-59, February 2012.
E. Decrossas, M.A. EL Sabbagh, V. Fouad Hanna and S.M. El-Ghazaly, "Measurement-based Effective Conductivity of Carbon Nanotube Networks for Microwave Design Purposes," in IEEE International Microwave Symposium, Montreal, Canada, June 17-22, 2012.
E.Decrossas, and S.M. El-Ghazaly. "Microwave characterization of carbon nanotube networks" in Carbon Nanotubes/book 6. S. Bianco, Intech, 2011.

is required and this is a none destructive methods which significantly reduces the cost of the characterization in case of carbon nanotube networks; the process is easily implemented and only a single test structure is used to extract the complex permittivity over a wide frequency band from 10 MHz to 50 GHz [37] and [54].

Based on experiments, the large values of the complex permittivity are physically explained using the percolation theory through the experimental study of the permittivity functions of the packing density and the frequency. In addition, a model describing the effective conductivity is built based on the experimental study to improve the CNT-based simulations.

B. COMPLEX EFFECTIVE PERMITTIVITY OF CARBON NANOTUBE NETWORKS

To reduce errors due to the measurements the performance network analyzer (PNA, Agilent E8163) three short-open-load coaxial calibrations are performed through the entire frequency band: from 10 MHz to 1 GHz, from 1 GHz to 20 GHz, and from 20 GHz to 50 GHz. 201 frequency points and 70 Hz intermediate frequency (IF) bandwidth are considered in each frequency range to reduce noise and minimize calibration errors.

In this part of study, bundled networks of single-walled CNTs are used as provided by manufacturer (Sigma-Aldrich): the sample purity is 50 to 70 volume percentage as determined by Raman spectroscopy and scanning electron microscopy (SEM) which shows that the sample contains residual catalyst impurities of nickel and yttrium. The length of an individual CNT is approximately 20 μm. Several images are taken by SEM and they reveal the presence of multi-walled CNTs as well as single-walled CNTs within the sample which is in agreement with similar data reported in [55].

The variation of the real and imaginary part of the relative extracted permittivity ($\varepsilon_r = \varepsilon_r' - j\varepsilon_r''$) of carbon nanotube network function of the frequency considering several packing density is presented through Fig. 3.1 to Fig. 3.4.

The packing density is computed using the relation:

$$\rho = \frac{M}{V}\ (\mathrm{g/cm^3})$$

where M is the mass of the CNT powder inserted in the measurement setup in grams weighed using a analytical balance with 0.001mg resolution and V is the volume of cavity in $\mathrm{cm^3}$ determined through optical measurements.

The results obtained for the complex permittivity of carbon nanotubes dry powder are presented using two different frequency bands for a better clarity as large variation at low frequencies are observed in Figs. 3.1 and 3.3 while at high frequencies the permittivity seems to converge to an asymptotic values as shown in Figs. 3.2 and 3.4.

As shown in Figs. 3.1 and 3.2, the real part of the permittivity or dielectric constant decreases with the frequencies from a maximum value 1.6×10^5 obtained at 10 MHz to reach 6.5 at 50 GHz. Similarly, the highest value of the imaginary part of the relative complex permittivity at 10 MHz is 4.1×10^3 as shown in Fig. 3.3 and decreases to 7 at 50 GHz as shown in Fig. 3.4. The extracted complex permittivity data plotted through Fig. 3.1 to 3.4 are in agreement with those reported in [36] and [55]-[56].

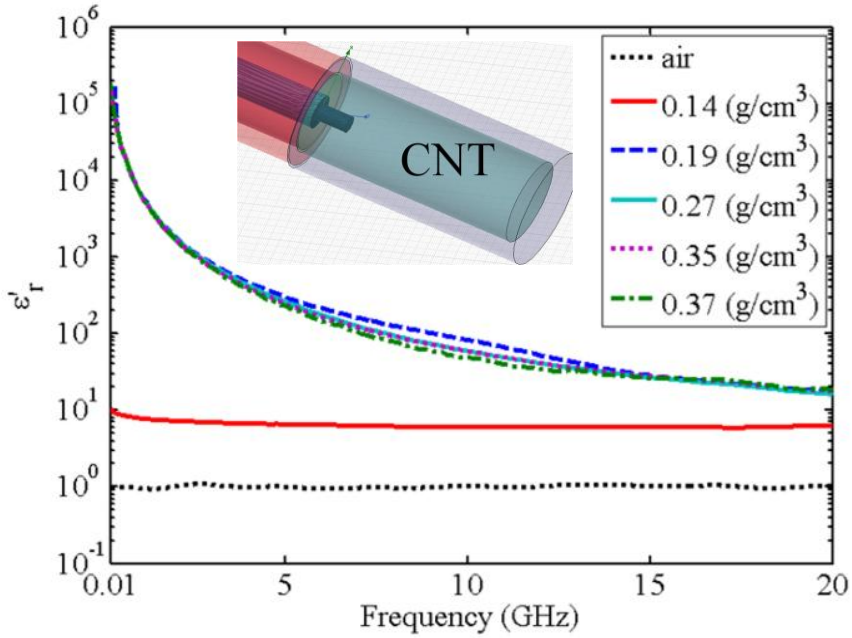

Fig. 3.1: Variation of the real part of the relative complex permittivity of CNT networks in the frequency range 10 MHz to 20 GHz for different packing densities. The y-axis is in logarithmic scale to show the dramatic variation of the real part of the permittivity. Permittivity of air is included for reference.

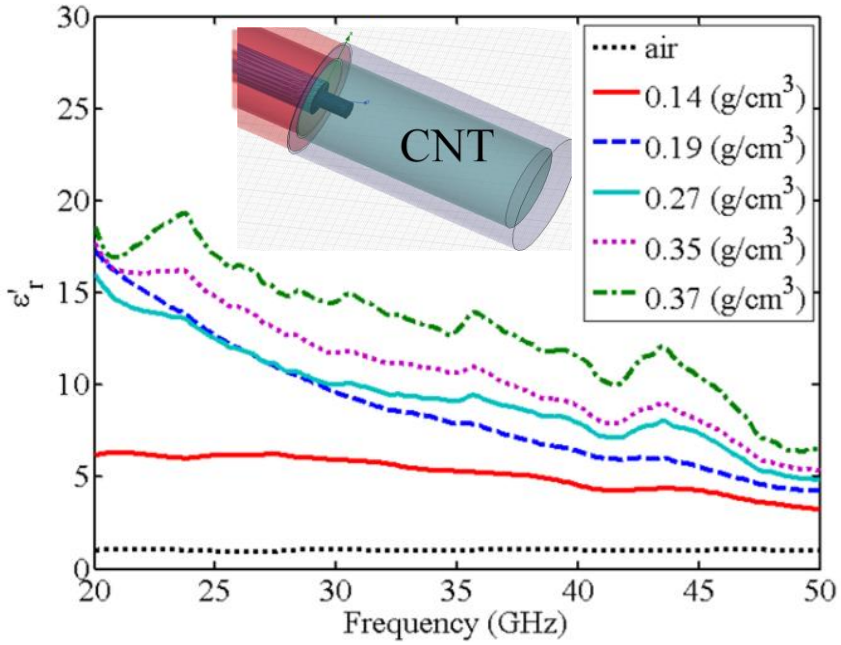

Fig. 3.2: Variation of the real part of the permittivity of CNT networks in the frequency range 20 GHz to 50 GHz for different packing densities. The linear vertical scale indicates a small variation of the real of the permittivity, suggesting asymptotic values. Permittivity of air is included for reference.

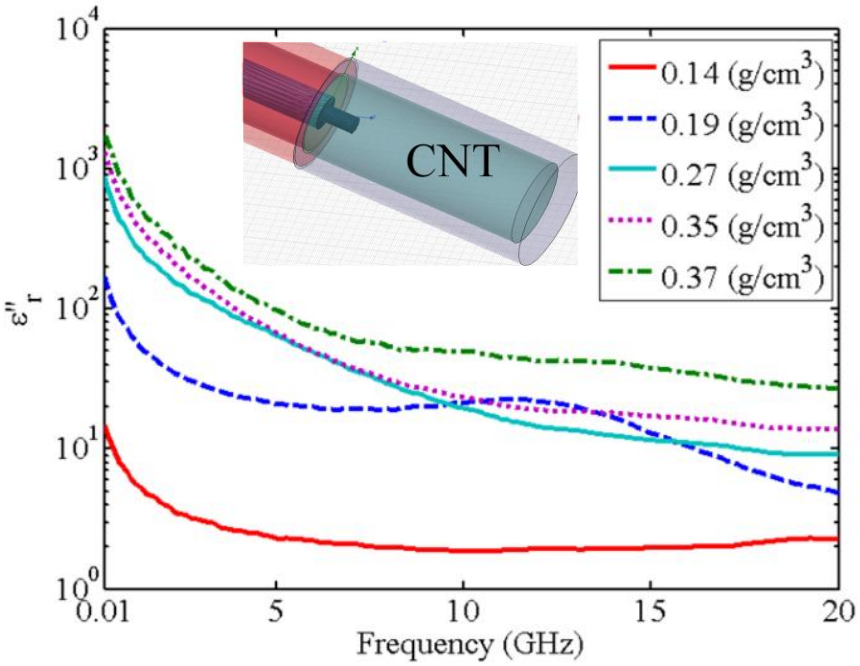

Fig. 3.3: Variation of the imaginary part of the relative permittivity of CNT networks in the frequency range 10 MHz to 20 GHz for different packing densities. The y-axis is in logarithmic scale to show the dramatic variation of the imaginary part of the permittivity. The imaginary part of the permittivity for air is not plotted in log scale because it is less than 10^{-3} which is outside the range of interest.

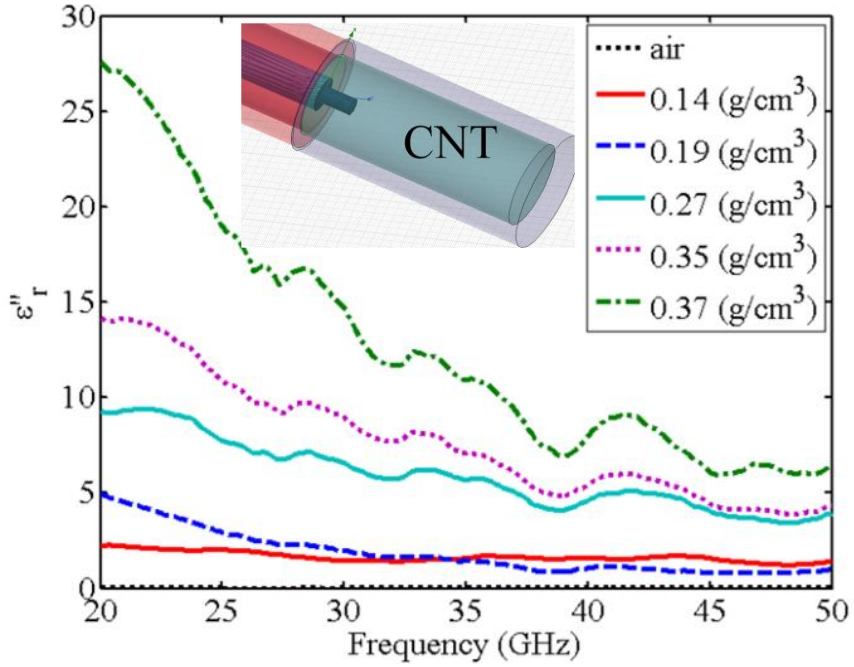

Fig. 3.4: Variation of the imaginary part of the permittivity of CNT networks in the frequency range 20 GHz to 50 GHz for different packing densities. The linear scale indicates a small variation of the imaginary part of the permittivity, suggesting asymptotic values.

In addition the variation of the complex permittivity increases with the packing density as plotted in Figs. 3.5 and 3.6. The high values of the imaginary part of the permittivity can be attributed to the conductivity of the carbon nanotube networks as presented in [36] ($\varepsilon_r'' = \frac{\sigma}{\omega}$ where σ is the conductivity of the MUT and ω is the angular frequency). The trend followed by the plots presented in Figs. 3.5 and 3.6 are consistent with the percolation behavior of the material composed of semi-conducting and metallic elements [28]. In other words, the material behaves as dielectric until a percolation threshold is reached and the material becomes conductor due to the insertion of metallic particles. As mentioned in chapter 2, CNTs consist of a mixture of conducting and semiconducting nanotubes with a ratio of 1:2 depending on their chirality, i.e., 1/3 metallic tubes are mixed with 2/3 of semiconducting nanotubes from the theoretical model described in Chapter 1.

Fluctuations as shown in Figs. 3.2 and 3.4 in the extracted values of dielectric properties especially at higher frequencies may be attributed to the random nature of CNT networks which includes randomness in number of semiconducting and metallic nanotubes, the randomness of orientation and alignment of nanotubes. To avoid this effect, statistical measurement variations are to be considered to get smooth results. Another reason is the assumption virtually considered in any modeling technique that surface roughness is neglected. This has quite a strong effect on the extracted dielectric constant as frequency goes up explaining why the fluctuations occur at the same frequencies independently of the packing density. A measurement scenario without CNTs

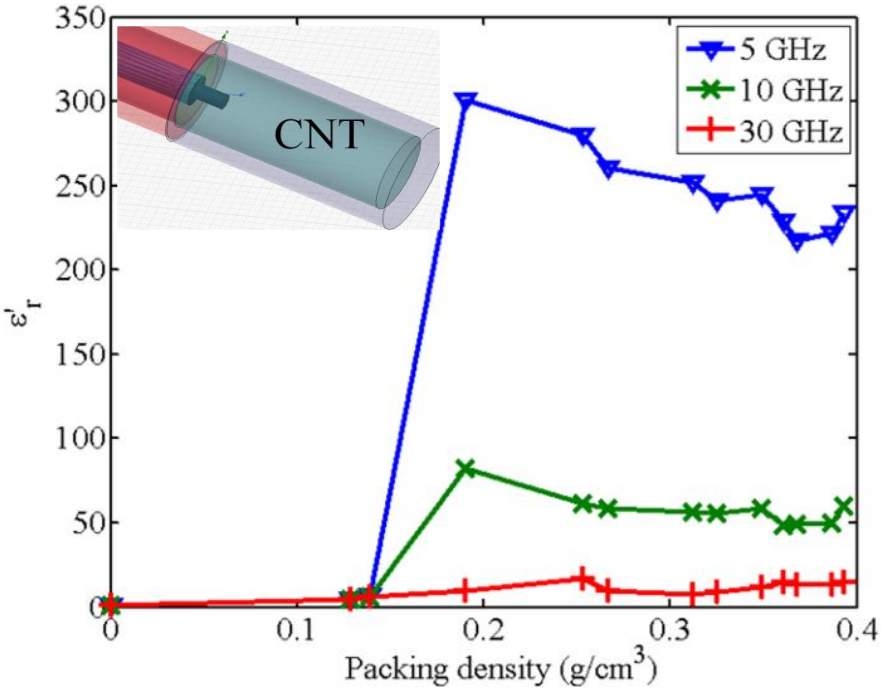

Fig. 3.5: Variation of the real part of the effective permittivity of CNT networks as a function of packing density at 5, 10 and 30 GHz.

which corresponds to air is included for reference purposes. This case was originally presented in [37] and added here to serve as a reference in Figs. 3.1, 3.2, and 3.4. We observe quite a constant value of dielectric constant as a function of frequency when the packing density of CNTs is little as it is dominated by air.

Above a packing density of 0.15 g/cm^3, we observe a percolation behavior of permittivity versus density of CNTs as shown in Fig. 3.5 due to the dramatic increase of number of nanotubes and the reduction of air interstices. The data in Fig. 3.5 and Fig. 3.6 are obtained from results shown in Figs. 3.1 to 3.4 at 5, 10 and 30 GHz as well other measurements with different packing densities. The results in Fig. 3.5 indicate a percolation behavior which is quite significant for lower frequencies, e.g., 5 GHz. After the percolation threshold, the dielectric constant decreases as the packing density increases. The same behavior also occurs at higher test frequencies such

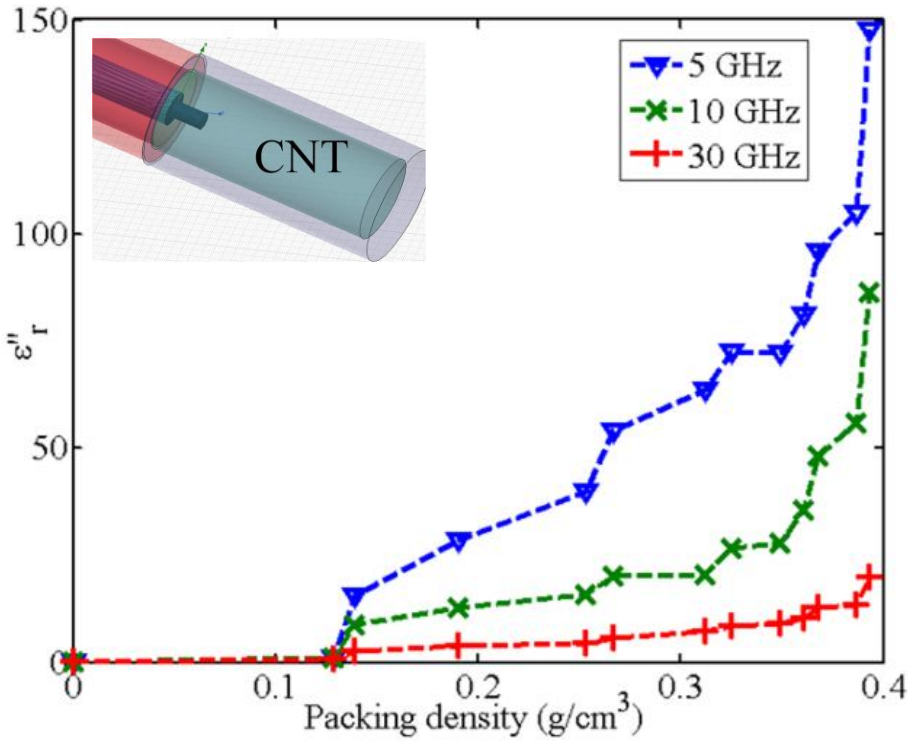

Fig. 3.6: Variation of the imaginary part of the relative permittivity of CNT networks as a function of packing density at 5, 10 and 30 GHz.

as 10 and 30 GHz yet with slower variation of dielectric constant. These results are in agreement with those in Fig. 3.2 where it is shown that in the frequency range from 5 GHz to 15 GHz, the dielectric constant corresponding to the highest packing density is lower than the dielectric constant corresponding to intermediate densities. This effect is less prominent as the frequency goes higher. It is noted that while the dielectric constant is decreasing with packing density, the imaginary part is increasing as the packing density goes beyond the percolation threshold density $\rho = 0.15$ g/cm^3 as shown in Fig. 3.6. Below this percolation threshold density, metallic CNTs are separated by semiconducting ones. As the packing density increases, the spacing between conducting CNTs becomes smaller creating nano-capacitors which significantly increases the real part of the effective permittivity until it reaches a peak value exactly at the percolation threshold density [57]. In other words, above the percolation threshold density, connected

conductive paths are completely formed in the material which leads to the dramatic increase of losses ($\varepsilon_r'' = \frac{\sigma}{\omega}$ where σ is the conductivity of the MUT and ω is the angular frequency) at a packing density of 0.4 g/cm^3. Above the percolation threshold density, the effective real part of permittivity decreases since relative dielectric constant of a metallic material is unity.

The effective complex permittivity plotted in Fig. 3.7 versus packing density. In the inset of Fig. 3.7, the real and imaginary part of the effective permittivity function of the density is plotted in log-log scale at 3 GHz to extract the relevant parameters of the percolation curves.

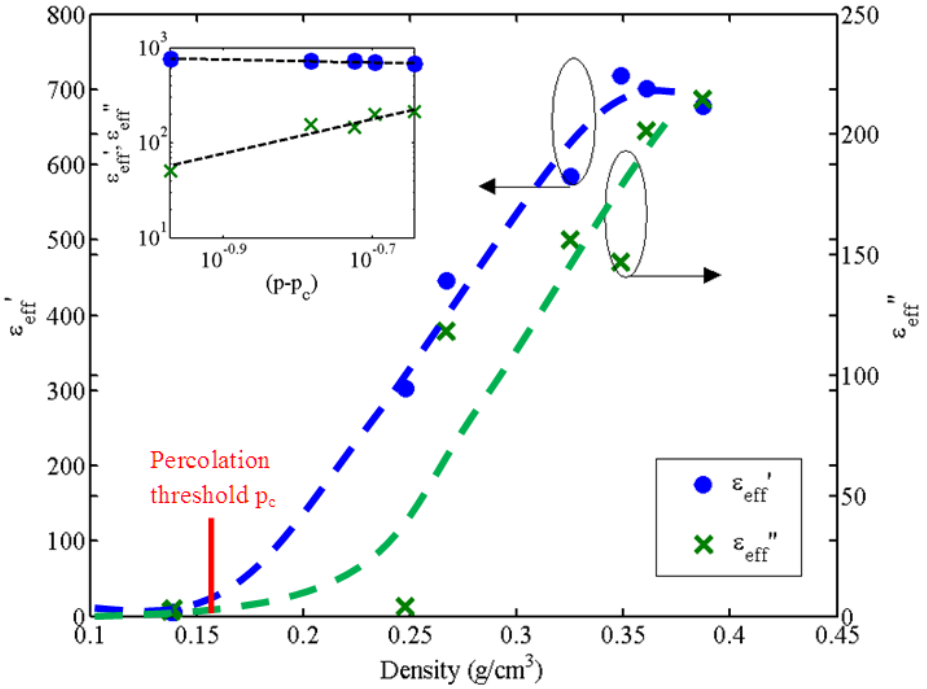

Fig. 3.7: Variation of the real (dot) and imaginary (cross) parts of the complex effective permittivity of carbon nanotube networks versus density at 3 GHz. The inset presents the log-log plots of the real and imaginary part of the complex effective permittivity functions of the occupation probability. The dashed lines in the inset are the mean values fitting curves based on equation (3.1).

Above the percolation threshold p_c , the real and imaginary parts of the effective permittivity of a conductor-insulator mixture can be expressed in terms of a power law relation as follows:

$$\varepsilon', \varepsilon'' \propto (p - p_c)^t \text{ for } p > p_c \qquad (3.1)$$

where p is the occupation probability and t is the critical exponent. It should be noted that the CNT networks include metallic, semiconducting nanotubes and air voids. Hence, the variable packing density is adopted in this work to describe the percolation behavior instead of the volume/weight fraction. The critical exponent t is usually between 1.6 and 2 in a three dimensions percolation network. However, experiments show that its value varies from 1.3 to 3.1 [59]. In Fig. 3.7, the percolation threshold p_c corresponding to the packing density of 0.15 g/cm^3 represents the onset of material changing behavior from dielectric to conductive. For the studied CNTs, the critical exponent obtained by the linear regression fitting curve of the imaginary part of the effective permittivity shown in the inset of Fig. 3.7 is 1.8 at 3 GHz which is in agreement with the percolation data reported in the literature. The region below percolation threshold where the dielectric constant increases rapidly has been studied experimentally and theoretically in [60]. Below percolation threshold, it is observed that the material behaves as an insulator with a large dielectric constant and small losses. In this work, we study the nano-material characteristics above its percolation threshold where it behaves as a conductor. Thus, a saturation followed by decreasing of the real part of the permittivity versus packing density is observed while the imaginary part continuously increases as shown in Fig. 3.7. Applying (3.1) to the fitting curve of the real part of the permittivity shown in the inset of Fig. 3.7, gives a negative critical exponent (-0.15) due to the decrease of the dielectric constant. The fact that the dielectric constant decreases above percolation threshold with the increase of packing density is because the material under test becomes more conducting due to the increasing number of metallic nanotubes. Ultimately, the real part of the permittivity should theoretically reach 1 as for a metallic material.

At low frequencies, the interaction between metallic and semiconducting nanotubes enhances the real part of complex effective permittivity. In [61], the experimental measurements applied to a mixture of nano-particles of alumina and micro-particles of copper show the contribution of packing density and the composition of a mixture of metallic-dielectric nano particles to the large values of complex permittivity.

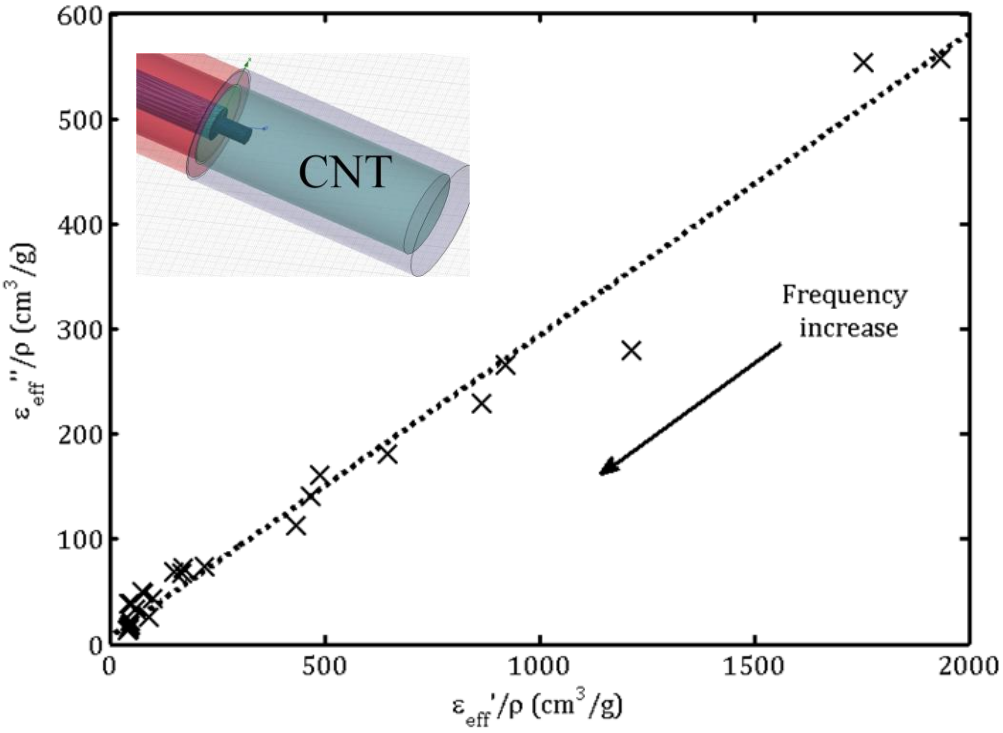

Fig. 3.8: Locus in the complex plane of the relative complex permittivity divided by bulk density for carbon nanotube networks. The black dashed line represents the linear approximation of the extracted data using the measurements setup as presented in the inset.

Moreover, studies in [62]-[63] suggest that the nonlinear-behavior of permittivity can be enhanced by changing the aspect ratio of mixed nano-particles**.** At low frequencies, the interaction between metallic and semiconducting nanotubes enhances the real part of complex effective permittivity. In [61], the experimental measurements applied to a mixture of nano-particles of alumina and micro-particles of copper show the contribution of packing density and the composition of a mixture of metallic-dielectric nano-particles to high values of complex

permittivity. Two-physical mechanisms may explain this permittivity enhancement [64]-[65]. First, electrical field creates a surface charge polarization on the interface between metallic and dielectric particles which yields an increase in capacitance. Second, dipole polarization contributes to global permittivity when the frequency of applied electrical field is lower than the relaxation frequency of metallic particles.

In Fig. 3.8, the locus in the complex plane of the relative complex permittivity divided by bulk density for carbon nanotube networks can be used to predict the behavior of the material.

C. MEASUREMENT-BASED EFFECTIVE CONDUCTIVITY OF CARBON NANOTUBE NETWORKS FOR MICROWAVE DESIGN PURPOSES

Two different setups are used to extract the conductivity of carbon nanotube networks: 1) CNTs are packed in a shorted circular waveguide connected to a performance network analyzer via coaxial cable to extract the effective complex permittivity from the reflection coefficient (S_{11}) as presented in the previous section and published in [37] and [54]. 2) CNTs replace the metallic trace in planar transmission lines and extraction is based on reflection and transmission measurements [55]. The combination of the data extracted from the CNT powder using two completely different methods is used to provide a general mathematical formula of the effective conductivity function of the packing density and frequency.

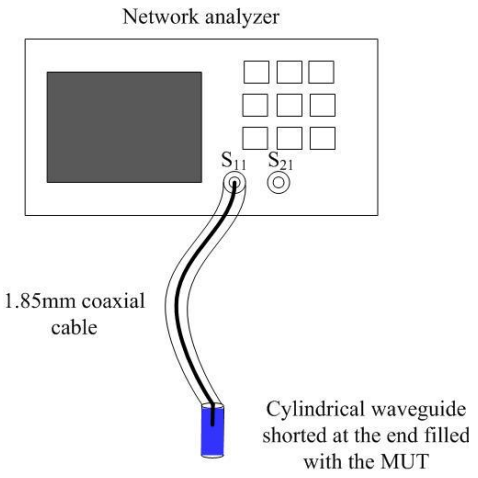

Fig. 3.9: Schematic of the measurement setup where a cylindrical waveguide filled with material under test is connected to a network analyzer via a 1.85mm coaxial cable.

The variation of the conductivity is explained based on the percolation theory. The percolation control parameters are then found by fitting the measurements curve. The usage of two independent procedures is general enough to minimize any possible fluctuations in results due to random orientation, alignment and/or the number of semiconducting versus conducting nanotubes included within the CNT networks.

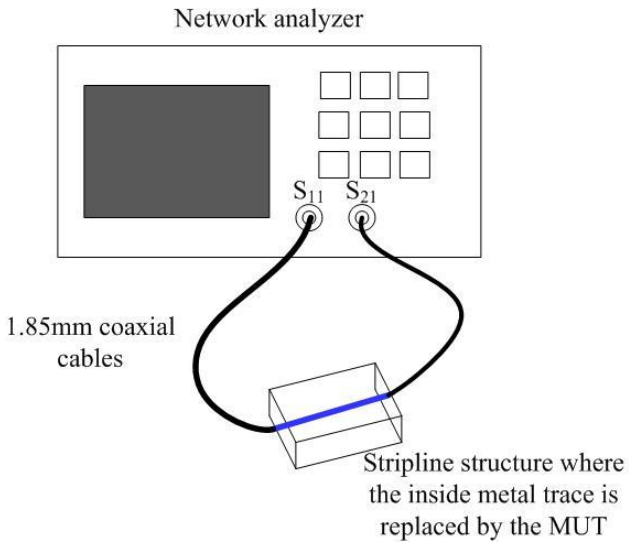

Fig. 3.10: Schematic of the transmission line measurement where the metallic trace replaced by the MUT inside a stripline structure is connected to the network analyzer via 1.85mm coaxial cables.

The probe measurement where a custom designed circular waveguide is shorted at the end and filled with the carbon nanotube networks to be tested as presented in Chapter 2. The pin of the male part protruding in the circular waveguide plays the role of the probe. Extraction of the complex effective permittivity is then carried out using the process described in [37]. The conductivity is computed from the imaginary part of the extracted complex effective permittivity $(\varepsilon = \varepsilon' - j\varepsilon'')$ as shown Figs. 3.3 and 3.4 using the following relation:

$$\sigma = \omega \varepsilon_0 \varepsilon'' \tag{3.2}$$

where ω is the angular frequency and ε_0= 8.85×10^{-12} (F/m) is the vacuum permittivity. This approach is broadband, non destructive and low cost. It allows the measurement of different packing densities where a small amount of material under test (MUT) stands alone in the circular waveguide. Measurements are realized for different packing densities up to 0.4 g/cm^3 where the powder becomes so compact that the pin cannot be easily inserted. Thus, another measurement

setup is used to extract the conductivity at higher packing density where the metallic trace of a transmission line is replaced by carbon nanotubes.

The transmission-line measurement setup consists of a stripline structure where the CNTs replace the metallic trace of the stripline structure shown in Fig. 3.10. The reflection (S_{11}) and transmission (S_{21}) coefficients are then measured to extract the complex effective permittivity of the metallic trace composed of CNT networks as described in [55].

The conductivity is then computed from the extracted complex effective permittivity using (3.2). Measurements are performed considering different packing densities but are limited to the frequency band from 10 MHz to 400 MHz where only the fundamental mode propagates in the structure.

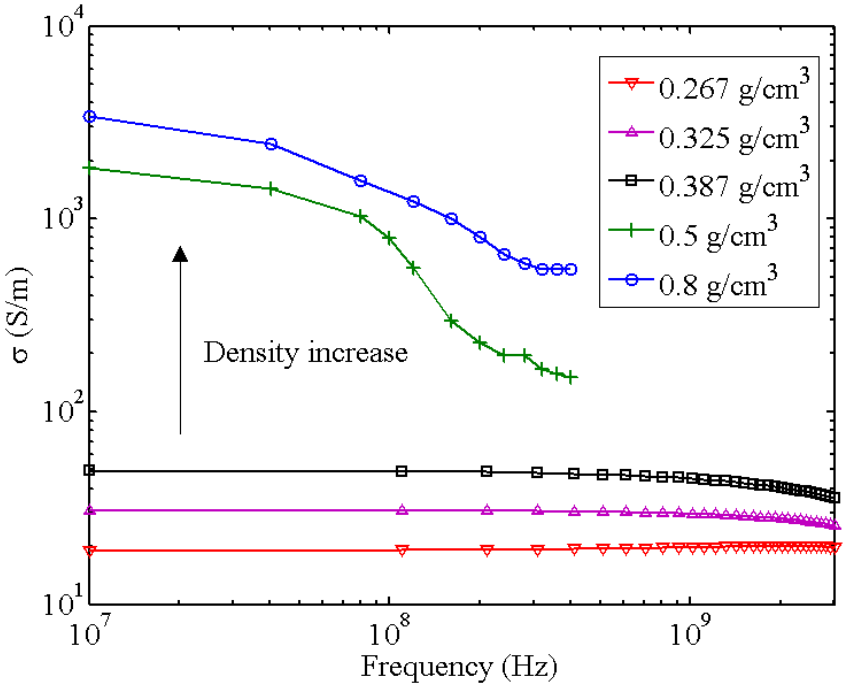

Fig. 3.11: Extracted conductivity functions of the frequency of carbon nanotubes in a dry powder form using the measurement setups presented in Fig. 3.9 and Fig. 3.10 for different packing densities. The data obtained for densities below 0.4 g/cm^3 are obtained from the coaxial discontinuity setup while above this density statistical measurements variation are extracted from the transmission line measurement setup.

This technique allows measurements of high packing density close to the theoretical value of the CNT density 1.1 g/cm^3. The conductivity function of the frequency extracted for different packing densities is presented in Fig. 3.11. It is clear that the conductivity increases with the packing density as more metallic nanotubes are introduced. In addition, the conductivity decreases with the frequency as the losses due to skin effect and carbon nanotubes semiconducting/conducting interconnects as well as air voids effects become predominant.

The conductivity of carbon nanotubes is extracted over a large range of packing densities at 100 MHz as presented in Fig. 3.12. From the experimental results, a mathematical model is built from linear regression fitting curves to predict the behavior of the conductivity of the carbon nanotubes. The model is based on the percolation theory [58] that properly predicts the behavior of CNT networks composed of semiconducting/conducing CNTs and air voids. The percolation behavior of the material describes the change of the material from dielectric to conductor due to the insertion of metallic nanotubes which enhances the conductivity of the material.

Above the percolation threshold p_c, the frequency-dependent conductivity of a conductor-insulator mixture can be expressed in terms of a power law relation as:

$$\sigma_{\mathrm{AC}} \propto (p - p_c)^t \text{ for } p > p_c \tag{3.2}$$

where p is the occupation probability and t is the critical exponent. The packing density defined as the ratio of the powder weight to the enclosure volume is adopted in this work as the independent variable describing percolation behavior instead of the volume/weight fraction due to the complex nature of the MUT. The critical exponent t is estimated theoretically to be between 1.6 and 2 for three-dimensional percolation networks. However, experiments show that its value varies from 1.3 to 3.1 [59]. For the studied CNTs, the critical exponent obtained by the

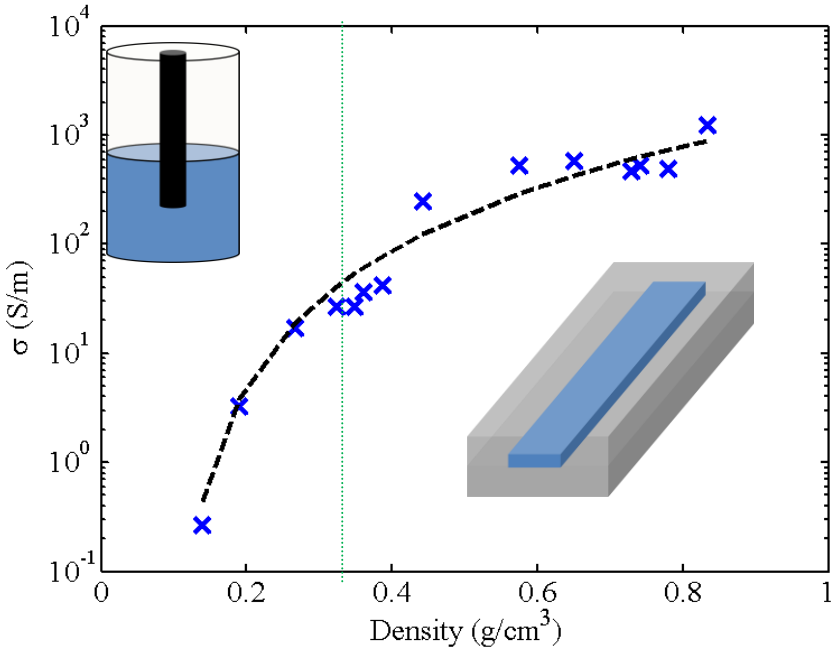

Fig. 3.13: Semi-log plot of the AC conductivity of CNT networks extracted at 100 MHz using two different extraction measurement setups. The probe measurement is used for packing densities below 0.4 g/cm^3 and the transmission line measurement is used for higher packing densities. The dashed line is obtained from (3.2) after fitting the extracted conductivity as shown in Fig. 3.14.

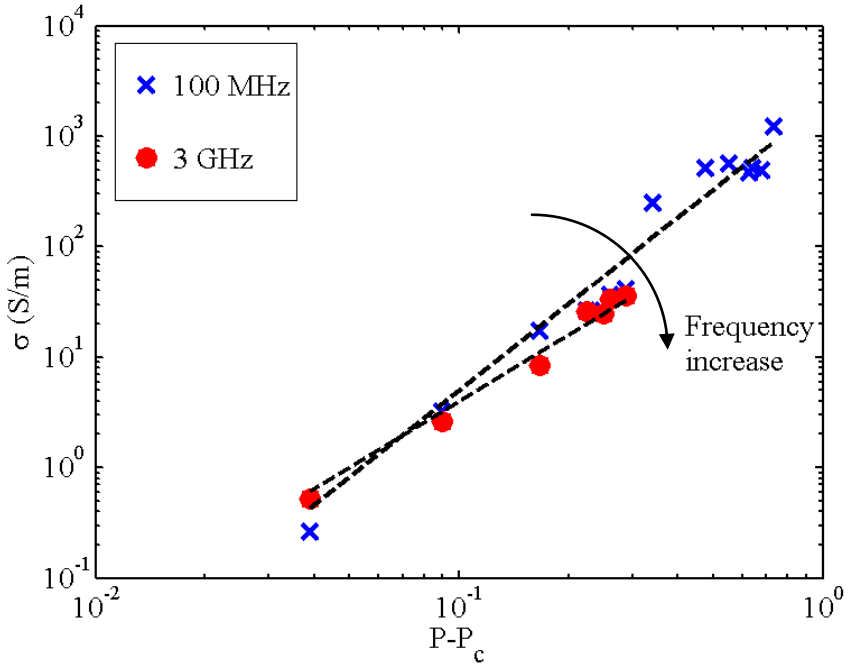

Fig. 3.14: Log-log plot representing the linear regression fitting curves to find percolation parameters based on the power law described in (3.2) and data from Fig. 3.11.

linear regression fitting curve of the conductivity at 100 MHz shown in Fig. 3.12 is 2.6 which agrees with the percolation data reported in the literature. Table I summarizes the percolation parameters using (3.2) obtained at different frequencies from Fig. 3.14 and other measurements as well.

TABLE I

SUMMARY OF THE PERCOLATION PARAMETERS OBTAINED FROM LINEAR REGRESSION FITTING CURVES USING (2) AND EXPERIMENTAL RESULTS

Frequency (MHz)	Percolation threshold P_c	Critical exponent t
50	0.1	2.6
100	0.1	2.6
3000	0.1	2

At low frequencies the variation of the conductivity function of the density is higher as the wavelength of the electromagnetic are larger than the separation between two metallic particles. When the frequency range increases to the GHz range the conductivity decreases as the losses such as skin effect and semiconducting/conducting CNTs interconnect effects cannot be neglected anymore.

IV. ENGINEERED CARBON-NANOTUBES BASED COMPOSITE MATERIAL FOR RF APPLICATIONS[3]

A. INTRODUCTION

The electrical characterization of composite material is particularly interesting for their new electrical properties [62] and [66]. Nelson [67] has described different models to estimate the complex permittivity of bulk material from its pulverized form. However, those models fail in the case of nano-particles as explained in [61] where it is observed the enhancement of the real part of the permittivity of composite nano-material. Also in [64], it is reported at low frequencies in the range of few MHz dramatic values of complex permittivity for carbon nanotube networks where percolation theory [58] is used to interpret the reason for high values for both real and imaginary parts of complex permittivity.

The objective of this work is to explore changing in a controlled manner the complex permittivity of nano-particles of alumina by mixing with carbon nanotubes. For this purpose, the complex effective permittivity of pure alumina nano-particles is obtained. Then, carbon nanotubes in a dry-powder form as furnished by the manufacturer are characterized. Finally, we

---

[3] © 2012 IEEE. Reprinted, with permission, from E. Decrossas, M.A. EL Sabbagh, V. Fouad Hanna and S.M. El-Ghazaly, "Rigorous characterization of carbon nanotube complex permittivity over a broadband of RF frequencies," in *IEEE Transactions on Electromagnetic Compatibility*, vol. 54, no. 1, pp. 81-87, February 2012.
E. Decrossas, M.A. EL Sabbagh, V. Fouad Hanna and S.M. El-Ghazaly, "Engineered Carbon-nanotube Based Composite Materials for RF Applications," *in IEEE Transactions on Electromagnetic Compatibility*,vol. 54, no. 1, pp. 52-59, February 2012.
E. Decrossas, M.A. EL Sabbagh, H.A. Naseem, V. Fouad Hanna, S.M. El-Ghazaly, " Effective permittivity extraction of dielectric nano-powder and nano-composite materials: effects of packing densities and mixture compositions," IEEE European Microwave Week, Manchester, UK, October 9-14, 2011.
E.Decrossas, and S.M. El-Ghazaly. "Microwave characterization of carbon nanotube networks" in Carbon Nanotubes/book 6. S. Bianco, Intech, 2011.

show that by mixing alumina and CNT in a controlled approach, it is possible to synthesize a novel nano-composite material with interesting electrical properties which could have appealing RF applications.

B. DESCRIPTION OF NEW TEST SETUP

To achieve this goal a new measurement setup is used in this work for material characterization similar to one described in chapter 2. This hollow cylinder corresponds to region IV shown in Fig. 4.2 (a) and it is connected to a 50-Ω air-filled coaxial transmission line that corresponds to region I through regions II and III which are air-filled coaxial transitions. This new structure is used to increase the density inside the hollow circular waveguide. In the previous setup the pin of the 2.4 mm male precision adapter protruded inside the circular waveguide filled with pulverized material. When the density becomes too high the pin could not be easily inserted and broke.

Fig. 4.1: Actual picture of the different parts of fabricated test setup. (a) plunger. (b) Plunger support. (c) Coaxial lines of regions I to III. (d) Hollow circular waveguide, region IV. Part (a) goes into (b) on top of (d) to pack the powder inside (d), then removed. Measurements are realized when part (c) is ended with part (d) filled with powder.

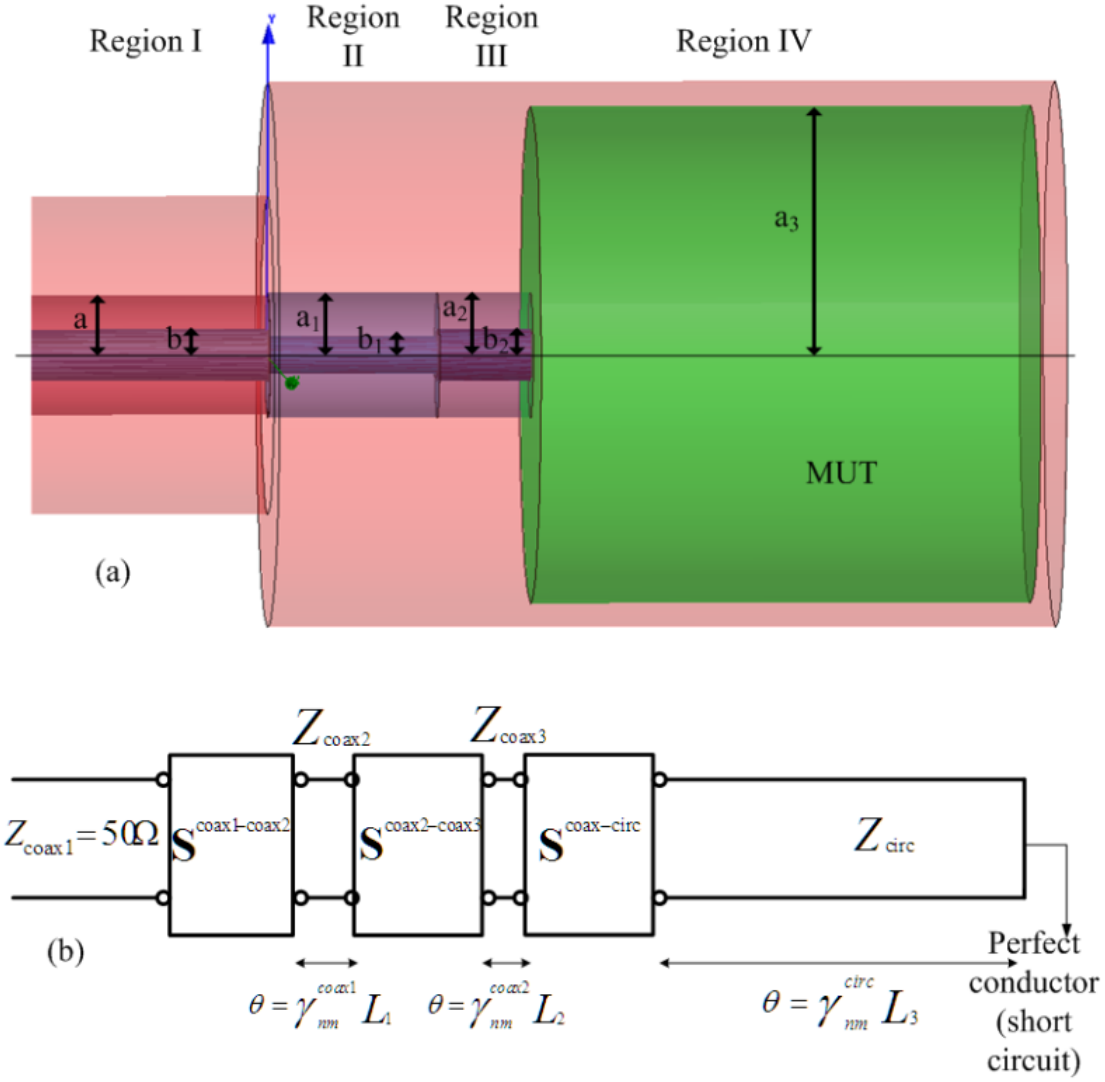

Fig. 4.2: (a) Schematic of the test structure. (b) Cascaded blocks of generalized scattering matrices. The dimensions of setup are: a = 1.2 mm, $b = b_2$ = 0.52 mm, $a_1 = a_2$ = 1.265 mm, b_1 = 0.4 mm, a_3 = 4.9 mm, L_1 = 3.4 mm, L_2 = 1.8 mm, L_3 = 10 mm.

The rigorous derivation of the mode matching technique-based model and convergence studies has been previously discussed in chapter 2. The results presented in chapter 2 show that the permittivity has been successfully retrieved from reflection coefficient (S_{11}) with an error less than 2%. In addition, the extraction procedure has been applied to air as a lossless material and water as a lossy material. The results are in good agreement with other references found in the literature. In [68], the accuracy for the real part of the permittivity ε' less than 3% and the

imaginary part with accuracy less than 5% was reported using an APC7mm connector when the loss tangent $\varepsilon''/\varepsilon'$ is greater than ±0.01, yet the frequency range was limited to 18 GHz.

In this work, we are interested at the frequency band below 3GHz where the carbon nanotube networks present high real and imaginary parts of the complex permittivity as shown in chapter 3. The output ports of this PNA are 1.85 mm connectors. To avoid any phase ambiguity due to calibration, the 50-Ω line of region I is machined with the same dimensions as those of a 2.4 mm male connector. In this case, the 1.85 mm cable is connected directly between the PNA and the testing cell without the need for any adapter in between. The fabrication tolerance of the micro-machined test setup as verified by optical methods is less than 10 μm.

C. RESULTS AND DISCUSSION

The microwave measurements are carried out for pure alumina powder, carbon nanotubes, and a mixture of CNTs and alumina. The alumina used in this work is supplied by South Bay Technology, Inc. The nano particles of alumina have a diameter of 50 nm. The CNTs are provided by Bucky USA (product number BU-203) and they have a purity > 90 wt%, ash < 1.5 wt%, diameter 1 nm to 2 nm, and length 5 μm to 30 μm. For each material, nano-particles are weighted then dropped directly into the hollow-cylinder (region IV) holder. MUT is packed in the holder by exercising manual press through a plunger and a plunger support as shown in Fig. 4.1 (a) and (b), respectively, to progressively increase the density inside the holder shown in Fig. 4.1 (d). The volume of cavity *V* is determined using optical measurements and the weight *M* of MUT is obtained using analytical balance with ±0.01mg resolution. The packing density is computed using the following relation: $\rho = \frac{M}{V}$.

1. Nano-Particles of Alumina

Dry powder of only nano-particles of alumina is used as furnished by the manufacturer. The average size of alumina particles is 50 nm. Fig. 4.3 shows the real and imaginary parts of the extracted complex effective permittivity of pure alumina versus frequency at different packing densities.

Fig. 4.4 presents the variation of complex effective permittivity of alumina versus packing density and volume fraction at a frequency of 3 GHz. Volume fraction is defined as the ratio of the actual volume of nano particles to the total volume of container. In this case, alumina is weighed and the volume is obtained from $V_{act} = \frac{M}{\rho}$ where ρ = 3.9 g/cm^3 for alumina. The volume of holder cavity is 0.7854 cm^3. The linearly extrapolated results shown in Fig. 4.4 suggest that if a packing density equal to the bulk density of alumina is reached then the bulk permittivity of alumina is obtained. This linear variation of complex permittivity versus packing density is different from those models initially proposed in [67] for particles with sizes between 50-100 μm and discussed in [61] to extract bulk permittivity. The reason that initial models introduced in [67] fails for nano-particles is attributed to the reduction of air gaps between particles synthesizing a better homogeneous material as illustrated by the cartoon in Fig. 4.5 where particles are assumed to be spherical in shape. In other words, solid spheres corresponding to the alumina particles with larger radii lead to bigger voids between the particles which are equivalent to an air-alumina mixture and the effective permittivity of the mixed material is dominated by the air permittivity. As the radii of alumina particles decrease, voids between the solid spherical particles are reduced. As the size of interstices becomes smaller than the waveleng th of the electromagnetic waves propagating in the material the alumina nano-particles can be considered quite a homogenous medium.

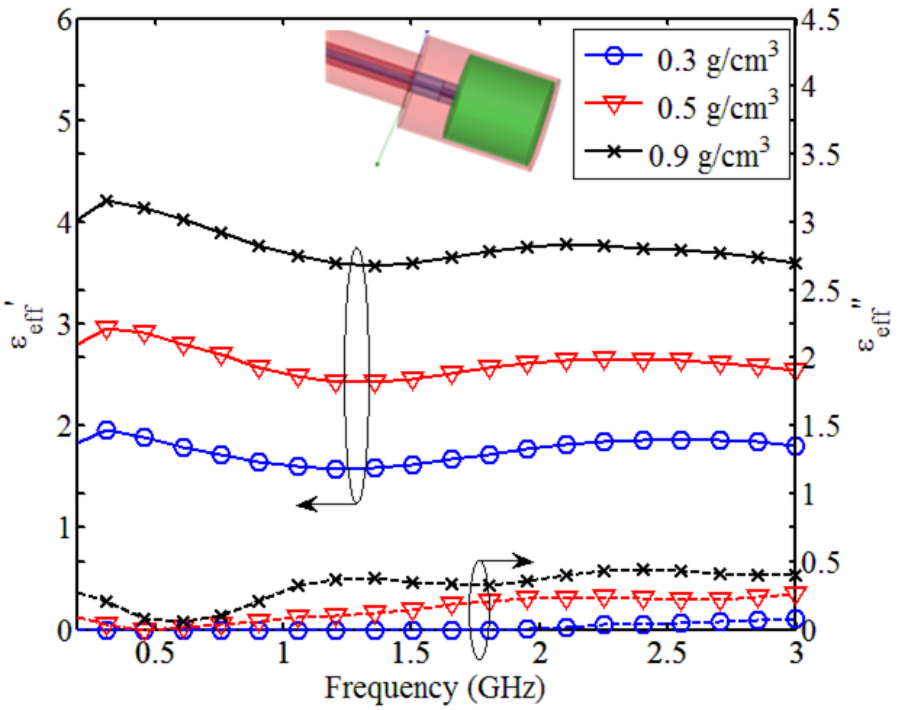

Fig. 4.3: Variation of the extracted complex effective permittivity of alumina versus frequency at different densities using the structure shown in the inset. The left axis corresponds to the real part of complex effective permittivity represented by solid lines while the right axis corresponds to the imaginary part shown by dashed lines. Same marker is used to represent both real and imaginary parts at each packing density.

Meanwhile the size of air interstices between alumina nano-particles decreases, their number has significantly increased. It is reported in [69] that the losses are less sensitive for granular particles with size greater than 3-4 μm in a fully dense material. However, for this case study, the loss dependence is strongly influenced by the porosity of the alumina nano-particles. This explains why the extracted imaginary part of the complex effective permittivity shown in Fig. 4.4 is higher than the one obtained in [69] for sintered alumina.

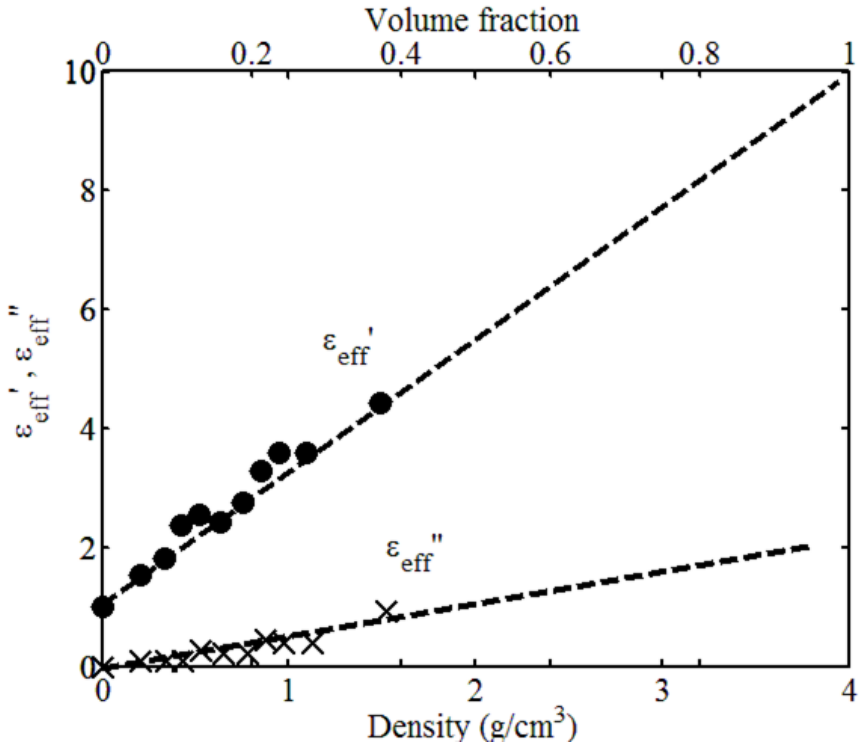

Fig.4.4: Variation of extracted complex effective permittivity of alumina versus packing density or the volume fraction at 3 GHz. The straight dashed black lines represent a linear curve fitting of data. The same scale is used for the real ($\varepsilon'_{\text{eff}}$)and imaginary ($\varepsilon''_{\text{eff}}$) parts of the effective permittivity.

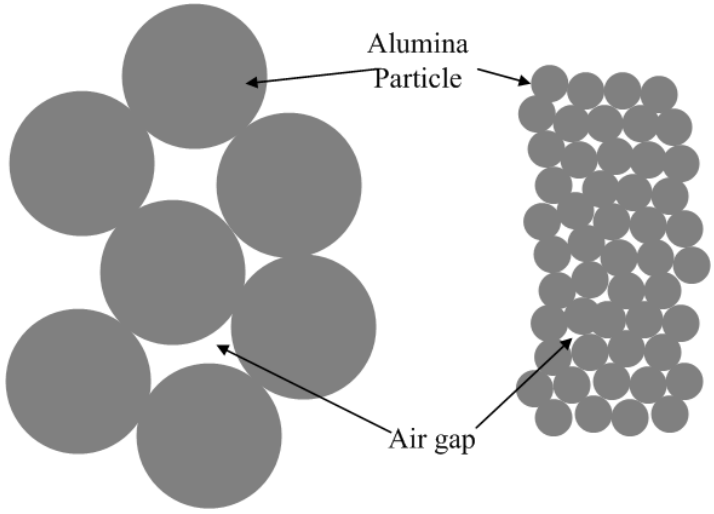

Fig. 4.5: Schematic of alumina particles explaining the dependence of material electrical properties on the size reduction of particles from 50-100μm (left-hand side) to 50nm (right-hand side). Dimensions are not to scale.

It should be noted that the packing density of alumina in the holder is progressively increased. Hence, the ratio of air to alumina is decreasing as the packing density is increased. For the particular scenario where packing density is 0, the holder is entirely empty, i.e., filled with air and the extracted permittivity corresponds to the case of air as shown in [54].

2. Mixture of Carbon Nanotubes with Nano-Particles of Alumina

In this part of study, single-walled CNTs are mixed with nano-particles of pure alumina. The alumina used in this work is supplied by South Bay Technology, Inc. The nano particles of alumina have a diameter of 50 nm. The CNTs are used as provided by Bucky USA (product number BU-203) and they have a purity > 90 wt%, ash < 1.5 wt%, diameter 1 nm to 2 nm, and length 5 μm to 30 μm. Fig. 4.6 is an image obtained by scanning electron microscopy (SEM) of the mixture of 1 g alumina and 0.2 g CNTs. Transmission electron microscopy (TEM) of prepared mixture is shown in Fig. 4.7.

Another procedure used to characterize the mixture is the Energy-dispersive X-ray spectroscopy (EDX) shown in the inset of Fig. 4.7. The EDX where three peaks can be distinguished is representative of the mixture sample realized at different positions in the sample. The first peak indicates the presence of carbon due to CNTs as well as the carbon grid used to deposit the samples explaining the high magnitude compared to other components. The second and third peaks indicate the presence of oxygen and aluminum due to alumina particles (Al_2O_3).

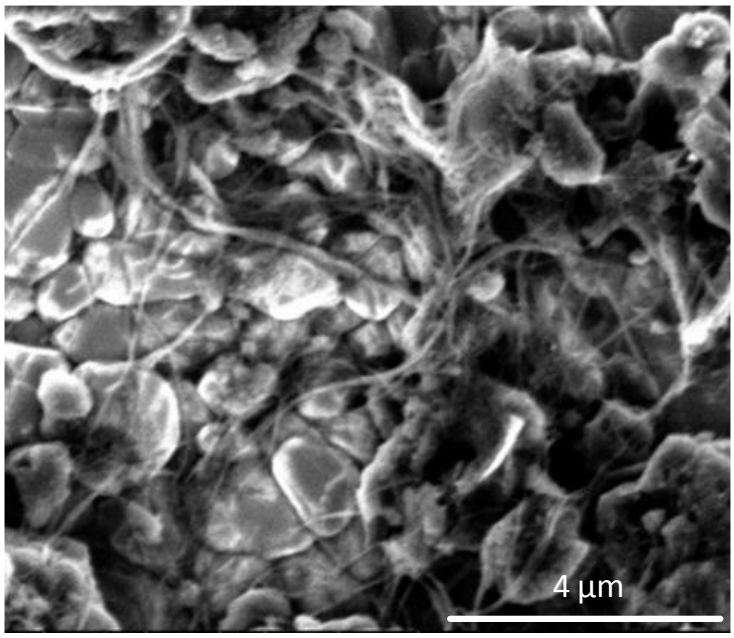

Fig. 4.6: SEM picture of the prepared mixture of 0.2 g carbon nanotubes mixed with 1 g alumina powder.

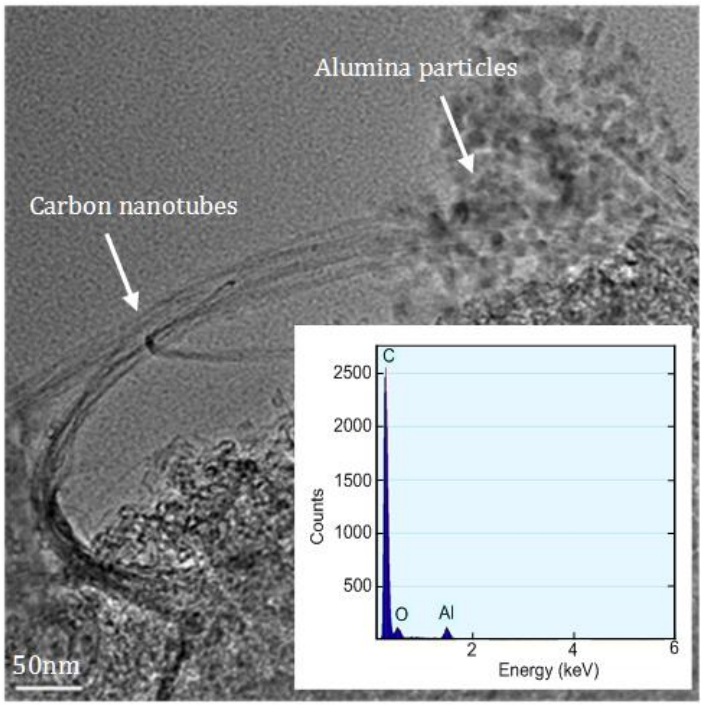

Fig. 4.7: TEM picture of the prepared mixture of alumina and carbon nanotubes. The inset is the EDX showing the different particle components found in the sample.

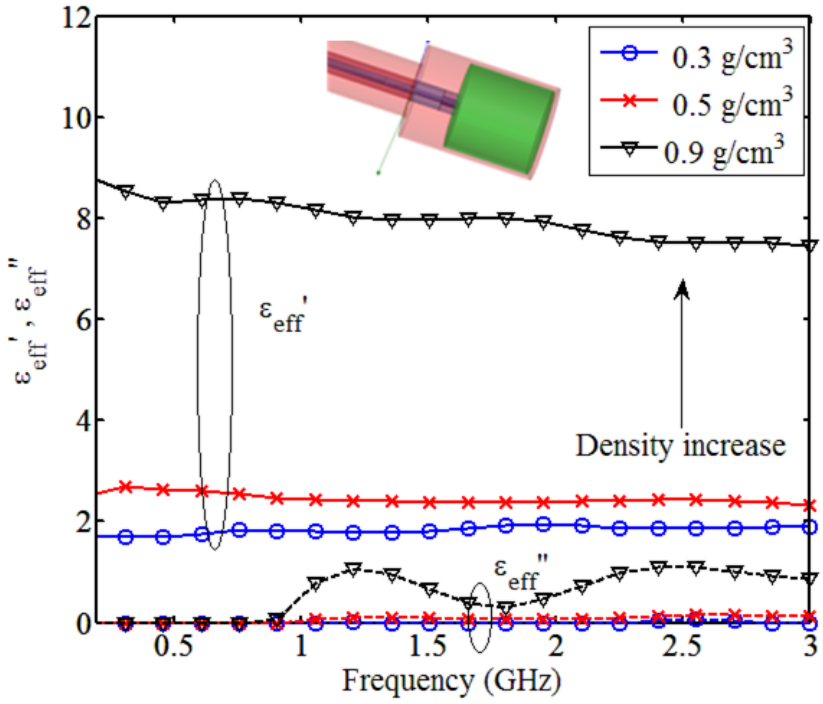

Fig. 4.8: Variation of the complex effective permittivity of a dry mixture of alumina and CNTs. The same marker is used for real and imaginary parts at each packing density. The same scale is used for the real ($\varepsilon'_{\text{eff}}$)and imaginary ($\varepsilon''_{\text{eff}}$) parts of the effective permittivity.

Based on our previous studies presented in chapter 3 the extracted complex permittivity of CNT networks is significantly large at low frequencies as shown in chapter 3 and drops by several orders of magnitude at higher frequencies. This trend is observed regardless of the packing density. At higher frequencies, both real and imaginary parts of the effective permittivity converge to asymptotic values corresponding to bulk material. As we anticipate that the main effect due to the addition of CNTs to alumina medium occurs at low frequencies, we have limited the maximum measurement frequency to 3 GHz.

The complex permittivity of the composite mixture versus frequency from 10 MHz to 3 GHz at different packing densities is presented in Fig.4.8.

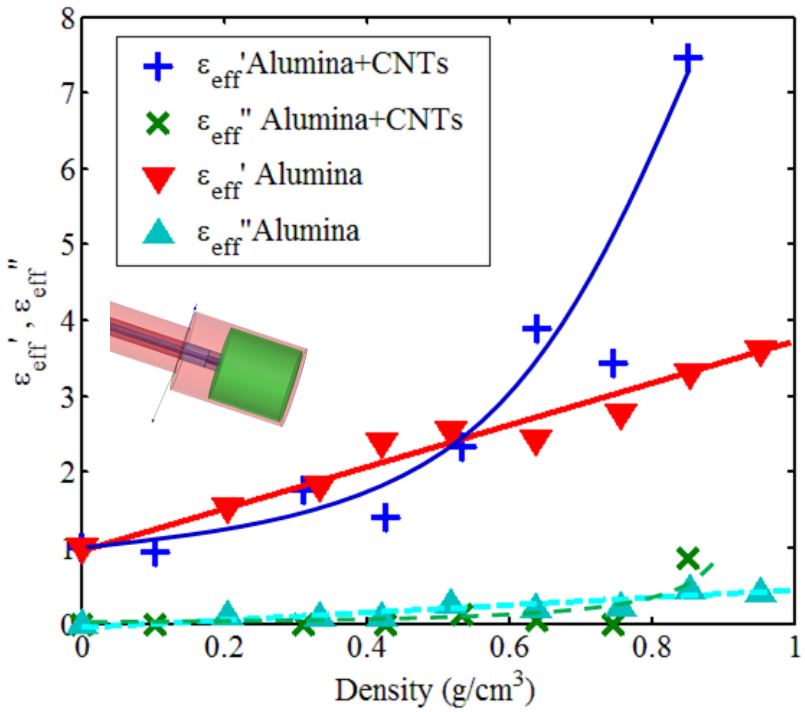

Fig. 4.9: Variation of the real (solid line) and imaginary (dashed line) parts of the complex effective permittivity of a mixture of CNTs and alumina versus density. The data obtained for pure alumina are plotted to highlight the increase of dielectric constant of the composite material. Both real ($\varepsilon'_{\text{eff}}$) and imaginary ($\varepsilon''_{\text{eff}}$) parts of the effective permittivity are plotted on the same scale.

Fig. 4.9 shows the variation of the complex permittivity of a dry mixture of CNTs and alumina versus density at a frequency of 3 GHz. In this figure, the data obtained for pure alumina are also plotted to highlight the increase of dielectric constant due to the mixing with CNTs.

Fig. 4.10 summarizes the loss tangent of all nano-materials characterized in this work. For each material the loss tangent increases with the packing density. Alumina well known as a low loss material is used as a reference as shown by dotted lines in Fig. 4.10. CNTs on the other hand have a high loss tangent as described by the solid lines in Fig. 4.10. By combining the electrical properties of alumina and carbon nanotubes, it is possible to obtain high values of dielectric constant controlled by CNTs as shown in Fig. 4.9 and low loss tangent controlled by alumina as shown in Fig. 4.10.

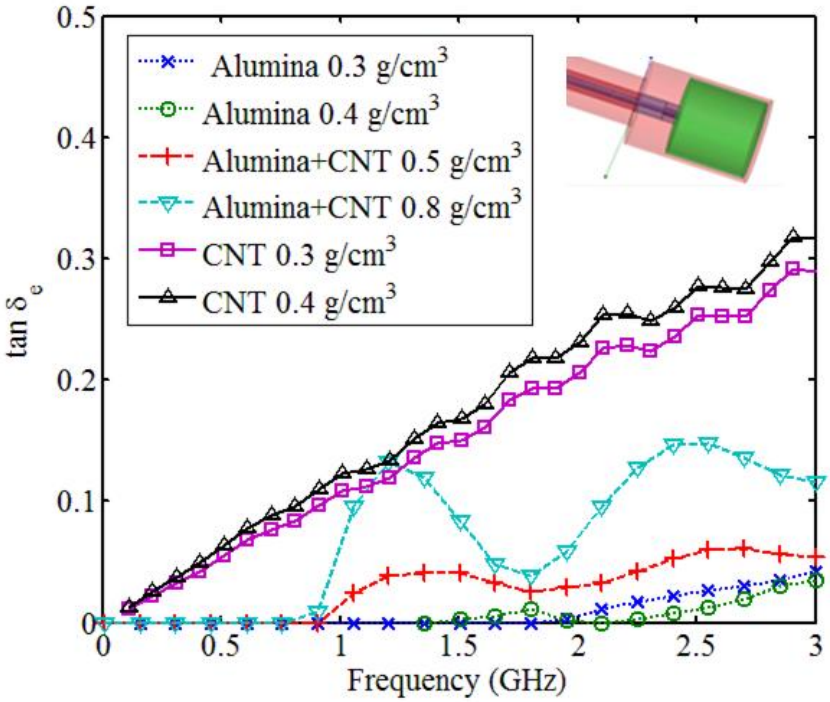

Fig. 4.10: Comparison of the loss tangent obtained for all nanomaterials characterized in this work considering different packing densities: alumina is shown by dotted lines, alumina mixed with carbon nanotubes by dashed lines and pure CNT powder by solid lines.

Fig. 4.9 shows a comparison between the real part of the effective permittivity of alumina mixed with CNTs and pure alumina to highlight the role of CNTs in the enhancement of the real part of the effective permittivity as the packing density increases. The results of alumina mixture with those CNT networks were measured at 60 MHz as we anticipate the most significant effect of CNTs on the mixture. The results in Fig. 4.8 verify the high values of permittivity of CNTs shown in chapter 3. As frequency goes higher, we do not expect that CNTs have that comparable strong effect on permittivity as at low frequencies. The linear increase of permittivity of pure alumina versus packing density is due to addition of more material which replaces air and hence permittivity is increasing. It is noted that the value of dielectric constant for bulk alumina depends on the density of alumina. For example, CoorsTek reports a dielectric constant varying from 8.2 to 9.8 corresponding to Alumina density varying from 3.42 to 3.92, respectively.

Ultimately, if we could reach an ultimate packing density of alumina close to 3.92 g/cm^3, then we expect to have a dielectric constant equal to 9.8. The linear trend of permittivity is based on measurements and studies presented in [65] for the same material.

It is noted that the percolation behavior is enhanced due to the specific shape of nanotubes, the size of nano metallic particles. The cylindrical shapes of CNTs increase considerably the number of interconnection while the nanosize improves the dispersion in the medium.

Link *et al*. in [63] reported the importance of the aspect ratio with respect to the variation of the dielectric constant for gold nanorods and the effect on the dielectric constant of medium.

D. RADIO FREQUENCY (RF) APPLICATIONS

The characterization of the electrical properties of nano-composites is necessary to understand and design novel materials for high-frequency applications. For instance, initial work was carried out in [61] to explore the potential of replacing metallic traces with CNT for interconnect applications. For this purpose equivalent circuit models of those interconnect were developed in [70]-[71]. Dielectric resonators used in microwave/RF circuits require a high-dielectric constant and/or low loss to achieve high quality factor. In addition, the resonant frequency is inversely proportional to the square root of the real part of the permittivity and the dimensions of resonator. Consequently, at low frequencies, dielectric resonators are not used mainly due to their large size. Earlier work by El Sabbagh [72] shows the possibility of building a CNT-based miniaturized resonator.

We have shown that the mixing of CNTs with alumina significantly enhances the real part of permittivity without increasing the losses represented by the imaginary part of the permittivity as shown in Fig.. These results are in agreement with those in [72] confirming the role of CNT to miniaturize RF resonators. Other researchers have shown that above percolation threshold, a

multi-conducting path through the CNT-based composite material can be used to tune the electrical properties of the medium [73] by introducing a small bias voltage across the composite material. This is another interesting application in tunable circuits. Moreover, CNTs composite materials were studied in [74] for electromagnetic interference (EMI) shielding to protect delicate electronic devices against external electromagnetic radiation [75]. Several groups also investigates the electromagnetic compatibility behavior of carbon nanotube interconnects as a possible candidates to replace copper in future electronics [76]-[77]. In the last decade, high-k gate dielectric appeared in semiconductor technology and progressively replaced silicon dioxide insulator layers to further miniaturize microelectronic components without sacrificing the performance of CMOS transistors at high frequency [78]. Our work shows that CNT-based composites may be a possible candidate as future high-k gate dielectric implemented in high-frequency silicon-based transistors.

Several research groups have demonstrated the RF applications in radio systems where carbon nanotubes detect an amplitude modulation (AM) signal in a functioning radio receiver as replacement of diode in current radio systems [79]-[80]. CNTs are also among the possible candidates to implement future high frequency transistors due to their quasi-ballistic electron transport and their high intrinsic cut-off frequencies (up to terahertz). The main challenge is to control the alignment and the deposition of CNTs to form a semiconducting channel between the drain and source. Several alignment techniques have been investigated such as droplet, dielectrophoresis, Langmuir-Blodgett, spin coating and chemical vapor deposition (CVD) methods [81]; however, fabrication of CNT-field effect transistor (CNT-FET) on a large scale integration still needs to be improved to be competitive compared to traditional silicon based FET.

V. CARBON-NANOTUBE BASED ELECTRONIC AND OPTOELECTRONIC DEVICES

A. INTRODUCTION

As presented in chapter 1, electronic properties of carbon nanotubes are anisotropic and are present along their longitudinal axis depending on their chirality and the tube diameter. Therefore, to fully exploit these properties it is necessary to control the alignment and the deposition of CNT networks. For this purpose, the alignment technique is realized by dielectrophoresis (DEP) where the process uses the electrical force generated by an electric field between two isolated electrodes. Thus, the medium enclosed by the electrodes tends to align the polarized suspended particles along the electrical field lines [82]-[84].

The forces acting on the suspended carbon nanotubes during the alignment process are computed from the electrical properties of CNTs networks previously extracted at low frequencies (MHz) [36], [56] and [64]. This work is based on theoretical and experimental studies of the DEP process to fully investigate the optimized parameters controlling the alignment depending on the distance between the electrodes, the applied voltage magnitude and frequency. Then, the electrical contact between the electrodes and CNTs alignment is verified using scanning electron microscopy (SEM) images and I-V measurements.

Following the alignment, a high bias voltage is applied to selectively keep the semiconducting carbon nanotubes and burn the conducting ones by Joule heating [85].

The purpose of this project is to study the possibility to design novel electronic/optoelectronic devices using aligned semiconducting carbon nanotubes. The gained knowledge and general results will be helpful in implementing future CNT-based high-frequency device models.

B. DIELECTROPHORESIS (DEP) THEORY

DEP is a process where an electrical field is generated by applying a potential difference between two isolated electrodes. Under this condition suspended particles in a neutral aqueous solution confined between a pair of electrodes become polarized and tend to align along the electrical field lines as shown in Fig. 5.1.

This process involves controlling the electrical field related to the applied AC voltage and the distance between the electrodes. In addition, the surface area of deposition can be controlled by reducing the width or the shape of the electrodes. To describe the phenomenon acting the suspended carbon nanotubes, it is necessary to study the combination of dielectrophoretic force acting on CNTs and electro-thermal force acting on the medium (fluidic motion).

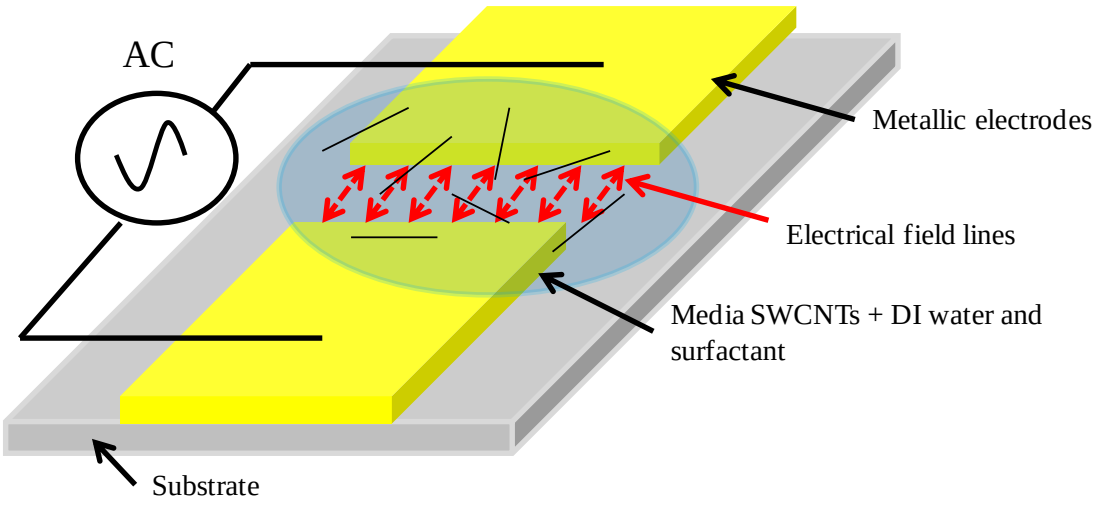

Fig. 5.1: A schematic of the experiment setup used for DEP process to align the CNTs. The figure shows that a small droplet of CNTs aqueous solution is deposited between two metallic electrodes. Then an AC signal is applied to align the carbon nanotubes along the electrical field lines.

The DEP force, F_{DEP} acting on the suspended CNTs can be described as [84]-[86]:

$$F_{DEP} = \Gamma\, \varepsilon_m\, Re\{F_{CM}\}\nabla|E_{rms}|^2 \tag{5.1}$$

where $\Gamma = \frac{\pi}{6} r^2 l$ represents the shape factor and $F_{CM} = \frac{\varepsilon_p^* - \varepsilon_m^*}{\varepsilon_m^*}$ is the real part of the Clausius-Mossoti factor of suspended particles with high aspect ratio such as carbon nanotubes. *r* is the radius and *l* the length of the particles, E_{rms} is the root mean square (RMS) electric field. The complex relative permittivities presented in the Clausius-Mossoti factor are defined as:

$$\varepsilon_p^* = \varepsilon_p - i\,\frac{\sigma_p}{2\pi f} \qquad\qquad \varepsilon_m^* = \varepsilon_m - i\,\frac{\sigma_m}{2\pi f}$$

where the subscript (*p* or *m*) denotes the permittivity of particles or medium respectively.

From the Clausius-Mossoti factor is should be noted that the dielectrophoretic force can be either positive or negative. When DEP is positive suspended particles migrate to the high electric field gradient regions. Otherwise, carbon nanotubes travel to low electric field gradient regions. Hence, by using different electrodes shape to narrow the high electric field gradient area in addition to positive dielectrophoresis, it is possible to control the position and the alignment of the carbon nanotubes.

In addition to the DEP force, the electro-thermal force due to the fluidic motion induced by Joule heating also translates the suspended particles. The electro-thermal force is the force acting on the suspending liquid medium produced by applying an external electric field on the liquid medium [84]:

$$F_e = -M\left(\frac{\varepsilon_m \sigma_m V_{RMS}^4}{2k_T \pi^3 g^3 T}\right) \tag{5.2}$$

where g is half the length of the gap and M is a dimensionless factor defined by

$$M = \frac{(T/\sigma_m)(\partial\sigma_m/\partial T) - (T/\varepsilon_m)(\partial\varepsilon_m/\partial T)}{1 + (2\pi f\tau)^2} + \frac{1}{2}\frac{T}{\varepsilon_m}\frac{\partial\varepsilon_m}{\partial T} \tag{5.3}$$

where V_{rms} is the root mean square AC voltage, k_T is the suspending medium thermal conductivity, T is suspending medium temperature and $\tau = \frac{\varepsilon_m}{\sigma_m}$ is the charge relaxation of the medium.

Similarly to the DEP force, the electro-thermal force can be either positive or negative. When F_e is negative the fluidic motion tends to push away the suspended particles from the electrode gap. Inversely, if the electro-thermal force is positive, the fluid flows into the gap, enhancing the carbon nanotubes migration.

C. FORCES CALCULATION

The variation of the dielectrophoretic force function of the AC applied voltage frequency is computed from equation (5.1) based on the information given by the carbon nanotubes manufacturer and/or extracted from experimental results. The average diameter of the CNTs is 20 nm and the length is 20 µm. The conductivity σ_p and relative permittivity ε_p are $4.10^4 S/m$ and $4.5.10^6 \varepsilon_0 F/m$ respectively reported in [87]. The suspending aqueous medium is dionized (DI) water with a conductivity σ_m of $10^{-3} S/m$ and relative permittivity ε_m of $80\varepsilon_0 F/m$ from [37]. The distance between the isolated electrodes is 100 µm. The square field gradient $\nabla|E_{rms}|^2$ is computed based on the RMS applied voltage and the gap length between the electrodes $\nabla|E_{rms}|^2 = \frac{\left|\frac{V_{RMS}}{gap}\right|^2}{gap}$. It should be noted that we have assumed here that the real part of the permittvity stays constant with the frequency which is only valid at low frequencies up to a few MHz. The dielectric constant is related to the motion of the particles under an external electric field. In other words, when the electric field switches the polarized particle need a certain time called relaxation time to align along the electric field lines.

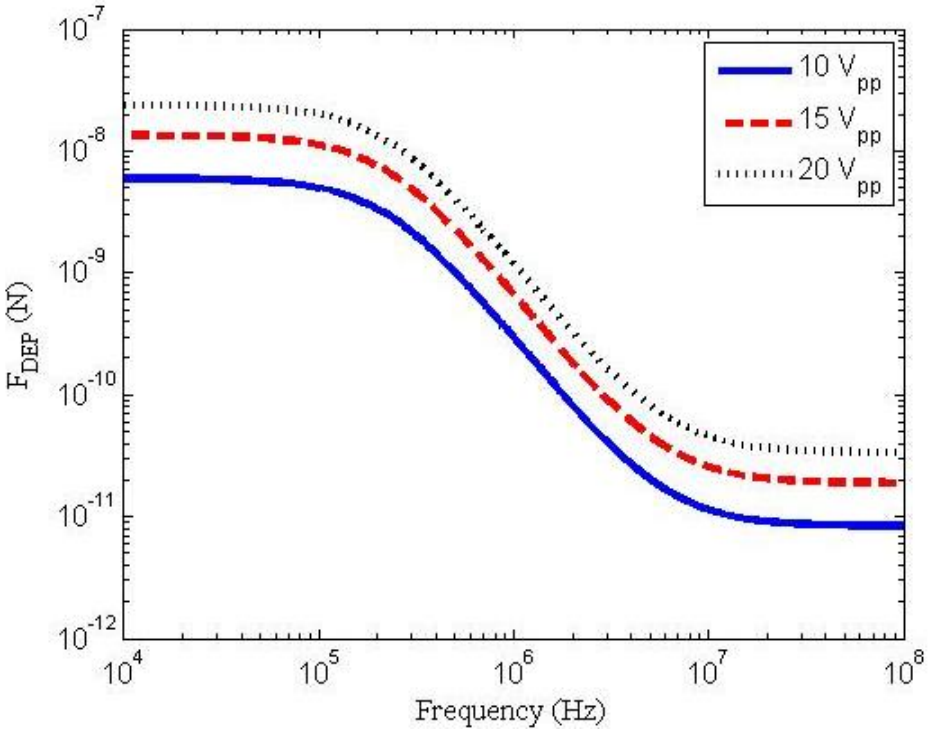

Fig.5.2: Dielectrophoretic force as a function of alignment frequency at different applied peak to peak voltage considering a gap of 100 µm between the electrodes.

From Fig. 5.2, it is clear that the dielectrophoretic force is always positive, depending on the Clausius-Mossoti term; the complex permittivity of CNTs is significantly higher than the relative complex permittivity of DI water. The variation of the DEP force with respect to the frequency suggests two constant regions: Below 100 KHz, the force is principally controlled by the relative conductivities of the CNTs and suspending medium, otherwise, above 10 MHz, the controlling factor becomes the permittivities of the carbon nanotubes and DI water. The variation of dielectrophoretic force from 10^{-8}N to 10^{-11}N, indicates that the frequency and the magnitude of the applied voltage doesn't play a major role in the alignment compared to the difference of relative complex permittivitties between the medium and suspended particles described by the Clausius-Mossoti factor.

Similarly, the variation of the electro-thermal force acting on the suspending aqueous medium with the frequency is investigated through (5.2) and (5.3). The thermal conductivity

k_T of DI water is $0.6\ \mathrm{W/(m^2.K)}$ at room temperature (300K). In addition, $(1/\sigma_m)(\partial\sigma_m/\partial T)$ is assumed to be 0.02^oC^{-1} and $(1/\varepsilon_m)(\partial\varepsilon_m/\partial T)is-0.004^oC^{-1}$ from [84].Unlike, the DEP force, the electro-thermal force is negative at low frequencies and positive at high frequency as illustrated by Fig. 5.3.

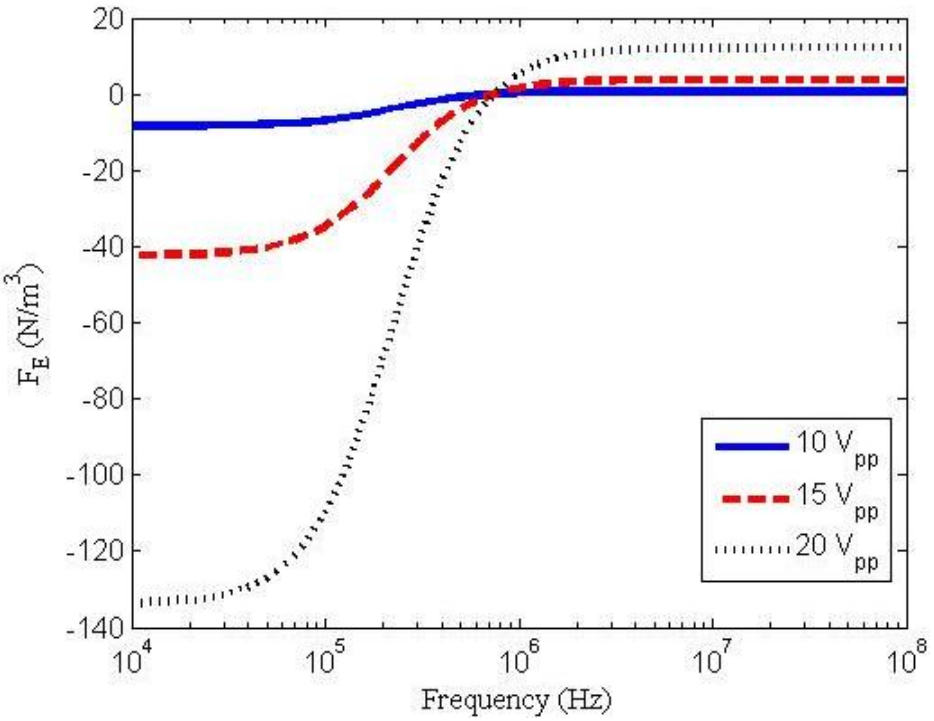

Fig.5.3: Electro-thermal force as a function of alignment frequency at different applied peak to peak voltage considering a gap of 100 µm between the electrodes.

The cross-over frequency occurs around 1 MHz, which corresponds to negative-positive transitions shown in Fig. 5.3. Unlike the DEP force, frequency is the controlling factor and should be above 1 MHz in order to ensure a positive electro-thermal force.

Fig. 5.4 summarizes the phenomenon acting on the suspended particles when the electro-thermal force is either positive or negative. In other words, the forces acting on the suspended particles need to act in the same direction to enhance the migration of the carbon nanotubes into the electrodes gap.

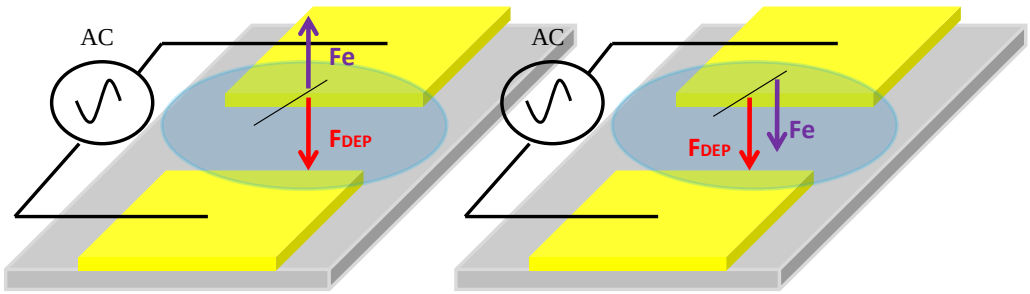

(a) (b)

Fig. 5.4: Comparison of the forces acting on the suspended particles below 1 MHz (a) and above 1 MHz (b) frequency due the electro-thermal and dielectrophoretic forces highlights the choice of the applied AC signal frequency.

Therefore, the theoretical study of the dielectrophoresis process shows that to optimize the alignment of carbon nanotubes, we have to use an AC voltage source generating the highest peak to peak voltage at a frequency higher than 1 MHz to ensure a positive electro-thermal force.

D. EXPERIMENTAL RESULTS

In this project, bundled networks of single-walled CNTs are used as provided by the manufacturer (Sigma-Aldrich): the sample purity is 50 to 70 volume percentage as determined by Raman spectroscopy and scanning electron microscopy (SEM). Moreover, the sample contains residual catalyst impurities nickel and yttrium. The lengths of CNTs are approximately 20 μm. According to the manufacturer, SEM pictures show the presence of multi-walled carbon nanotubes as well as single-walled CNTs within the sample. The CNTs suspension for DEP was prepared using an analytical balanced with a precision of 0.01 mg to weight the CNTs powder grown by arc discharge process.

The carbon powder was mixed with 10 ml of deionized (DI) water and two drops (~10 μl) of Nanosperse®, poly(oxy-1,2-ethandiyl, an alpha-(nonylphenyl)-omega-hydroxy based surfactant designed to accelerate the dispersion of carbon nanotubes in water. The liquid mixture was

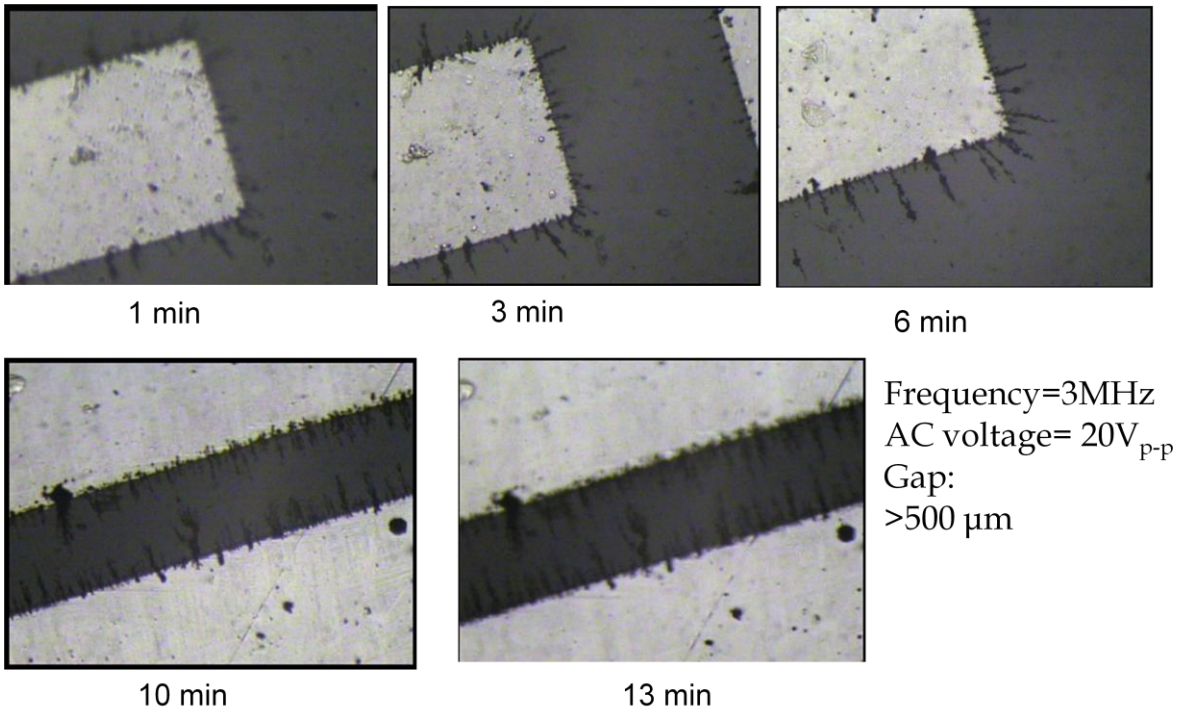

Fig.5.5: Screen captures of the alignment of CNTs during DEP process for different times using a CCD camera (40x magnifications) coupled with microscope (10x magnification).

sonicated at 44 KHz in an ultrasonic bath 10 min, and then dropped in the gap between a pair of electrodes using an Eppendorf pipette as shown in Fig. 5.1.

Fig. 5.5 shows the alignment of CNTs during the DEP process, it is clear from the pictures that aligned carbon nanotubes actually grows from each sides of the electrodes to meet in the middle of the gap. In addition, we have chosen to show the alignment at one corner to show that the electric field is more concentrated at this point and consequently, explains why the traces of CNT are longer than the traces at the edges of the electrodes.

The aligned carbon nanotubes are obtained when all liquid is evaporated, the time for the DEP process is usually between 10-15 min. Therefore, the time depends on the droplet shape and amount of deposited liquid on the electrodes. When the surface contact of the drop with the electrodes is large the evaporation time decreases. To optimize the alignment parameters and verify the contact between the electrodes a series of experimental measurements were carried out

after the dielectrophoresis process. After complete evaporation of the solution, the samples were dried in an oven to completely remove liquid particles.

E. DC RESISTANCE OF THE DEPOSITED CNT-BASED TRACE

1. Functions of the Applied Voltage

From the DEP theory developed in the previous section, we have shown that the applied AC voltage is the main alignment factor because both forces are sensitive to it. Fig. 5.6 shows the variation of the measured resistance considering two gap lengths after DEP process. It should be noted that we have neglected the resistive contact between the two electrodes when the resistance is in the order of MΩ. For this experiments the DEP frequency was fixed to 3 MHz and the 1.5 mg of carbon nanotubes powder were suspended in a 10 ml DI water solution containing 2 drops of surfactant. A droplet size of 5 µl was deposited between the electrodes as shown in Fig. 5.1.

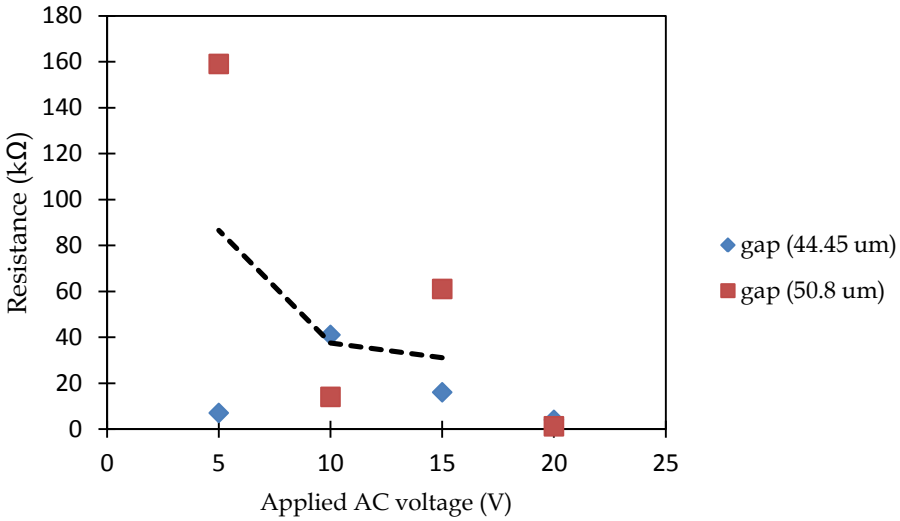

Fig. 5.6: Variation of the measured resistance functions of the applied voltage between the electrodes after the DEP process. The black dashed line is the mean value obtained from the different measurements

Multi-traces of carbon nanotubes between the electrodes have been observed during the DEP process as shown on Fig. 5.5 explaining the discrepancies between the measured resistances. Consequently, the repeatability of the results gives a standard deviation of 40% on the resistance value then decreases to 10% when the applied AC voltage is higher than 10 V_{p-p} considering a gap length from 12.7 µm (0.5 mil) to 50.8 µm (2 mils).

2. Functions of the Applied Frequency

Here, all the parameters are kept constant and only the frequency of the applied AC voltage is tuned as shown in Fig. 5.7. As presented in the previous section, measured resistances in the order of MΩ have been neglected. Fig. 5.7 shows that around 1 MHz the values of the measured resistances are steadier with a standard deviation of 10%. It is noted that this specific frequency is the cross-over frequency that we have theoretical computed for the negative-positive transition of the electro-thermal force. In addition, below 1 KHz we have observed the apparition of bubbles occurring in the gap during the dielectrophoresis process, due to the electrolyze of the electrodes (oxidation of the metal). Theoretical and experimental studies demonstrated that an AC voltage higher than 10 V_{p-p} in addition to a frequency above 1 MHz should insure a good alignment and repeatable measurements.

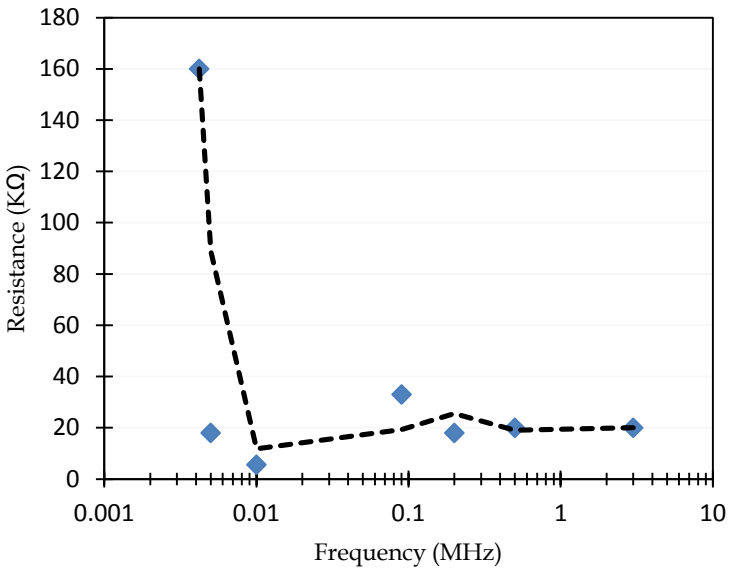

Fig. 5.7: Variation of the measured resistance functions of the applied AC frequency after DEP process with the following parameters: applied voltage 20 V_{pp}, drop size 5 µl and gap length 19.05 µm.

3. Functions of the Distance Between the Electrodes

To fully understand the variation of the resistance function of the gap, we have increased by four the concentration of carbon nanotubes in the solution to insure a contact between the electrodes.

Fig. 5.8 clearly shows that the resistance increases with the distance between electrodes. The repeatability of the measurements shows a 15% standard deviation. The black dashed line is the linear mean between the measurements to highlight the increase of the resistance function of the gap. In this case, a linear average has been privileged based on the resistance expression of a trace $R = \rho \frac{L}{A}$ where R is the resistance, ρ is the resistivity, L the length of the conducting path and A the cross section of the trace.

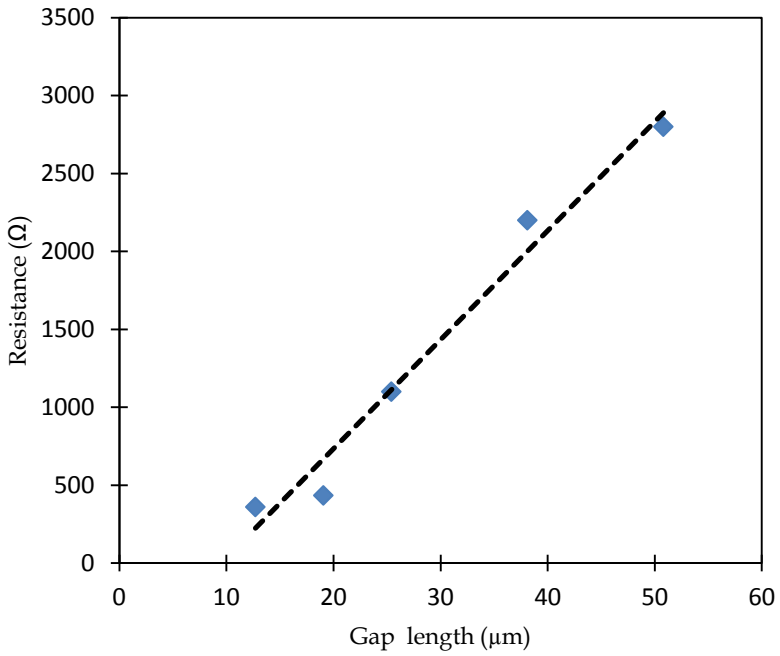

Fig. 5.8: Variation of the measured resistance functions of the gap length between the electrodes with the following parameters: frequency 3 MHz, applied voltage 20 V_{pp} and drop size 5 µl.

4. Functions of CNTs Concentration in the Solution

Fig. 5.9 shows that the resistance decreases with the concentration of CNTs suspended in the aqueous solution. The data from Fig. 5.9 are plotted to highlight the effect of the carbon nanotubes concentration on the resistance measurements. Usually, a ratio of one semiconducting to three conducting CNTs is produced depending on their chirality [8]-[9]. In addition, our samples present some particles of metal catalyst which also increase the conductivity of the trace. In other words, by increasing the concentration, we have also increased the metallic conducting particles in the trace and consequently improve the contact between the electrodes. To fabricate the high concentration solution, we have doubled the amount of carbon powder in the DI water solution.

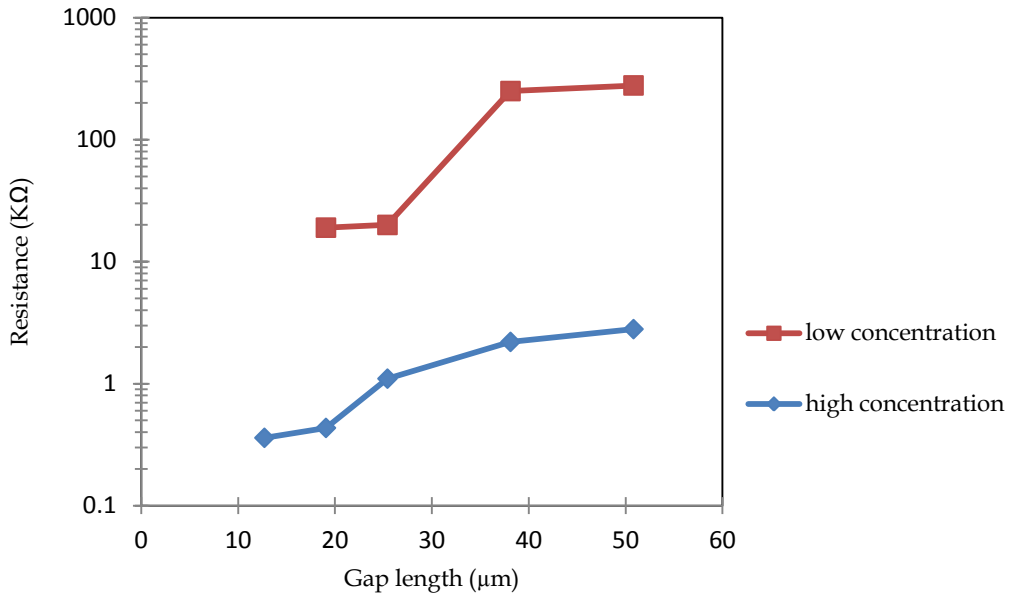

Fig. 5.9: Variation of the resistance functions of the distance between electrodes at different CNTs concentration in the aqueous solution with the following parameters: frequency 3 MHz, applied voltage 20 V_{pp}, drop size 5 µl and high concentration 3 mg.

5. Functions of the Surface Area of Deposition

The width of the electrodes has been reduced from 1 cm to 1 mm decreasing the surface area deposition of CNTs. Consequently, less carbon nanotubes are present in the gap and explain the larger value of the measured resistance compared to larger electrodes width as shown on Fig. 5.10. In addition more CNTs are present on the substrate around the electrodes where the forces acting on the carbon nanotubes were too weak to attract the particles in the gap between the electrodes. However, we are able to confine the carbon nanotubes deposition and reduced the number of CNTs traces between the electrodes as presented in Fig. 5.13.

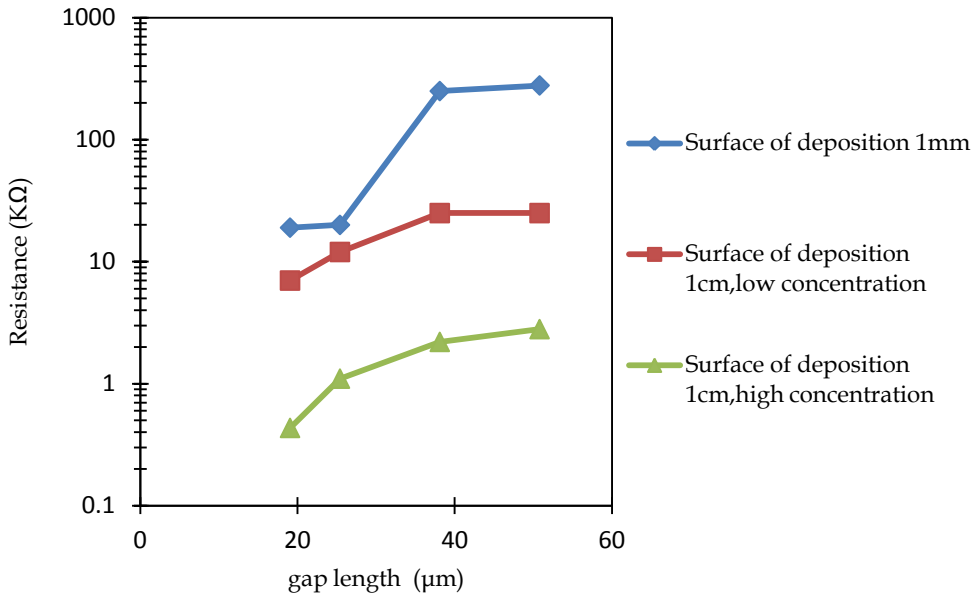

Fig. 5.10: Variation of the surface deposition area functions of the gap considering different electrodes width and concentration of CNTs in the aqueous solution with the following applied parameters: frequency 3 MHz, applied voltage 20 V_{pp}, drop size 5 µl and high concentration 3 mg.

6. Approximation of the Dielectric Constant and Conductivity

It is possible to approximate the dielectric constant of the carbon nanotubes considering that a gap filled with a dielectric material delimitated by the electrodes defined a capacitance as shown on Fig. 5.11 where the capacitance from the glass substrate is in parallel with the carbon nanotubes capacitance.

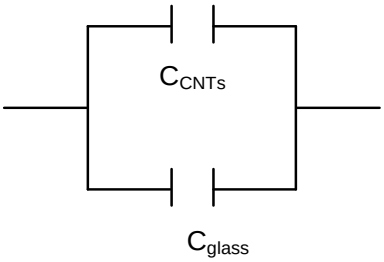

Fig. 5.11: equivalent parallel capacitance of the design.

Therefore, to find the value of the equivalent capacitance, we have to add the two parallel capacitances. The values found in Fig. 5.12 are much higher than C_{glass}. Consequently, we can neglect the capacitance created by the glass substrate. By roughly approximating the electrodes by two parallel plates, we can extract the dielectric constant from the simple calculation:

$$\varepsilon_p = \frac{d * C}{\varepsilon_0 * A} \tag{5.4}$$

where A represents the width of the trace multiply by the height of the electrodes, C is the measured capacitance represented in Fig. 5.11, d is the distance between the electrodes, ε_0 the vacuum permittivity.

The plot clearly shows that the capacitance decreases with the gap length. The measures of the capacitance have been realized by using a capacimeter. First, the value of the capacitance without any CNTs trace C_{glass} value was below 1 pF and reached the limit of the capacimeter. Additionally, the variation of the capacitance is inversely proportional to the distance between the electrodes which is represented by the dark mean line as presented on Fig. 5.12.

By averaging the value of the dielectric constant we found: $\varepsilon_p = \sim 4.5.10^6$. This very high value of the dielectric constant is coherent with data presented in chapter 3.

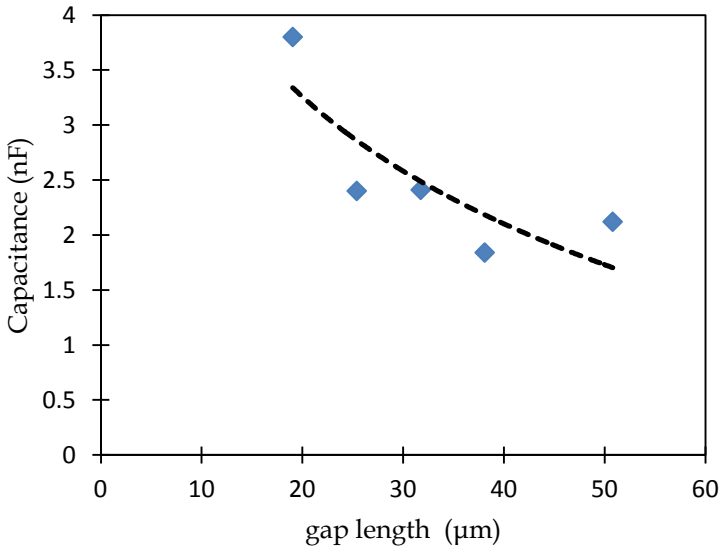

Fig. 5.12: Variation of the capacitance functions of the distance between the electrodes.

Similarly to the measurements of the capacitance between the electrodes, we have measured the resistance. Knowing the width of the trace, the height of the electrodes and the length between the electrodes we can approximate the resistivity or the conductivity of the trace as:

$$\sigma_p = \frac{L}{R * A} \tag{5.5}$$

where L is the distance between the electrodes, A represents the width of the trace multiply by the height of the electrodes and R the measured resistance obtained in Fig. 5.10. By averaging the value of the conductivity, we found: $\sigma_p = \sim 4.10^4$ S/cm. Again this calculation is a rough approximation and is coherent with the values found in chapter 3.

7. Tuning the Width of the CNTs Trace due to the Shape of the Electrodes

By changing the tip angle at the end of the electrodes, it is possible to tune the width of the CNT-based trace as shown on Fig. 5.13. The alignment is realized on alumina substrate.

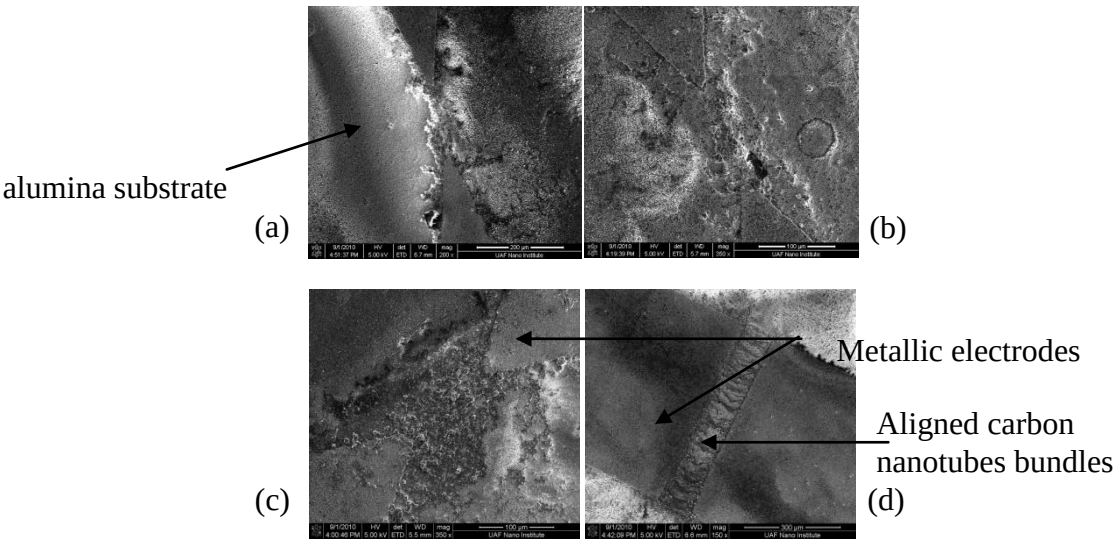

Fig. 5.13: SEM picture of aligned CNTs between two electrodes separated by 100µm after applying the dielectrophoresis process for different tip angle (a) 30°, (b) 45°, (c) 60°, and (d) 180°.

The alignment of bundled carbon nanotubes can be seen on the SEM picture Fig. 5.13 for the case where the tip angle is varying 30^{o} (trace width ~50 μm), 45^{o} (trace width ~70 μm), 60 ^{o} (trace width ~100 μm), 180^{o} and the distance between the electrodes is 100 μm.

F. I-V MEASUREMENTS

Usually, bundles of carbon nanotubes present both semiconducting and conducting CNTs depending on their chirality [88]. For this reason, when the alignment of CNTs is realized, we have increased the current between the electrodes to burn the conducting CNTs using the Joule effect properties [89]. Fig. 5.14 presents the I-V characteristic of the aligned carbon nanotubes trace before and after applying a 70 V bias DC voltage for 5 minutes. It is clear that the measured current decreases from mA to μA suggesting that the conducting carbon nanotubes have burned.

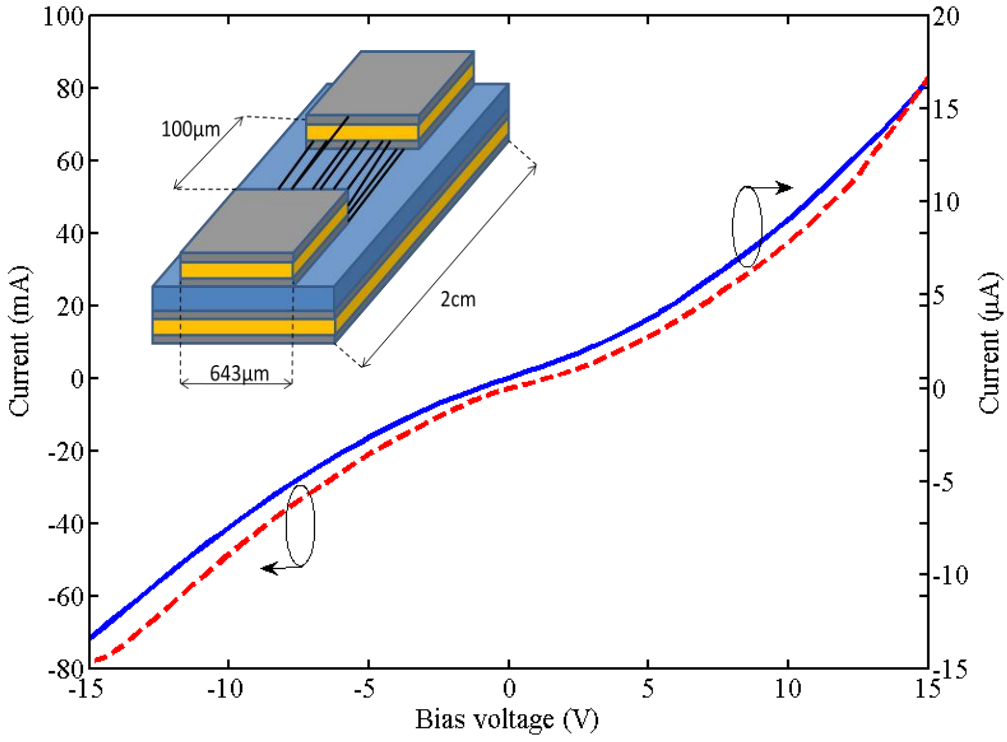

Fig. 5.14: I-V curves comparison before and after applying 70V bias voltage to burn the conducting CNTs. The red dashed curve is the measurement after deposition of the CNTs as presented in Fig. 5.13 while the blue curve is the measurement after applying high bias voltage for 5 minutes.

In semiconductor physics, single-walled carbon nanotubes present an interesting direct band gap structure inversely proportional to their diameter, expressed [90]:

$$E_g = \frac{0.692}{d} \tag{5.6}$$

where E_g is the energy band gap in eV and d the diameter of the nanotubes in nm. The diameter is related to the chirality of the CNTs and the constant value is a fitting curve parameter usually defined between 0.6 and 0.8 eV. When the energy of the photon emitted by the light is higher than the band gap energy, an electron can migrate from the valence band to the conduction band and create an electron-hole pair. By applying a bias voltage, it is possible to collect this electron and enhance the current, this is the so called photocurrent. By substituting the value of the band gap energy for 1 nm SWCNT diameter, we can evaluate the light wavelength necessary to excite the electrons. This wavelength corresponds to the infrared band, widely used in communication system. Therefore, based on the properties of the semiconducting nanotubes and the previous calculation, it shows that the aligned CNTs vary with the light intensity as presented in Fig. 5.15.

$$\lambda > \frac{hc}{E_g} \approx \frac{1240}{0.692} = 1792 \text{ nm} \tag{5.7}$$

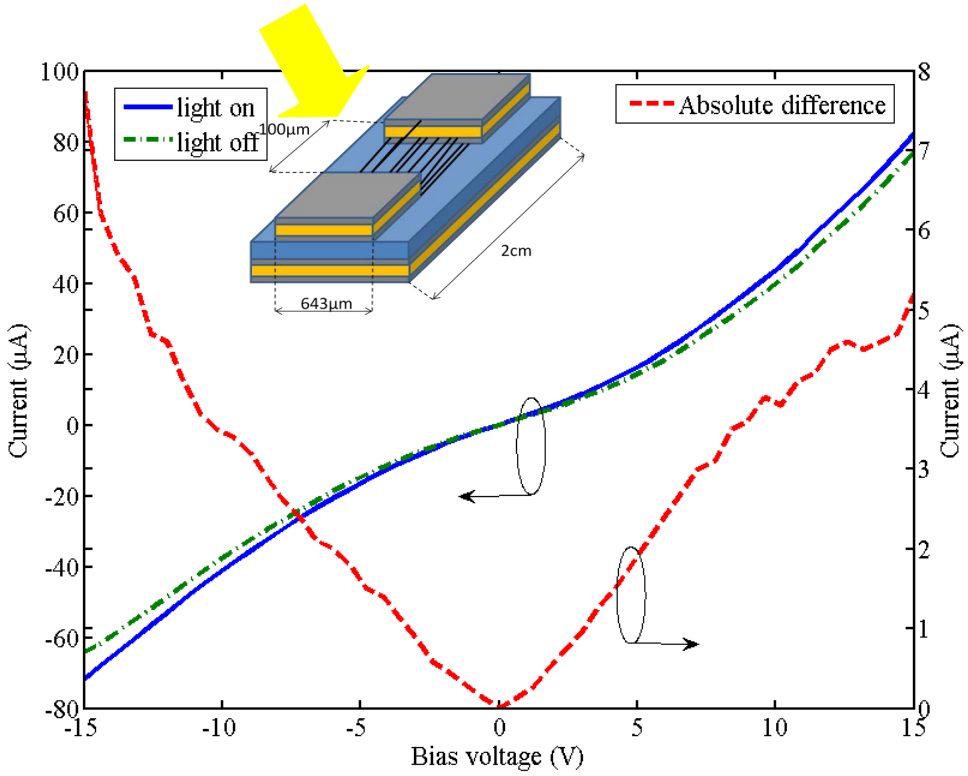

Fig. 5.15: Comparison of the I-V curves with (blue line) and without (green dashed line) light. The red dashed line is the absolute difference between the two measurements.

Thus, using the dielectrophoresis process, we have been able to produce aligned semiconducting carbon nanotubes between two metallic electrodes**.** In addition, experimental results have shown that it is possible to control the alignment and the surface area of deposition. Then, the demonstration of the semiconducting selection and the optical properties of carbon nanotubes have indicated the possibility to design novel optoelectronic devices.

VI. CONCLUSIONS AND FUTURE WORK

The extraction process developed in chapter 2 is a combination of accurate modeling using the full-wave mode matching method, experimental measurements and mathematical optimization. The MMT is used to accurately model coaxial and circular discontinuities more efficiently than using commercial software based on the finite element methods. The study of the convergence criteria allowed us to choose adequately the number of modes necessary to accurately model each region with an optimized computing time. Then, an optimized gradient method is performed to vary the complex permittivity until the convergence criteria based on the difference between the modeled and measured reflection coefficient S_{11} are achieved. The experimental measurement matches well the MMT model and the extracted complex permittivity is validated using both lossless and lossy material under test and compared with published data in the literature.

In chapter 3, a non-destructive, low-cost, easily implemented technique where only a small fraction of material is presented to characterize carbon nanotube based materials in powder form over a broadband of RF frequencies. Only a single measurement setup is required to achieve characterization over the broadband of frequencies from 10 MHz to 50 GHz. Finally, the frequency dependence of effective complex permittivity and the effects of the packing density of CNTs networks are presented. The effective conductivity of CNT is modeled based on the percolation theory. Experimental results are obtained using two different extraction methods over a large range of packing densities varying from low values up to the theoretical density of CNTs. The mathematical expression computed from the percolation control parameters after fitting the experimental curves is a real achievement to improve simulation models for future CNTs high-

frequency devices. Based on the results presented in this work, it is possible to predict the proper weight of the CNT networks to obtain the desired conductivity.

In chapter 4, the technique is applied to nano-particles of pure alumina, carbon nanotubes, and to a mixture of alumina and carbon nanotubes. For alumina, the linear dependence of complex effective permittivity on packing density gives an estimate of the permittivity of bulk material. The dramatic values of the real and imaginary part of the complex permittivity of CNTs at low frequencies are due to the interaction of metallic and dielectric nano-particles. The nonlinear behavior of the variation of the permittivity as a function of the packing density is experimentally demonstrated for a mixture of carbon nanotubes and alumina. The possibility to engineer CNT-based composites material with a high-dielectric constant and low loss has been shown. The compositions as well as the dispersion of the carbon nanotubes in a dielectric medium will be the key to engineer those new microwave composite materials.

In chapter 5, a complete procedure to build carbon nanotubes based devices has been described, derived from the theoretical and experimental study of the dielectrophoresis process. Our preliminary results help to understand the behavior of semiconducting CNTs and highlight the possibility to design novel electronic/optoelectronic devices. However, it is necessary to improve experiments by increasing the purity of the carbon nanotubes and the alignment process. To enhance the optical response of the carbon nanotubes, the bundled CNTs need to be removed and the metallic contact between the carbon nanotubes trace and the electrodes studied.

This work can lead to novel optoelectronic devices and optic to microwave converters using the unique properties of semiconducting carbon nanotubes. Moreover, the infrared response of single-walled carbon nanotubes may contribute to new 1.55 μm wavelength communication

system widely used in fiber-optic. Furthermore, a new research area is investigating THz devices where this frequency band is the missing link between microwave and optic research.

1. Future Improvement of the CNT-Based Prototype

A new prototype consisting of semiconducting single-wall carbon nanotube (s-SWCNT) is evaluated to enhance the photo-response of the carbon nanotubes: After fabricating nano-electrodes as shown in Fig. 6.1, deposition and alignment of s-SWCNT is realized using the dielectrophoresis (DEP) technique. The scanning electron microscope (SEM) pictures show a few aligned carbon nanotubes in the 300 nm gap between the two nano-electrodes. Then, I-V measurements are conducting considering the device shown in Fig. 6.1. Preliminary results suggest that the increase number of aligned s-SWCNT between the electrodes enhances the measured current functions of the applied voltage as shown in Fig. 6.2. In addition, when measurements are realized in the dark and when light is applied on the device, a small enhancement of the measured current has been observed at room temperature. Although those measurements are quite noisy, the data suggest the light sensitivity of the devices as shown in Fig. 6.2. The 99%+ single-walled semiconducting nanotubes are suspended in the aqueous solution as furnished by the manufacturer Nanointegris.

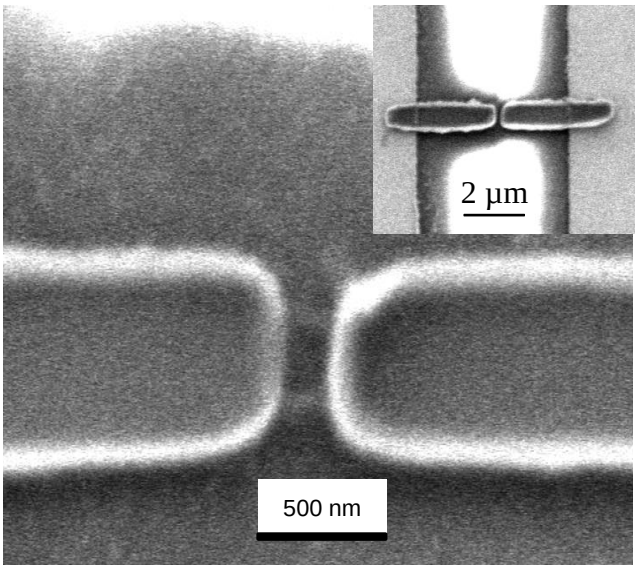

Fig. 6.1: SEM picture of a few aligned semiconducting SWCNTs. The inset presents a low magnification of the fabricated titanium (Ti) nano-electrodes on glass wafer.

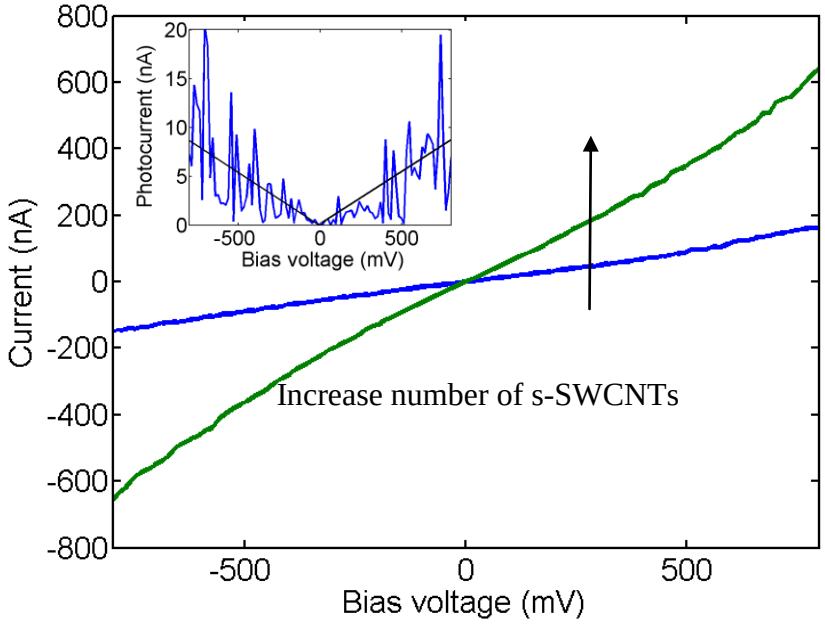

Fig. 6.2: IV-curve realized of the CNT prototype showing the increased current with the number of CNT entrapped between the electrodes. The inset shows some sort of photocurrent based on the absolute difference of measurements realized in the dark and when light is applied on the device. The black lines suggest the trend followed by the measurements considering different devices.

The next steps involve the improvement of the devices by using palladium (Pd) nano-electrodes instead of titanium. Literature reviews show that Schottky contacts created at the

semiconducting carbon nanotubes-metal interface can be minimized using Pd electrodes. More optical experiments should be carried out to verify the light or thermal sensitivity of the devices and decrease the noise considering different light sources based on the wavelengths and radiated power. In addition, the contact resistance between the metallic electrodes and the s-SWCNT should be determined more precisely to evaluate the light or thermal sensitivity of the nanotubes. The yield fabrication process consisting of photolithography and electron beam lithography (EBL) should also be improved to be able to repeat measurements with more consistency and carried out high frequency experiments.

REFERENCES

[1] S. Iijima, "Helical microtubules of graphitic carbon," *Nature,* vol. 354, pp. 56-58, Nov. 1991.

[2] L.V. Radushkevich and V.M. Lukyanovich, "The structure of carbon formed by thermal decomposition of carbon monoxide on an iron contact" *J. Phys. Chem.*, vol. 26, no. 88, pp. 88-95,1952 in Russian.

[3] A. Oberlin, M. Endo, and T. Koyama, "Filamentous growth of carbon through benzene decomposition" *J. of Crystal Growth,* vol. 32, no. 3, pp. 335–349, Mar. 1976.

[4] J. Abrahamson, P.G. Wiles, and B.L. Rhoades, "Structure of carbon fibers found on carbon arc anodes," in *14th Biennial Conf. Carbon*, Pennsylvania State University, PA, 25-29 Jun. 1979, pp. 1873-1874.

[5] M. Monthioux and V.L. Kuznetsov, "Who should be given the credit for the discovery of carbon nanotubes?," *Carbon*, vol. 44, no. 9, pp. 1621–1623, 2004.

[6] H.G. Tennent, "Carbon fibrils, method for producing same and compositions containing same," U.S. Patent 4663230, May 5, 1987.

[7] K.S. Novoselov, A.K. Geim, S.V. Morozov, D. Jiang, Y. Zhang, S.V. Dubonos, I.V. Grigorieva and A.A. Firsov, "Electric field effect in atomically thin carbon films," *Science*, vol. 306, no. 5696, pp. 666-669, Oct. 2004.

[8] M.J. O'Connell, *Carbon Nanotubes Properties and Applications* (1st ed.), CRC Press LLC, Florida, USA, 2006.

[9] A. Jorio, M.S. Dresselhaus, & G. Dresselhaus, *Carbon Nanotubes: Advanced Topics in the Synthesis, Structure, Properties, and Applications*, Springer, New York, USA, 2008.

[10] R. Saito, G. Dresselhaus, & M.S. Dresselhaus, *Physical Properties of Carbon Nanotubes*, Imperial College Press, London, UK, 1998.

[11] A.K. Geim and K. S. Novoselov, "The rise of graphene," *Nature Materials*, vol. 6, pp. 183-191, 2007.

[12] S. Iijima and T. Ichihashi, "Single-shell carbon nanotubes of 1-nm diameter," *Nature*, vol. 36, pp. 603-605, Jun. 1993.

[13] M.O. Manasreh, "*Semiconductor Heterojunctions and Nanostructures,"* New-York: McGraw-Hill, 2005.

[14] P. Avouris, J. Appenzeller, R. Martel, and S.J. Wind, "Carbon nanotube electronics," *Proc. IEEE*, vol. 91, no. 91, pp. 1772-1784, Nov. 2003.

[15] P.L. McEuen, M. S. Fuhrer, and H. K. Park, "Single-walled carbon nanotube electronics," *IEEE Trans. Nanotechnology*, vol. 1, no. 1, pp. 78-85, Mar. 2002.

[16] J. Guo, "Carbon nanotube electronics: modeling, physics, and applications," Ph.D. dissertation, Dept. Electron. Elect. Eng., Purdue University, West Lafayette, IN, Aug. 2004.

[17] M. Meyyapan, *Carbon Nanotubes: Science and Applications* (1st ed.), CRC Press LLC, Florida, USA, 2005.

[18] M.S. Dresselhaus, G. Dresselhaus, and P. Avouris, *Carbon Nanotubes Synthesis, Structure, Properties and Applications*, Springer, Berlin, 2001.

[19] M.S. Arnold, A.A. Green, J. F. Hulvat, S.I. Stupp and M.C. Hersam, "Sorting carbon nanotubes by electronic structure using density differentiation," *Nature Nanotechnology*, vol. 1, pp. 60-65, Oct. 2006.

[20] M.C. Hersam, "Progress towards monodisperse single-walled carbon nanotubes," *Nature Nanotechnology*, vol. 3, pp. 387-394, Jul. 2008.

[21] L.F. Chen, C.K. Ong, C.P. Neo, V.V. Varadan, V.K. Varadan, *Microwave Electronics: Measurement and Materials Characterization*, John Wiley & Sons, 2004.

[22] M.U. Afsar, J.R. Birch, R.N. Clarke, and G.W. Chantry, "The measurement of the properties of materials," *Proc. IEEE*, vol. 74, no. 1, pp. 183–199, Jan. 1986.

[23] J. Baker-Jarvis, M.D. Janezic, J.H. Jr. Grosvenor, and R.G. Geyer, *Transmission/ Reflection and Short-circuit Line Methods for Measuring Permittivity and Permeability*, NIST Technical Note 1355 (revised), U. S. Department of Commerce, 1993.

[24] P. Guillon, "Microwave techniques for measuring complex permittivity and permeability of materials," *Mater. Process. Wireless Commun.*, T. Negas and H. Lings, Eds., The American Ceramic Society, Westerville, pp. 65–71, 1995.

[25] J. Krupka and C. Weil, "Recent advances in metrology for the electromagnetic characterization of materials at microwave frequencies", in *12th Int. Conf. Microw. Radar*, vol. 4, pp. 243–253, Krakow, Poland, 20-22 May 1998.

[26] P.C.P. Watts, D.R. Ponnampalam, and W.K. Hsu, "The complex permittivity of multi-walled carbon nanotube-polystyrene composite films in X-band," *Chem. Phys. Lett.*, vol. 378, no. 5-6, pp. 609-614, Sept. 2003.

[27] P. Potschke, S.M. Dudkin, and I. Alig, "Dielectric spectroscopy on melt processed polycarbonate-multiwalled carbon nanotube composites," *Polymer*, vol. 44, no. 17, pp. 5023-5030, Aug. 2003.

[28] J.K.W. Sandler, J.E. Kirk, I.A. Kinloch, M.S.P. Shaffer, and A.H. Windle, "Ultra-low electrical percolation threshold in carbon-nanotube-epoxy composites," *Polymer,* vol. 44. No. 19, pp. 5893-5899, Sept. 2003.

[29] B. Kim, J. Lee, and I. Yu, "Electrical properties of single-wall carbon nanotube and epoxy composites," *J. Appl. Phys.,* vol. 94, no. 10, pp.6724-6729, Sept. 2003.

[30] C.A. Grimes, C. Mungle, D. Kouzoudis, S. Fang, and P.C. Eklund, "The 500 MHz to 5.50 GHz complex permittivity spectra of single-wall carbon nanotube-loaded polymer composites," *Chem. Phys. Lett.,* vol. 319, no. 5-6, pp. 460-464, Mar. 2000.

[31] C.A. Grimes, E.C. Dickey, C. Mungle, K.G. Ong and D. Qian, "Effect of purification of the electrical conductivity and complex permittivity of multiwall carbon nanotues," *J. Appl. Phys.,* vol. 90, no. 8, pp 4134-4137, Jul. 2001.

[32] J. Wu and L. Kong, "High microwave permittivity of multiwalled carbon nanotube composites," *Appl. Phys. Lett.,* vol. 84, no. 24, pp. 4956-4958, Jun. 2004.

[33] Z. Liu, G. Bai, Y. Huang, F. Li, Y. Ma, T. Guo, X. He, X. Liin, H. Gao, and Y. Chen, "Microwave absorption of single-walled carbon nanotubes/soluble cross-linked polyurethane composites," *J. Phys. Chem. C.,* vol. 111, no. 37, pp. 13696-13700, Jun. 2007.

[34] L. Liu, S. Matitsine, Y.B. Gan, L.F. Chen and L.B. Kong, "Frequency dependence of effective permittivity of carbon nanotube composites," *J. Appl. Phys.,* vol. 101, no. 9, pp. 094106 (1-7), May 2007.

[35] S.L. Bednarz, R. Daussin, C. bailly, X. Lou, J-M. Thomassin, C. Pagnoulle, C. Detrembleur, R. Jerome, and I. Huynen, "Carbon nanotube composites for broadband microwave absorbing materials," *IEEE Trans. Microw. Theory Tech.,* vol. 54, no. 6, Jun. 2006.

[36] H. Xu, M. Anlage, L. Hu, and G. Gruner, "Microwave shielding of transparent and conducting single-walled carbon nanotube films," *J. Appl. Phys.* vol. 90, 183119 (1-3), May 2007.

[37] E. Decrossas, M.A. EL Sabbagh, V. Fouad Hanna and S.M. El-Ghazaly, "Mode matching technique based modeling of coaxial and circular waveguide discontinuities for materials characterization purposes" *Int. J. Microw. Wireless Tech.,* vol. 3, pp. 679-690, Sep. 2011.

[38] E. Decrossas, M.A. EL Sabbagh, V. Fouad Hanna, S.M. El-Ghazaly, "Broadband characterization of carbon nanotube networks," in *IEEE Int. Symp. Electromagn. Compat.,* Fort Lauderdale, Florida, Jul. 25-30, 2010.

[39] Agilent 85070E Dielectric probe kit 200 MHz to 50 GHz manual.

[40] J.R. Whinnery, H.W. Jamieson, and T.E. Robbins, "Coaxial-line discontinuities" *Proc. IRE.*, vol. 32, no. 11, pp. 695-709, Sept. 1944.

[41] N.E. Belhadj-Tahar, and A. Fourrier-Lamer, "Broad-band analysis of a coaxial discontinuity used for dielectric measurements," *IEEE Trans. Microw. Theory Tech*., vol. 34, no. 3, pp. 346-349, Mar. 1986.

[42] T. Itoh, *Numerical Techniques for Microwave and Millimeter Wave Passive Structures*, John Wiley and Sons, New York, 1989.

[43] G.V. Eleftheriades, A.S. Omar, L.P.B. Katehi, and G.M. Rebeiz, "Some important properties of waveguide junction generalized scattering matrices in the context of the mode matching technique," *IEEE Trans. Microw. Theory Tech.*, vol. 42, no. 10, pp. 1896-1903, Oct. 1994.

[44] A. Wexler, "Solution of waveguide discontinuities by modal analysis," *IEEE Trans. Microw. Theory Tech.*, vol. 15, no. 9, pp. 508-517, Sept. 1967.

[45] O. Picon, V. Fouad Hanna, J. Citerne, J.-P. Lefevre, "Exact calculation of scattering parameters of the coplanar-slot transition in unilateral finline technology," *IEEE Trans. Microw. Theory Tech.*, vol. 35, no. 12, pp. 1408-1413, Dec. 1987.

[46] M.A. EL Sabbagh, "Cad of waveguide discontinuities transitions and applications in filters and multiplexers," Ph.D. dissertation, Dept. Elect. Comput. Eng., Univ. Maryland, College Park, MD, 2002.

[47] Ansoft HFSS, Pittsburgh, PA, Version 12.1.2, 2010.

[48] S. Trabelsi, A.W. Kraszewski, and S.O. Nelson, "Phase-shift ambiguity in microwave dielectric properties measurements," *IEEE Trans. Instrum. Meas.*, vol. 49, no. 1, pp. 56–60, Feb. 2000.

[49] D.M. Pozar, *Microwave Engineering*, John Wiley & Sons, New Jersey, 2005.

[50] N.W. McLachlan, *Bessel Functions for Engineers*, Lowe & Brydone, London, 1961.

[51] G.R. Walsh, *Methods of Optimization*, John Wiley & Sons, New Jersey, 1975.

[52] MATLAB Ver. 7.10.0.499 (R2010a), MathWorks, Inc., Natick, MA, 2010.

[53] U. Kaatze, "Complex permittivity of water as a function of frequency and temperature," *J. Chem. Eng. Data*, vol. 34, no. 4, pp. 371-374, Oct. 1989.

[54] E. Decrossas, M.A. EL Sabbagh, V. Fouad Hanna and S.M. El-Ghazaly, "Rigorous characterization of carbon nanotube complex permittivity over a broadband of RF frequencies," *IEEE Trans. Electromagn. Compat.*, vol. 54, no. 1, pp. 81-87, Feb. 2012.

[55] M.A. EL Sabbagh and S. M. El-Ghazaly, "Measurement of dielectric properties of carbon nanotube networks used to build planar transmission lines," in *IEEE Int. Symp. Electromagn. Compat.*, pp. 112-117, Austin, TX, 17-21 Aug. 2009.

[56] N.N. Al Moayed, U.A. Khan, M. Obol, S. Gupta, and M.N. Afsar, "Characterization of single- and multi-walled carbon nanotubes at microwave frequencies," in *Instrum. Meas. Tech. Conf.,* Warsaw, Poland, 1-3 May 2007.

[57] F. He, S. Lau, H.L. Chan, and J. Fan, "High dielectric permittivity and low percolation threshold in nanocomposites based on poly (vinylidene fluoride) and exfoliated graphite nanoplates," *Adv. Mat.,* vol. 21, no. 6, pp. 710-715, Dec. 2009.

[58] D. Stauffer and A. Aharony, *Introduction to Percolation Theory,* Taylor and Francis, Washington, DC, 1992.

[59] N.K. Shrivastava, B.B. Khatua, "Development of electrical conductivity with minimum possible percolation threshold in multi-wall carbon nanotube/polystyrene composites," *Carbon*, vol. 49, no. 13, pp. 4571-4579, Nov. 2011.

[60] L. Wang, and Z.M. Dang, "Carbon nanotube composites with high dielectric constant at low percolation threshold," *Appl. Phys. Lett.*, vol. 87, no. 4, pp. 042903 (1-3), Jul. 2005.

[61] E. Decrossas, M.A. EL Sabbagh, H.A. Naseem, V. Fouad Hanna, S.M. El-Ghazaly, " Effective permittivity extraction of dielectric nano-powder and nano-composite materials: effects of packing densities and mixture compositions," in *IEEE European Microw. Week,* Manchester, UK, 9-14 Oct. 2011, pp. 956-959.

[62] N. Guo, S.A. DiBenedetto, P. Tewari, M.T. Lanagan, M.A. Ratner, and T.J. Marks, "Nanoparticle, size, shape, and interfacial effects on leakage current density, permittivity, and breakdown strength of metal oxide-polyolefin nanocomposites: experiment and theory," *Chem. Mater*., vol. 22, no. 4, pp.1567–1578, Jan. 2010.

[63] S. Link, M.B. Mohamed, and M.A. El-Sayed, "Simulation of the optical Absorption spectra of gold nanorods as a function of their aspect ratio and the effect of the medium dielectric constant," *J. Phys. Chem*. B, vol. 103, no. 16, pp. 3073-3077, Apr. 1999.

[64] M.A. EL Sabbagh, S.M. El-Ghazaly, and H.A. Naseem, "Carbon nanotube-based planar transmission lines," in *IEEE MTT-S Int. Microwave Symp. Dig.*, Boston, MA, 7-12 June 2009, pp. 353-356.

[65] R. Ravindran, K. Gangopadhyay, S. Gangopadhyay, N. Mehta and N.Biswas, "Permittivity enhancement of aluminum oxide thin films with the addition of silver nanoparticles," *J. Phys. D: Appl. Phys*., vol. 89, no. 26, pp. 263511 (1-3), Dec. 2006.

[66] D. Gerbson, J. P. Calame, and A. Bimboim, "Complex permittivity measurements and mixings laws of alumina composites*," J. Appl. Phys*, vol.89, no.12, Jun. 2001.

[67] S.O. Nelson, "Estimation of permittivities of solids from measurements on pulverized or granular materials," in Dielectric Properties of Heterogeneous Materials, A. Priou, Ed. New York: Elsevier, 1992, vol. 6, ch.6.

[68] N.-E. Belhadj-Tahar, O. Meyer, and A. Fourrier-Lamer, "Broad-Band Microwave Characterization of Bilayered Materials Using a Coaxial Discontinuity with Applications for Thin Conductive Films for Microelectronics and Material in Air-Tight Cell," *IEEE Trans. Microw. Theory Tech*, vol. 45, no, 2, pp. 260-267, Feb. 1997.

[69] S.J. Penn, N. Mc.Alford, A. Templeton, X. Wang, M. Xu, M. Reece, and K. Schrapel, ''Effect of Porosity and Grain Size on the Microwave Dielectric Properties of Sintered Alumina,'' *J. Am. Ceram. Soc.*, vol. 80, no. 7, pp.1885–1888, Jul. 1997.

[70] M.A. EL Sabbagh and S.M. El-Ghazaly, "Frequency-Dependent Circuit Models of Carbon Nanotube Networks," in *IEEE 18th Conf. Elect. Performance Electron. Packag Systems*, Portland, OR, 19-21 Oct. 2009, pp. 129–132.

[71] M.A. EL Sabbagh and S.M. El-Ghazaly,"Measurement-Based Models of Carbon Nanotube Networks," in *IEEE Radio and Wireless Symp*, New Orleans, LA, 10-14 Jan. 2010, pp. 340–343.

[72] M.A. EL Sabbagh and S. M. El-Ghazaly, "Miniaturized carbon nanotube-based RF resonator," in *IEEE Int. Microwave Theory Tech. Symp. Dig.*, Boston, MA, 7-12 Jun. 2009, pp. 829-832.

[73] L. Liu, L.B. Kong, and S. Matitsine, "Tunable effective permittivity of carbon nanotubes composites," *Appl. Phys. Lett.*, vol. 93, no. 11, pp. 113106 (1-3), Sept. 2008.

[74] N. Li, Y. Huang, F. Du, X. He, Xi. Lin, H. Gao, Y. Ma, F. Li, Y. Chen, and P.C. Eklund, "Electromagnetic interference (EMI) shielding of single-walled carbon nanotube epoxy composites," *Nano lett.*, vol. 6, no. 6, pp. 1141-1145, May 2006.

[75] I.M. De Rosa, F. Sarasini, M.S. Sarto, and A. Tamburrano, "EMC Impact of Advanced Carbon Fiber/Carbon Nanotube Reinforced Composites for Next-Generation Aerospace Applications," *IEEE trans. Electromagn. Compat.*, vol.50, no.3, pp.556-563, Aug. 2008.

[76] A.G. Chiariello, A. Maffucci, G. Miano, and F. Villone, "High frequency and crosstalk analysis of VLSI carbon nanotube nanointerconnects,"in *Int. Symp. Electromagn. Compat. Europe*, Athens, Greece, 11-12 Jun. 2009, pp.1-4.

[77] M.S. Sarto, and A. Tamburrano, "Multiwall carbon nanotube vias: An effective TL model for EMC oriented analysis," in *IEEE Int. Symp. Electromagn. Compati.*, Austin, TX, 17-21 Aug. 2009, pp. 97-102.

[78] D. Barlage, R. Arghavani, G. Dewey, M. Doczy, B. Doyle, J. Kavalieros, A. Murthy, B. Roberds, P. Stokley, and R. Chau, "High-frequency response of 100nm integrated CMOS transistors with high-K gate dielectrics," in *IEDM Tech. Dig. Int.*, Washington, DC, 2-5 Dec. 2001, pp.10.6.1-10.6.4.

[79] C. Rutherglen, and P. Burke, "Carbon nanotube radio," *Nano Lett.*, vol. 7, no. 11, pp. 3296–3299, Oct. 2007.

[80] K. Jensen, J. Weldon, H. Garcia, and A. Zettl, "Nanotube radio," *Nano Lett.*, vol. 7, no. 11, pp. 3508–3511, Oct. 2007.

[81] C. Rutherglen, D. Jain, and P. Burke, "Nanotube electronics for radiofrequency applications," *Nature nanotechnology*, vol. 4, pp. 811-819, Nov. 2009.

[82] A. Nocke, M. Wolf, H. Budzeir, K. F. Arndt, and G. Gerlach, "Dielectrophoretic alignment of polymer compounds for thermal sensing," *Sensors and Actuators A: Physical*, vol. 156, no. 1, pp. 164-170, Nov. 2009.

[83] H.W. Seo, C.S. Han, D.G. Choi, K.S. Kim, and Y.H Lee, "Controlled assembly of single SWNTs bundle using dielectrophoresis," *Microelectron. Eng.*, vol. 81, no. 1, pp. 83-89, Jul. 2005.

[84] H. Rokadia, S. Tung, and M. Gordon, "Characterization of laterally aligned carbon nanotubes formed by AC dielectrophoresis," in *IEEE Conf. Nanotechnology*, pp. 361-366, Hong Kong, China, Aug. 2007.

[85] L. Song, G. Toth, J. Wei, Z. Liu, W. Gao, L. Ci, R. Vajtai, M. Endo and P.M. Ajayan, "Sharp burnout failure observed in high current-carrying double-walled carbon nanotube fibers," *Nanotechnology*, vol.23, no.1, pp. 1-7, Dec. 2011.

[86] S. Tung, H. Rokadia, and W.J. Li, "A micro shear sensor based on laterally aligned carbon nanotubes," *Sensors and Actuators A: Physical*, vol. 133, no. 2, pp. 431–438, Feb. 2007.

[87] E. Decrossas, and S.M. El-Ghazaly, "Microwave characterization of carbon nanotube networks" in *Carbon Nanotubes – From Research to Applications*, Rijeka, Croatia: Intech, 2011, ch. 9, pp. 142-156.

[88] T.W. Odom, J.L. Huang, P. Kim, and C.M. Lieber, "Atomic structure and electronic properties of single-walled carbon nanotubes," *Nature*, vol. 391, pp. 62–64, Jan. 1998.

[89] P.G. Collins, M.S. Arnold, and P. Avouris, "Engineering carbon nanotubes and nanotube circuits using electrical breakdown," *Science*, vol. 292, no. 5517, pp. 706–709, Apr. 2001.

[90] K. El Shabrawy, K. Maharatna, D. Bagnall, and B.M. Al-Hashimi, "Modeling SWCNT bandgap and effective mass variation using a Monte Carlo approach," *IEEE trans. nanotechnology*, vol. 9, no.2, pp. 184-193, Mar. 2010.

APPENDIX A

The expressions of field components in a coaxial transmission line are given as follows:

TEM mode

$$\mathrm{e_r}(\mathrm{r},\phi,\mathrm{z}) = \frac{1}{\mathrm{r}}\mathrm{e}^{-\mathrm{j}k_0\mathrm{z}}$$
$$\mathrm{h}_\phi(\mathrm{r},\phi,\mathrm{z}) = \frac{1}{Z_{\mathrm{TEM}}}\mathrm{e_r}(\mathrm{r},\phi,\mathrm{z}) \quad \text{(A.1)}$$

where the TEM wave impedance is

$$Z_{\mathrm{TEM}} = \frac{\omega\mu}{k_0}$$

TM_{nm} modes

The solution of the Helmholtz equation gives:

$$e_{z_n}(\mathrm{r},\phi) = Z_n(\mathrm{k_c r})\begin{cases}\cos(n\phi) & \text{PEW}\\ \sin(n\phi) & \text{PMW}\end{cases} \quad \text{(A.2)}$$

where $Z_n(k_c r) = J_n(k_c r) + G_n Y_n(k_c r)$and the constant G_n is found by applying the boundary conditions: $e_{z_n}(\mathrm{r},\phi)$= 0 at r = $r_1^{(1)}$ and r = $r_2^{(1)}$. PEW and PMW denote perfect electric wall and perfect magnetic wall, respectively.

$$\mathrm{G}_n = -\frac{\mathrm{J}_n\left(\mathrm{k_c} r_1^{(1)}\right)}{\mathrm{Y}_n\left(\mathrm{k_c} r_1^{(1)}\right)} = -\frac{\mathrm{J}_n\left(\mathrm{k_c} r_2^{(1)}\right)}{\mathrm{Y}_n\left(\mathrm{k_c} r_2^{(1)}\right)} \quad \text{(A.3)}$$

In addition, the solution of the transcendental equation allowed us to find the roots of the equation. If the mth roots of

$$\mathrm{J}_n\left(\mathrm{k_c} r_1^{(1)}\right)\mathrm{Y}_n\left(\mathrm{k_c} r_2^{(1)}\right) - \mathrm{J}_n\left(\mathrm{k_c} r_2^{(1)}\right)\mathrm{Y}_n\left(\mathrm{k_c} r_1^{(1)}\right) = 0 \quad \text{(A.4)}$$

is designated by p_{nm}^{TM}, the allowed values of k_c are$k_{\mathrm{c}_{nm}}^{\mathrm{TM}} = \frac{p_{nm}^{\mathrm{TM}}}{r_1^{(1)}}$where $n = 0,1,2,3,\ldots N$ $n = 0,1,2,3,\ldots N$ and $m = 1,2,3,\ldots M$. Therefore the propagation constant can be described as

$$\gamma_{nm}^{2}{}^{\mathrm{TM}} = \mathrm{k_c}_{nm}^{2\,\mathrm{TM}} - \mathrm{k}^2 \tag{A.5}$$

where$\mathrm{k}^2 = \omega^2\mu\varepsilon$.

Finally, the field components for TM_{nm} higher-order modes are

$$\mathrm{e_z}_{nm}(\mathrm{r},\phi,\mathrm{z}) = \mathrm{Z}_n\left(\mathrm{k_c}_{nm}^{\mathrm{TM}}\mathrm{r}\right)\mathrm{e}^{-\gamma_{nm}^{\mathrm{TM}}\mathrm{z}}\begin{cases}\cos(n\phi) & \mathrm{PEW}\\ \sin(n\phi) & \mathrm{PMW}\end{cases} \tag{A.6}$$

$$\mathrm{h_r}_{nm}(\mathrm{r},\phi,\mathrm{z}) = \frac{\mathrm{jn}\omega\varepsilon}{\mathrm{r}\mathrm{k}_{\mathrm{c}nm}^{2\,\mathrm{TM}}}\,\mathrm{Z}_n\left(\mathrm{k_c}_{nm}^{\mathrm{TM}}\mathrm{r}\right)\mathrm{e}^{-\gamma_{nm}^{\mathrm{TM}}\mathrm{z}}\begin{cases}-\sin(n\phi) & \mathrm{PEW}\\ \cos(n\phi) & \mathrm{PMW}\end{cases} \tag{A.7}$$

$$\mathrm{h}_{\phi\,nm}(\mathrm{r},\phi,\mathrm{z}) = \frac{-\mathrm{j}\omega\varepsilon}{\mathrm{k_c}_{nm}^{\mathrm{TM}}}\,\mathrm{Z'}_n\left(\mathrm{k_c}_{nm}^{\mathrm{TM}}\mathrm{r}\right)\mathrm{e}^{-\gamma_{nm}^{\mathrm{TM}}\mathrm{z}}\begin{cases}\cos(n\phi) & \mathrm{PEW}\\ \sin(n\phi) & \mathrm{PMW}\end{cases} \tag{A.8}$$

$$\mathrm{e}_{\phi\,nm}(\mathrm{r},\phi,\mathrm{z}) = -\mathrm{Z_{TM}}\,\mathrm{h_r}_{nm}(\mathrm{r},\phi,\mathrm{z}) \qquad \mathrm{e_r}_{nm}(\mathrm{r},\phi,\mathrm{z}) = \mathrm{Z_{TM}}\,\mathrm{h}_{\phi\,nm}(\mathrm{r},\phi,\mathrm{z})$$
$$\mathrm{h_z}_{nm}(\mathrm{r},\phi,\mathrm{z}) = 0 \tag{A.9}$$

where the wave impedance for the $TM_{nm}{}^{th}$ mode is

$$\mathrm{Z_{TM}} = \frac{\gamma_{nm}^{\mathrm{TM}}}{\mathrm{j}\omega\varepsilon}$$

TE_{nm} modes

Similarly, the solution of the Helmholtz equation gives

$$\mathrm{h_z}_n(\mathrm{r},\phi) = \mathrm{Z}_n(\mathrm{k_c r})\begin{cases}\cos(n\phi) & \mathrm{PEW}\\ \sin(n\phi) & \mathrm{PMW}\end{cases} \tag{A.10}$$

where $\mathrm{Z}_n(\mathrm{k_c r}) = \mathrm{J}_n(\mathrm{k_c r}) + \mathrm{g}_n\mathrm{Y}_n(\mathrm{k_c r})$ and the constant g_n is fund by applying the boundary conditions. Therefore the longitudinal component of the magnetic field must vanish at the surface conductors. Hence,

$$\frac{\partial}{\partial \mathrm{r}}\mathrm{h_z}_n(\mathrm{r},\phi)\Big|_{\mathrm{r}=r_1^{(1)}} = \frac{\mathrm{d}}{\mathrm{dr}}\left[\mathrm{Z}_n(\mathrm{k_c r})\right]\Big|_{\substack{\mathrm{r}=r_1^{(1)}\\ \mathrm{r}=r_2^{(1)}}} = 0 \tag{A.11}$$

and we get the constant

$$g_n = -\frac{J'_n\left(k_c r_1^{(1)}\right)}{Y'_n\left(k_c r_1^{(1)}\right)} = -\frac{J'_n\left(k_c r_2^{(1)}\right)}{Y'_n\left(k_c r_2^{(1)}\right)} \tag{A.12}$$

Similarly, if the m[th] roots of the transcendental equation

$$J'_n\left(k_c r_1^{(1)}\right)Y'_n\left(k_c r_2^{(1)}\right) - J'_n\left(k_c r_2^{(1)}\right)Y'_n\left(k_c r_1^{(1)}\right) = 0 \tag{A.13}$$

is designated by $p_{nm}^{TE} p_{nm}^{TE}$, we find that the allowed values of k_c are $k_{c_{nm}}^{TE} = \frac{p_{nm}^{TE}}{r_1^{(1)}}$ where $n = 0,1,2,3, \ldots N$ $n = 0,1,2,3, \ldots N$ and $m = 1,2,3, \ldots M$.

Finally, the field components for TE_{nm} higher-order modes can be expressed as

$$h_{z_{nm}}(r,\phi,z) = Z_n\left(k_{c_{nm}}^{TE} r\right)e^{-\gamma_{nm}^{TE} z}\begin{cases}\cos(n\phi) & \text{PEW}\\ \sin(n\phi) & \text{PMW}\end{cases} \tag{A.14}$$

$$h_{r_{nm}}(r,\phi,z) = \frac{-\gamma_{nm}^{TE}}{k_{c_{nm}}^{TE}} Z'_n\left(k_{c_{nm}}^{TE} r\right)e^{-\gamma_{nm}^{TE} z}\begin{cases}\cos(n\phi) & \text{PEW}\\ \sin(n\phi) & \text{PMW}\end{cases} \tag{A.15}$$

$$h_{\phi_{nm}}(r,\phi,z) = \frac{-\gamma_{nm}^{TE}}{k_{c_{nm}}^{2\,TE}}\frac{n}{r} Z_n\left(k_{c_{nm}}^{TE} r\right)e^{-\gamma_{nm}^{TE} z}\begin{cases}-\sin(n\phi) & \text{PEW}\\ \cos(n\phi) & \text{PMW}\end{cases} \tag{A.16}$$

$$e_{r_{nm}}(r,\phi,z) = Z_{TE}\, h_{r_{nm}}(r,\phi,z) \quad e_{\phi_{nm}}(r,\phi,z) = -Z_{TE}\, h_{r_{nm}}(r,\phi,z)$$
$$e_{z_{nm}}(r,\phi,z) = 0 \tag{A.17}$$

where the wave impedance for TE_{nm} [th]mode is

$$Z_{TE} = \frac{j\omega\mu}{\gamma_{nm}^{TE}}$$

APPENDIX B

The rigorous derivation of the mutual inner product of coaxial-circular discontinuity concerning the TM_{nm} modes in region 2 and $TM_{n'm'}$ modes in region 3

$$M_{nm,n'm'}^{TM(2)-TM(3)}$$

$$= \frac{\gamma_{nm}^{TM(2)}}{k_{c_{nm}}^{TM(2)}} \frac{j\omega\varepsilon^{(3)}}{k_{c_{n'm'}}^{TM(3)}} \left(\int_0^{2\pi} \begin{cases} \cos(n\emptyset)\cos(n'\emptyset) \\ \sin(n\emptyset)\sin(n'\emptyset) \end{cases} d\emptyset \int_{r_2^{(2)}}^{r_1^{(2)}} Z'_n\left(k_{c_{nm}}^{TM(2)} r\right) J'_{n'}\left(k_{c_{n'm'}}^{TM(3)} r\right) r dr \right. \quad \text{(B.1)}$$

$$\left. + \int_0^{2\pi} \begin{cases} \sin(n\emptyset)\sin(n'\emptyset) \\ \sin(n\emptyset)\cos(n'\emptyset) \end{cases} d\emptyset \int_{r_2^{(2)}}^{r_1^{(2)}} \frac{nn'}{k_{c_{n'm'}}^{TM(3)} k_{c_{nm}}^{TM(2)} r^2} Z_n\left(k_{c_{nm}}^{TM(2)} r\right) J_{n'}\left(k_{c_{n'm'}}^{TM(3)} r\right) r dr \right)$$

By evaluating the $\emptyset$ dependent integrals, using the orthognality properties of the cosine and sine we get:

$$I_1 = \int_0^{2\pi} \begin{cases} \cos(n\emptyset)\cos(n'\emptyset) \\ \sin(n\emptyset)\sin(n'\emptyset) \end{cases} = \begin{cases} 2\pi & , n = n' = 0 \\ \pi & , n = n' \neq 0 \text{ for PEW} \\ 0 & , n \neq n' \end{cases}$$

$$I_2 = \int_0^{2\pi} \begin{cases} \sin(n\emptyset)\sin(n'\emptyset) \\ \sin(n\emptyset)\cos(n'\emptyset) \end{cases} = \begin{cases} 0 & , n = n' = 0 \\ \pi & , n = n' \neq 0 \text{ for PMW} \\ 0 & , n \neq n' \end{cases}$$

where PEW stands for perfect electric wall and PMW for perfect magnetic wall.

The *r* dependent integral is solved by using the recurrence relations of the Bessel properties as:

$$Z'_n\left(k_{c_{nm}}^{TM(2)} r\right) + \frac{n}{k_{c_{nm}}^{TM(2)} r} Z_n\left(k_{c_{nm}}^{TM(2)} r\right) = Z_{n-1}\left(k_{c_{nm}}^{TM(2)} r\right) \quad \text{(B.2)}$$

$$J'_n\left(k_{c_{n'm'}}^{TM(3)} r\right) + \frac{n}{k_{c_{n'm'}}^{TM(3)} r} J_n\left(k_{c_{n'm'}}^{TM(3)} r\right) = J_{n'-1}\left(k_{c_{n'm'}}^{TM(3)} r\right) \quad \text{(B.3)}$$

$$Z'_n\left(k_{c_{nm}}^{TM(2)} r\right) - \frac{n}{k_{c_{nm}}^{TM(2)} r} Z_n\left(k_{c_{nm}}^{TM(2)} r\right) = -Z_{n+1}\left(k_{c_{nm}}^{TM(2)} r\right) \quad \text{(B.4)}$$

$$J'_n\left(k_{c_{n'm'}}^{TM(3)} r\right) - \frac{n}{k_{c_{n'm'}}^{TM(3)} r} J_n\left(k_{c_{n'm'}}^{TM(3)} r\right) = -J_{n'+1}\left(k_{c_{n'm'}}^{TM(3)} r\right) \quad \text{(B.5)}$$

By multiplying (B.2) with (B.3) and (B.4) with (B.5) and add the results, we obtained

$$C_1 = \frac{1}{2} \int_{r_2^{(2)}}^{r_1^{(2)}} \left[Z_{n-1}\left(k_{c_{nm}}^{TM(2)} r\right) J_{n'-1}\left(k_{c_{n'm'}}^{TM(3)} r\right) + Z_{n+1}\left(k_{c_{nm}}^{TM(2)} r\right) J_{n'+1}\left(k_{c_{n'm'}}^{TM(3)} r\right) \right] r dr \quad \text{(B.6)}$$

Solving the first part of the integral and applying the boundary conditions $Z_n\left(k_{c_{nm}}^{\mathrm{TM}(2)}\begin{Bmatrix}r_1^{(2)}\\ r_2^{(2)}\end{Bmatrix}\right)=0$ and $J_{n\prime}\left(k_{c_{n\prime m\prime}}^{\mathrm{TM}(3)}r_1^{(2)}\right)=0$, we get:

$$C_2=\frac{1}{2}\frac{r_2^{(2)}k_{c_{n\prime m\prime}}^{TM(3)}}{k_{c_{nm}}^{2\ \mathrm{TM}(2)}-k_{c_{n\prime m\prime}}^{2\ \mathrm{TM}(3)}}Z_{n-1}\left(k_{c_{nm}}^{\mathrm{TM}(2)}r_2^{(2)}\right)J_{n\prime}\left(k_{c_{n\prime m\prime}}^{\mathrm{TM}(3)}r_2^{(2)}\right) \tag{B.7}$$

Similarly the second part of the integral after applying the boundary conditions is reduced to the following expression:

$$C_3=-\frac{1}{2}\frac{r_2^{(2)}k_{c_{n\prime m\prime}}^{TM(3)}}{k_{c_{nm}}^{2\ \mathrm{TM}(2)}-k_{c_{n\prime m\prime}}^{2\ \mathrm{TM}(3)}}Z_{n+1}\left(k_{c_{nm}}^{\mathrm{TM}(2)}r_2^{(2)}\right)J_{n\prime}\left(k_{c_{n\prime m\prime}}^{\mathrm{TM}(3)}r_2^{(2)}\right) \tag{B.8}$$

Hence, the final solution is equivalent to $C_1=C_2+C_3$ and after applying the recurrence Bessel relation in addition to the boundary conditions

$$Z_{n-1}\left(k_{c_{nm}}^{\mathrm{TM}(2)}r_2^{(2)}\right)=-Z_{n+1}\left(k_{c_{nm}}^{TM(2)}r_2^{(2)}\right) \tag{B.9}$$

the mutual inner product TM-TM between a coaxial and circular waveguides is performed by substituting the results of C_1 as shown in expression (2.20).